BEAM-INDUCED RADIATION HEATING ON THE SUPERCONDUCTING UNDULATOR AT THE ADVANCED PHOTON SOURCE

A Dissertation

Submitted to the Faculty

of

Purdue University

by

Laura Elizabeth Boon

In Partial Fulfillment of the

Requirements for the Degree

of

Doctor of Philosophy

December 2014

Purdue University

West Lafayette, Indiana

ACKNOWLEDGMENTS

I would like to thank my thesis advisor Dr. Katherine Harkay, for her guidance and encouragement over the last 4 years. This thesis would not have been possible without her support. I would also like to thank my Purdue Advisors, Professor Arthur Garfinkel and Professor Steve Durbin, for their time and guidance while I was working at Argonne National Laboratories. A special thank you the the APS scientists and technicians who, designed, built and installed SCU0. I appreciate your support in providing updated design drawings, lattice files and alignment information.

Thank you to all my collaborators at other laboratories, Jim Crittenden, Roberto Cimino for all the helpful discussions, and advice. And the American Physical Society staff for their support of my work with the Forum on Graduate Student Affairs. Thank you to my friends and co-workers. At APS; Jon Smejkal, and Brian Pruitt, I enjoyed our evening walks around the ring, and political discussions. To Cristina Moody, for the afternoon coffee breaks when we just needed to get away from our desks for a bit. And to my friends at at Purdue David Garand, Katie Davis, Jonathan Nafziger, Brendan Sullivan and Jordan Kendall, thank you for keeping me awake through all our late night homework sessions!

A big thank you to my parents, Richard and Martha Boon, for their unending support and encouragement over the years. Finally I would like to thank my husband, Kent Wootton, for his encouragement and attention to detail in references. Your enthusiasm for Physics is contagious!

TABLE OF CONTENTS

Page

LIST OF TABLES

LIST OF FIGURES

Figure Page

Figure Page

ABSTRACT

Boon, Laura Ph.D., Purdue University, December 2014. Beam-induced Radiation Heating on the Superconducting Undulator at the Advanced Photon Source. Major Professor: Katherine Harkay.

In January 2013 the Advanced Photon Source (APS), a 7 GeV synchrotron X-ray source, commissioned a Superconducting Undulator (SCU). The superconducting magnet is thermally isolated from the beam vacuum chamber, which absorbs the beam-induced heating [1]. Previous beam induced heat load studies at other laboratories had not included a robust calculation of radiation heating from the upstream dipole magnet. The mitigation of the radiation heating mechanism, and production of photoelectrons to seed an electron cloud was studied for this thesis.

An analytical model was developed to predict the radiation heat load on the SCU chamber. This model was benchmarked with ray tracings and simulations. Results from this synchrotron radiation model were used to guide the design of the installed SCU beam chamber. A 3D Monte-Carlo simulation on synchrotron radiation on the beam chamber was developed. The model considered the effect of diffuse scattering and complex chamber geometries. It was found that a simulation assuming no photon scattering gave a power that agreed within 0.4% of the analytical model. Comparison between analytical calculations and measured temperature rise on the installed SCU show the analytical model agrees with the measured temperature rise within 20%. Previous models of similar superconducting devices in accelerators have reached at best 200% difference between the measured and modeled heat load. The beam heat load model presented in this thesis represents a significant improvement in modeling of superconducting devices in high energy particle accelerators.

In addition to heating the SCU chamber, absorbed photons produce photoelectrons which seed electron clouds, another source of beam induced heating. Measurements of the technical aluminum samples show peaks in the quantum efficiency for photon energies equal to the K edges of oxygen, carbon, and aluminum. These results can be added to electron cloud simulation codes to improve simulation results.

1. INTRODUCTION

Current undulators use a either permanent magnets or room temperature electromagnets to produce magnetic fields; both devices have limitations on the peak field, and undulator period. By switching to a superconducting electromagnet shorter period undulators can be made while maintaining a high magnet field. In addition to the engineering design needed to design such an electromagnet, the magnet much be kept cool so the superconducting coils do not quench. However accelerators are an intense environment with many sources of heating. Previous work on beam induced heating has not created a satisfactory model for measured temperature rise.

There are four beam induced heat sources of concern for operating a superconducting magnet in an accelerator: radiation heating, resistive wall heating, electron cloud multipacting, and wake fields. The work presented in this thesis focuses on heating from dipole magnet radiation. Calculations of the heating will be done in three ways and compared. An analytical model was created, simulations were done and measurements of temperature rise were done. Also discussed will be ways to mitigate the radiation heating, with a note on how it effects other beam induced heating elements.

1.1 Outline

This thesis is divided into two parts. Part 1is composed of chapters 2-5. Chapter 2 will present the motivation for this thesis, covering the heating sources, previous work that has been done in calculating and modeling beam inducted heating on SCU's installed in other machines. Next the the background on synchrotron radiation will be presented in chapter 3, including the distribution of dipole radiation which will be used when calculating the radiation heating on the SCU, in a later chapter. Chapter 4 will introduce Synrad3D, a Monte Carlo program used to simulate radiation heating as part of this thesis. The last part of the introduction, chapter 5 will describe the layout of the section of accelerator modeled in this thesis.

The second part is comprised of chapters 6-9. In chapter 6 the analytical model created will be described, including a discussion of the parameters included in the radiation heating model. In chapter 7, results from Synrad3D simulations will be discussed and benchmarked against the analytical model. Included in the chapter will be a discussion of the effect of surface roughness on the photon distribution in the SCU chamber. Chapter 8 will describe the measurement technique and analysis method to measure the temperature rise in the SCU for an electron beam off-axis in the upstream dipole magnet. A comparison of measurement results with an analytical model of temperature rise will also be discussed. In chapter 9 measurements of the quantum efficiency are presented.

2. MOTIVATION

Third generation light sources, such as the Advanced Photon Source (APS), use insertion devices (ID) to provide the highest brightness photon beams to its users. These ID's are customized for various experiments needing certain photon energy or polarization. Current technology has reached its peak in electromagnet and hybrid permanent magnets. To produce these high energy photon beams either the peak magnetic field must be increased or the period length must be shortened. Research was done to design, build and implement superconducting undulators (SCU) in high energy storage rings. SCUs allow for shorter period lengths and higher magnetic fields, producing high brightness beams for user studies. This chapter will describe the current research at done at high energy storage rings to install and run superconducting ID magnets. The chapter will end with a description of the APS SCU and the proposed mitigation techniques.

2.1 Beam Induced Heating Processes

A limitation of superconducting technology is the heat load from the high energy electron beam. There are four main processes that must be understood and mitigated for the SCU to run transparently in the storage ring.

Resistive Wall Heating

The charged beam creates a current in the conducting walls of the vacuum beam chamber, with the opposite charge of the beam. These image currents heat the beam chamber due to the resistivity of the vacuum chamber. The heat load is dependent on the chamber material and frequency spectrum of the bunch train.

Electron Cloud

When low energy electrons build up inside the vacuum chamber of a particle accelerator or storage ring it is called an electron cloud. Electron clouds are accelerated into the chamber wall causing heating. In addition to the heating, the electron cloud can create problems for the particle beam by creating head tail instabilities, shift the tune of the beam and increase the emittance, among other problems [2, 3].

Electron cloud multipacting has been an area of much research and development for positron and proton machines [4–7], as those machines have been used for high energy physics research. Current research has focused on reducing the secondary electron yield of beam chamber materials through coatings and conditioning [8] as a way to mitigate electron cloud growth. As superconducting undulators (SCU) are being installed into high energy electron storage ring light sources [9, 10] reducing the heat load from electron cloud is important for optimal performance of the electron machine. Simulations of electron cloud build up in electron rings is not consistent between measurements taken at the Advanced Photon Source (APS) [11] and ANKA (ANgstrom source KArlsruhe) [12] possibly due to over-simplified photoelectron yield models used in the electron cloud simulation codes. Previous work at DAΦNE [13] and the LHC [14] have presented results for the photoelectron yield of low energy photons.

Wake Field Heating

Any changes in vacuum chamber dimensions can induce wake fields, standing electromagnetic fields, induced by the relativistic beam. To reduce wake field heating superconducting magnet chamber designs avoid short changes in chamber diameter.

Radiation Heating

Dipole magnets produce a fan of synchrotron radiation tangential to the path of the relativistic beam. Based on the accelerator geometry a section of that fan is incident on the superconducting chamber walls. To shield the chamber a system of collimators or photon absorbers are used. These will shield the chamber from direct radiation.

2.2 Current and proposed Superconducting devices

Superconducting technology has been used to build new undulators and wigglers for many years. Accelerators around the world have used this technology to install specialized insertion devices in their rings. At each of these facilities research into the beam induced heat load has been unable to produce an accurate model. This section will outline the work that has been done at these facilities.

2.2.1 MAX-Wiggler

Results of the beam induced heat load on the MAX-II superconducting wiggler (MAX-Wiggler) were published in [15]. MAX-II is a 1.5 GeV light source, in Laude Sweden. Pre-installation calculations estimated a total beam induced heat load of 0.17 W, 0.12 W from synchrotron radiation and 0.05 W from resistive wall heating. Measurements from the installed device showed a heat load of 0.86 W, 0.26 W from synchrotron radiation and 0.59 W from resistive wall heating. A full analysis of the resistive wall heating was done, in an attempt to reduce the resistive wall heat load a Cu strip 25 mm wide was deposited on the top and bottom of the beam chamber. The width and thickness of this strip needed was calculated analytically to minimize the heat load. The authors believe that the installed device has a higher resistivity of the Cu coating than what was used for the calculations, and this could account for the discrepancy in resistive wall heating. Misalignment of the upstream photon absorber could account for the extra heat load from synchrotron radiation. The wiggler was designed with more cooling power than the theoretical model predicted, therefore the device still operates to the required specifications.

2.2.2 Angstroem Source Karlsruhe (ANKA)

A superconducting undulator in use is at Angstroem Source Karlsruhe (ANKA) in Karlsruhe, Germany. This undulator was installed in March 2005 to evaluate the possibility of using SCUs in high energy storage rings [16]. The ANKA cryostat is shown in Figure 2.1.

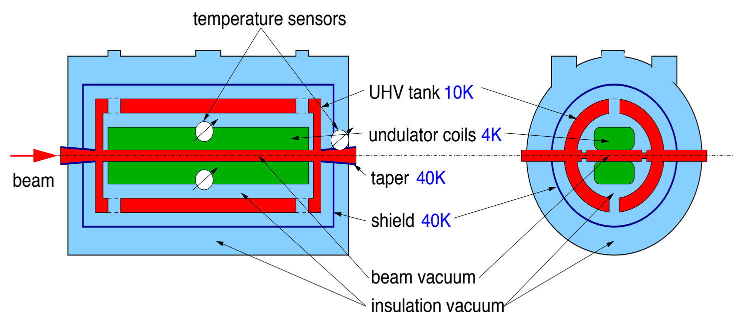

Fig. 2.1. A schematic of the cooling system for the SCU at ANKA. Three cryocoolers are used instead of cryogenics [9].

This SCU is cryogen free and uses three Sumitomo cryocoolers, two to cool the coils at 4K and one to keep the UHV tank at 10K [9]. Vacuum sections are used to thermally isolate the 4K coils from the 10K UHV tank and room temperature. There is no beam chamber separating the SCU magnet coils from the beam, so the ANKA SCU is called an in-vacuum undulator. Its period length is 14 mm and the magnets can generate a maximum magnetic field of 0.8 T with an 8 mm gap [17]. To vary the magnetic field, and the K value for the undulator, the poles can have gap widths of 16, 12 and 8 mm, full height. During injection the undulator gap must be 29 mm, full height, and have no current in the coils to prevent a quench from beam loss during injection.

2.2.3 Cold Vacuum Chamber for Diagnostics

Cold Vacuum Chamber for Diagnostics (COLDDIAG) is a cold vacuum chamber installed in Diamond Light Source to study beam induced heating on cold vacuum chambers. The cold section of the chamber is 0.5 m long, and cooled by a Sumitomo RDK-415D cryocooler. The chamber has been fitted with temperature sensors, residual gas analyzer and a retarding field analyzer [18] to measure the electron cloud. Results from measurements of beam induced heating are presented in [19–22]. Theoretical models showed resistive wall heating as the dominate heat load but, based on the measurements another source dominates. The measured heat load was an order of magnitude greater than the theoretical predictions. After a full analysis, they report that the extra heat load is unexplained from any known source, resistive wall, or electron and ion bombardment; synchrotron radiation heating was not considered. Work in understanding the heat load is continuing.

2.2.4 International Linear Collider Damping Rings Wigglers

The proposed design for the International Linear Collider (ILC) damping rings use superconducting wigglers to damp the electron beam emittance. Electron cloud multipacting can be amplified in positron machines so research has been done to understand and mitigate heating from electron cloud buildup [4]. Another concern is radiation heating from radiation produced by the damping wigglers. To mitigate this heating photon absorbers are placed along the length of the wiggler section; each photon absorber can absorb more than the 42 W of power incident [23, 24].

2.3 Advanced Photon Source Superconducting Undulator

The SCU was designed to increase photon brightness above 25 keV and still allow APS to operate with the 3 operating bunch timing patterns provided to users.

The SCU design will allow for magnetic fields near 1 T with short 15-20 mm period lengths, to produce high brightness and high energy photons in the first harmonic of the undulator. Previously such high fields would require period lengths around 30 mm [25]. Figure 2.2 shows the higher brilliance achievable with such an undulator. This plot compares the proposed SCU brightness curves with the current generic undulator curve, UA.

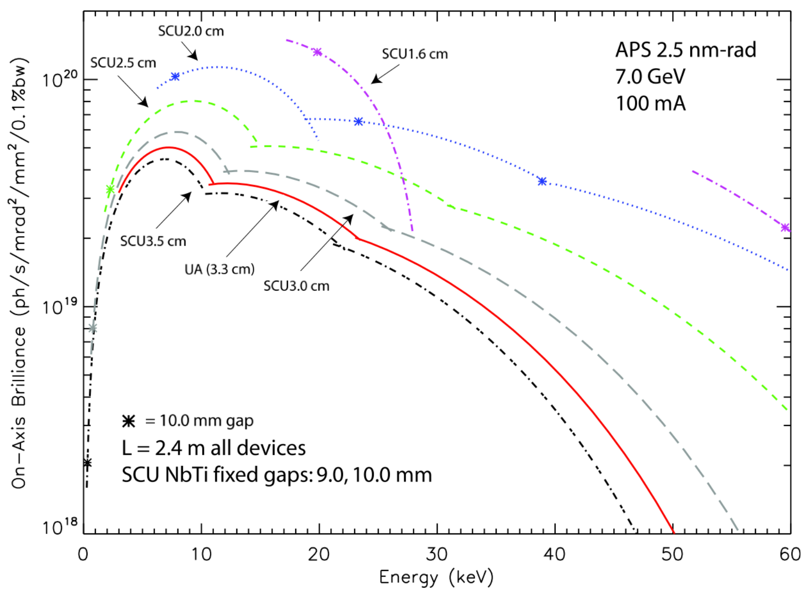

Fig. 2.2. Graph of the on-axis brillance curves for an SCU with varying period lengths [25].

The early stages of research included modeling the SCU, trying to optimize the brilliance between 20-25 keV with a magnetic gap of 9 mm to allow for the beam chamber walls [25]. Unlike the undulator installed at ANKA the undulator coils at

APS will not be in the beam vacuum. APS has a beam chamber that is thermally isolated from the magnet device.

The cooling for the APS SCU will be done with liquid helium (LHe). The chamber will nominally be kept at 20K, and thermally isolated from the SCU coils [25]. The chamber will be cooled by cryocoolers 3 and 4 in Figure 2.3. The cryocoolers can handle up to 40 W of heating on the chamber. These cryocoolers will also be cooling the 20K and 60 K radiation shields. While the SCU coils will be cooled with cryocoolers 1 and 2. This design is based on a superconducting wiggler at the Budker Institute in Novosibirsk, Russia [25]. SCU0 is 0.340 m long, with a period length of 16 mm.

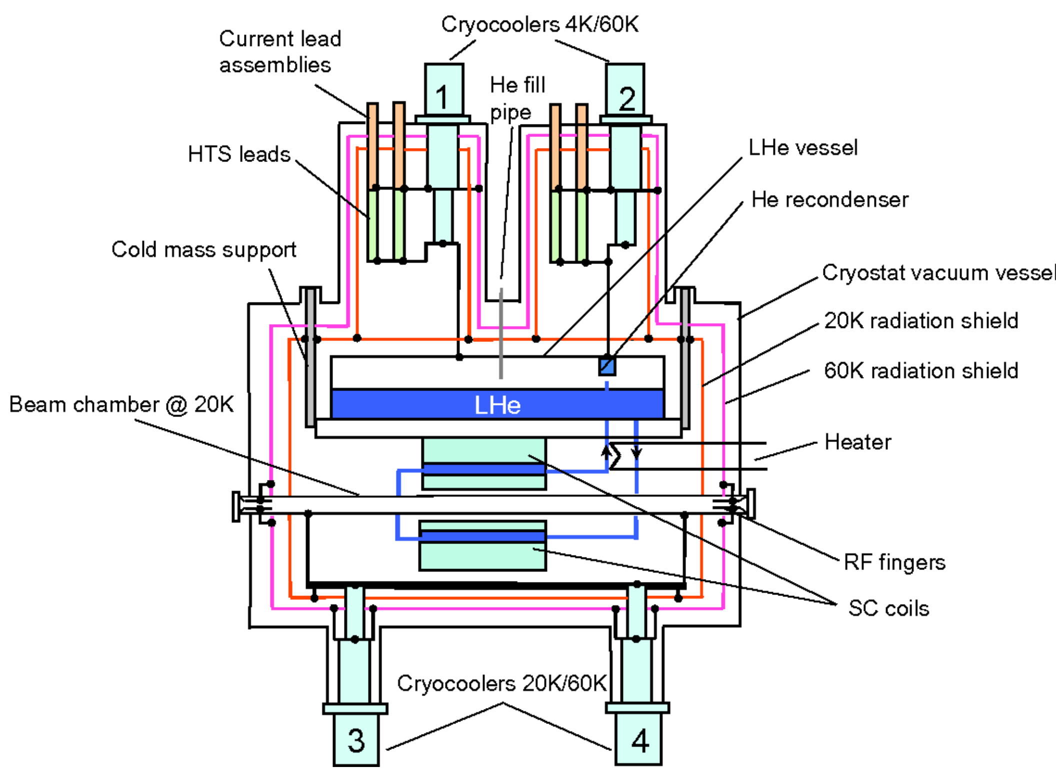

Fig. 2.3. Schematic of the cryosystem for the SCU prototype [25].

2.4 Summary

SCU's have been installed in high energy storage rings around the world. However the processes that heat the devices are not understood well enough to create reliable models of the beam induced heating. In this thesis heating from synchrotron radiation will be studied in detail.

3. INTRODUCTION TO SYNCHROTRON RADIATION

From electromagnetic theory it is known that accelerated charged particles radiate. Radiation produced by a relativistic particles in a circular accelerator is called synchrotron radiation. This chapter will introduce the physics and mathematics behind synchrotron radiation and the basics of bending magnet radiation.

3.1 Dipole Radiation

The electric and magnetic fields [26] from a point charge on an arbitrary path can be found with the equations,

$$\mathbf{E}(\mathbf{r},t) = \frac{q}{4\pi\epsilon_0}\frac{\mathscr{r}}{(\boldsymbol{\mathscr{r}}\cdot\mathbf{u})^3}[(c^2-v^2)\mathbf{u} + \boldsymbol{\mathscr{r}}\times(\mathbf{u}\times\mathbf{a})] \tag{3.1}$$

and

$$\mathbf{B}(\mathbf{r},t) = \frac{1}{c}\hat{\boldsymbol{\mathscr{r}}}\times\mathbf{E}(\mathbf{r},t), \tag{3.2}$$

where $\boldsymbol{\mathscr{r}}$ is the vector from the charge to the observer, $\mathbf{r}$ is the vector from the origin to the observer, $\mathbf{u} = c\hat{\boldsymbol{\mathscr{r}}} - \mathbf{v}$ and $\mathbf{a}$ is the acceleration. The term proportional to $\mathbf{u}$ is the velocity field, and the second term is the acceleration field. The power from a dipole can then be calculated using the Poynting vector, Equation 3.3.

$$\mathbf{S} = \frac{1}{\mu_0}(\mathbf{E}\times\mathbf{B}) = \frac{1}{\mu_0}[E^2\hat{\boldsymbol{\mathscr{r}}} - (\hat{\boldsymbol{\mathscr{r}}}\cdot\mathbf{E})\mathbf{E}] \tag{3.3}$$

Not all of this power is radiated away from the dipole. Integrating the Poynting vector over a sphere of radius $\mathscr{r}$ yields the radiated power. Any term proportional to $1/\mathscr{r}^2$ will be finite, while terms on the order of $1/\mathscr{r}^3$ and $1/\mathscr{r}^4$ or greater will tend to zero as $\mathscr{r}\to\infty$. This leaves only the acceleration field term $\mathbf{E}_{rad}$ in Equation 3.4

$$\mathbf{E}_{rad} = \frac{q}{4\pi\epsilon_0}\frac{\mathscr{r}}{(\mathscr{r}\cdot\mathbf{u})^3}[\mathscr{r}\times(\mathbf{u}\times\mathbf{a})] \tag{3.4}$$

Since the radiated field is perpendicular to $\mathscr{r}$ the second term in Equation 3.3 is zero, making the radiated power,

$$\mathbf{S}_{rad} = \frac{1}{\mu_0 c}E^2\hat{\mathscr{r}}. \tag{3.5}$$

If the particle has a small velocity we can simplify the equations by assuming $v = 0$, then $\mathbf{u} = c\hat{\mathscr{r}}$ and $\mathbf{E}_{rad}$ can be simplified to:

$$\mathbf{E}_{rad} = \frac{q\mu_0}{4\pi\mathscr{r}}[(\hat{\mathscr{r}}\cdot\mathbf{a})\hat{\mathscr{r}} - \mathbf{a}] \tag{3.6}$$

And the Poynting vector is,

$$\mathbf{S}_{rad} = \frac{\mu_0 q^2 a^2}{16\pi^2 c}\left(\frac{\sin^2(\theta)}{\mathscr{r}^2}\right)\hat{\mathscr{r}} \tag{3.7}$$

where θ is the angle between the acceleration vector, $\hat{a}$, and observer, $\hat{\mathscr{r}}$. This model is a good approximation for particles with $v << c$, but it is more complicated for particles with $v \simeq c$. The power radiated is the integral over the surface of a sphere around the source of the Poynting vector.

$$\mathbf{P} = \oint \mathbf{S}_{rad}\cdot d\mathbf{a} \tag{3.8}$$

From the Equation 3.8 and using the Doppler effect it is possible to calculate the power radiated by a relativistic particle per unit solid angle,

$$\frac{dP}{d\Omega} = \frac{q^2}{16\pi^2\epsilon_0}\frac{|\hat{\mathscr{r}}\times(\mathbf{u}\times\mathbf{a}|^2}{(\hat{\mathscr{r}}\cdot\mathbf{u})^5}. \tag{3.9}$$

In a synchrotron accelerator or storage ring, dipole magnets are used to bend the particles trajectory. These dipoles accelerate the particles in a direction perpendicular to the velocity. The power produced from relativistic particles ($\beta \simeq 1$) is sharply peaked in the instantaneous direction of the particle, tangential to the curve in the dipole. This power is given by,

$$\frac{dP}{d\Omega} = \frac{\mu_0 q^2 a^2}{16\pi^2 c} \frac{[(1-\beta\cos\theta)^2 - (1-\beta^2)\sin^2\theta\cos^2\phi]}{(1-\beta\cos\theta)^5}. \tag{3.10}$$

Synchrotron radiation is defined by its opening angle. It is seen that synchrotron radiation has a narrow opening angle diverging from the electron beam trajectory. The opening angle, θ_0, is described by $\cos\theta_0 = \beta$. As $\gamma \to \infty$ $\theta_0 = 1/\gamma$. This is the vertical and horizontal opening angle of synchrotron radiation. However in dipole magnets radiation is generated along the entire length of the magnet and a sweep of radiation is created with a horizontal opening angle equal to the bending angle of the magnet.

3.2 Dipole Magnet Energy Spectrum

With the effect of a relativistic boost on the angular distribution of synchrotron radiation quantified, we consider the resultant spectrum of bending magnet radiation. For this calculation Hofmann's book was referenced [27].

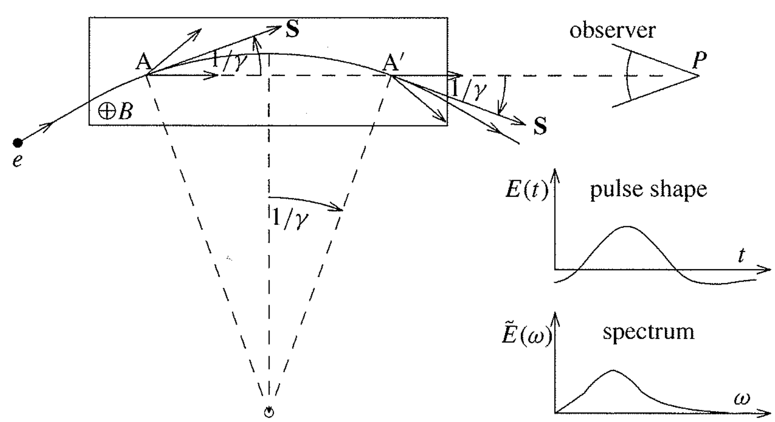

Fig. 3.1. Diagram for calculating the pulse length of a photon pulse in a long bending magnet. The opening angle of the radiation is $1/\gamma$ [27].

Assuming that the particle is traveling on a circular path through a long dipole magnet as in Figure 3.1, the length of the radiation pulse can be calculated. With an opening angle of $1/\gamma$ the radiation can first be seen by an observer at an angle of $1/\gamma$ from the perpendicular, A. The last point where radiation is detected by an observer is another $1/\gamma$ from the perpendicular, A', see Figure 3.1. The length of the pulse, δt, is the difference between the time it takes the particle to travel from A to A' on the circular path from the time it takes a photon to travel straight from A to A', Equation 3.11,

$$\delta t = t_e - t_\gamma = \frac{2\rho}{\beta\gamma c} - \frac{2\rho\sin(1/\gamma)}{c} = \frac{4\rho}{3c\gamma^3} \tag{3.11}$$

where ρ is the radius of the circle. Dipole magnets are usually characterized by their critical energy, E_c. Half of the total energy radiated is above the critical energy and half is below it. The critical frequency is $\frac{2}{\delta t}$ and the critical photon energy can be found from the equation [28],

$$E_c[keV] = 0.66503E^2[GeV]B[T]. \tag{3.12}$$

The spectrum of the radiation is the Fourier transform of the pulse shape. The higher energy the storage ring the shorter the radiation pulse will be and the wider the frequency spectrum. The dipole radiation spectrum for an APS bending magnet can be see in Figure 3.2.

3.3 Insertion Devices

Undulators and wigglers are used in 3^{rd} generation light sources to produce high brightness and high energy photons. The spectrum of each of the radiation sources, bending magnets, wigglers and undulators is slightly different based on the path of the electron beam, Figure 3.3. Both wigglers and undulators use alternating dipole magnets to change the trajectory of the beam in the horizontal plane. The difference between wigglers and undulators is the strength of that change. This is defined by the strength parameter, K, equal to:

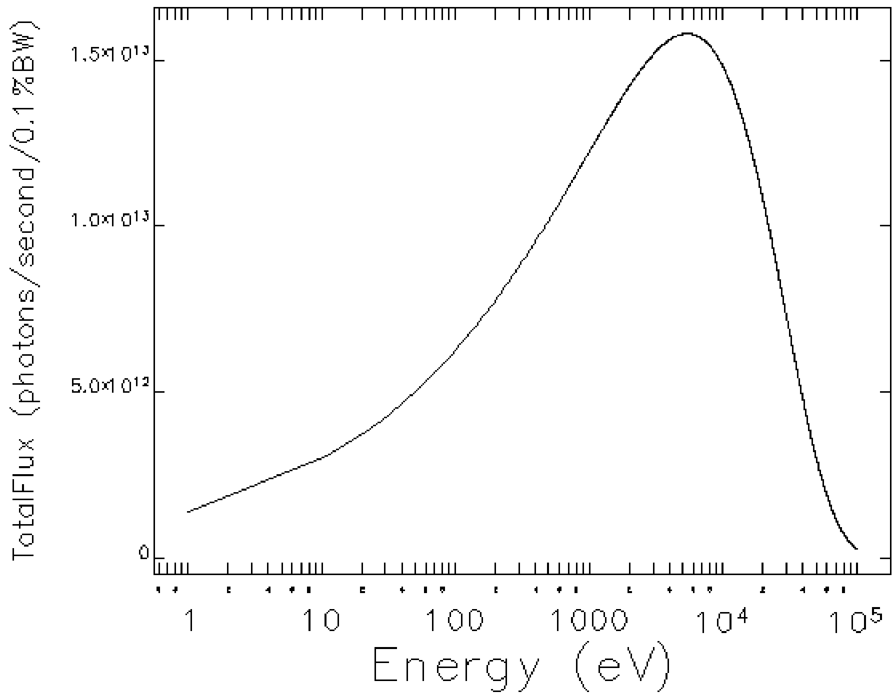

Fig. 3.2. The dipole spectrum from a main APS bending magnet. APS has a critical energy of 19 keV.

$$K = \theta\gamma = \frac{ecB}{mc^2}\frac{\lambda_p}{2\pi} = 0.934 B_0(T)\lambda_p(cm) \tag{3.13}$$

where θ is the electron deflection angle, e is the electric charge, B the magnetic field strength, and λ_p is the period length. In the next two sections the specifics of each insertion device will be discussed.

3.3.1 Wigglers

For a wiggler with short poles and only deflection in the x direction the magnetic field can be approximated by:

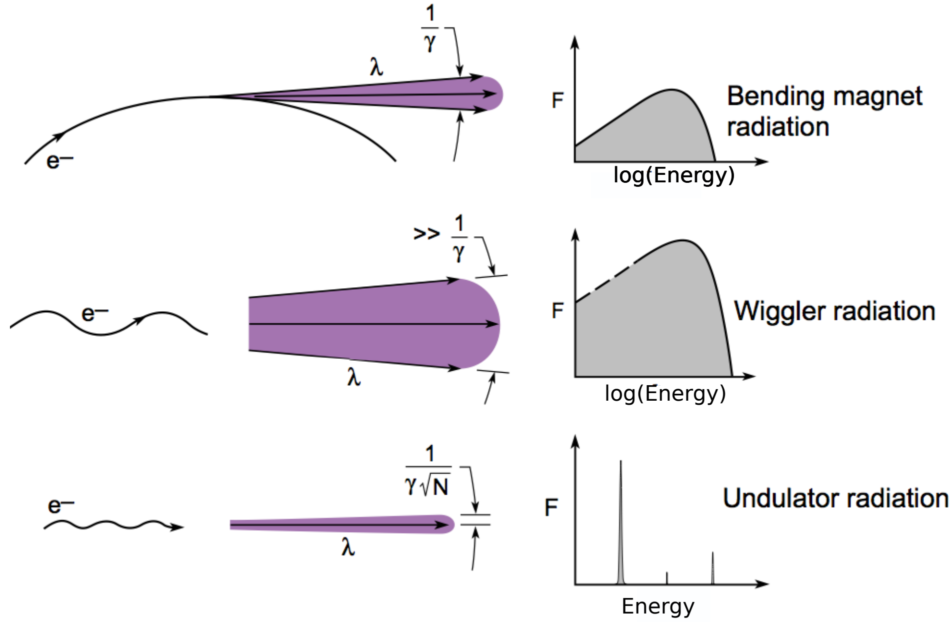

Fig. 3.3. The opening angle and spectrum from the three radiation source magnets [29].

$$B_y(x, y = 0, z) = B_0 \sin \frac{2\pi z}{\lambda_p}. \tag{3.14}$$

The maximum deflection angle θ is the integral over half of one pole. This is defined by the following integral,

$$\theta = \frac{B_0}{B\rho} \int_0^{\lambda_p/4} \sin \frac{2\pi z}{\lambda_p} dz = \frac{B_0}{B\rho} \frac{\lambda_p}{2\pi} \tag{3.15}$$

where $B\rho$ is the beam rigidity and ρ is the bending radius. The strength parameter K is given by Equation 3.13. For wiggler magnets $K \gg 1$. This is because the magnetic fields are strong in wiggler magnets. The strong magnetic field creates a large deflection in the transverse direction such that transverse motion is also relativistic. Because of this the radiation spectrum is broader than $1/\gamma$ but the photon energy is peaked in the axis of the magnet since that is the direction of the strongest bend. Off axis the radiation is softer since it was generated at a point where the field is lower. When a beam is Δz away from the peak of the sine curve the deflection angle is

$$\theta_{\delta z} = \frac{1}{\rho_0}\frac{\lambda_p}{2\pi}\sin\frac{2\pi}{\lambda_p}\Delta z. \tag{3.16}$$

The critical photon energy can then be calculated at an angle ψ from the wiggler axis.

$$\epsilon_c = \epsilon_{c0}\sqrt{1-\left(\frac{\gamma\psi}{K}\right)^2} \tag{3.17}$$

The critical energy at a set deflection angle ψ is important when more than one experimental station is using the radiation from one wiggler magnet and all stations want hard radiation from the wiggler axis. To increase the deflection angle of hard radiation the pole can be lengthened to flatten the sinusoidal field crest.

3.3.2 Undulators

Wiggler magnets focus on producing hard x-rays and high intensity, while undulators are used to produce radiation with better photon beam quality and high photon brightness. Undulator insertion devices have a strength parameter, $K \ll 1$ because the magnetic field of the poles is less than that of the wiggler magnet. The smaller fields only weakly deflect the electron beam to angles less than $\pm 1/\gamma$, therefore the transverse motion is non-relativistic. The wavelength of the emitted radiation is given by the Lorentz contracted period length given by $\lambda_\gamma^* = \lambda_p/\gamma$. For infinite undulators the radiation will be monochromatic however for finite undulators used in light sources the radiation is quasi-monochromatic with a band width of $1/N_p$, where N_p is the number of poles in the undulator. In the laboratory frame the radiation is Doppler shifted. This radiation is still quasi-monochromatic with the fundamental wavelength of λ_γ given by Equation 3.18.

$$\lambda_\gamma \approx \frac{\lambda_p}{2\gamma^2} \tag{3.18}$$

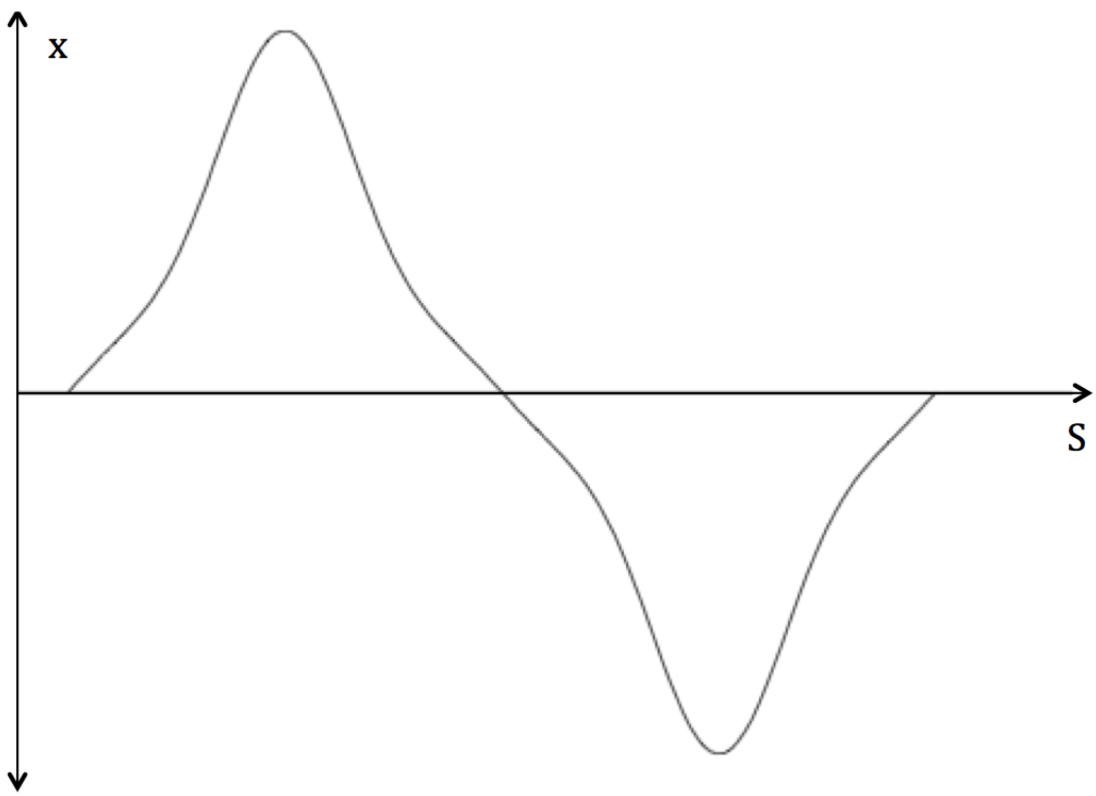

Fig. 3.4. Distortion of a sine wave by transverse relativistic motion [28].

If the strength parameter is increased by increasing the magnet field such that $K \sim 1$, the transverse motion becomes relativistic. This distorts the sinusoidal motion through Lorentz contraction of the longitudinal coordinate, Figure 3.4. This perturbation shows the odd harmonics of the fundamental frequency calculated in Equation 3.18. The radiation produced off axis has a larger fundamental frequency because it is not as strongly Doppler shifted. The fundamental frequency at an angle, θ, is described by the equation,

$$\lambda_1 = \frac{\lambda_p}{2\gamma^2}(1 + \frac{1}{2}K^2 + \gamma^2\theta^2). \tag{3.19}$$

This can also describe higher order frequencies, k, written in practical units in Equation 3.20,

$$\lambda_k(\mathring{A}) = 13.056 \frac{\lambda_p(cm)}{kE^2(GeV^2)}(1 + \frac{1}{2}K^2 + \gamma^2\theta^2) \tag{3.20}$$

and the critical energy is described by:

$$\epsilon_k(eV) = 950 \frac{kE^2(GeV^2)}{\lambda_p(cm)(1 + \frac{1}{2}K^2 + \gamma^2\theta^2)}. \tag{3.21}$$

If the magnetic field strength is increased more harmonics are visible and the on-axis spectrum begins to resemble that of the wiggler magnet, Figure 3.5. The spectral width of the radiation is described by:

$$\frac{\Delta\lambda}{\lambda} = \frac{1}{N_p}. \tag{3.22}$$

This equation shows that the more poles in an undulator the smaller the spectral width of the photon beam.

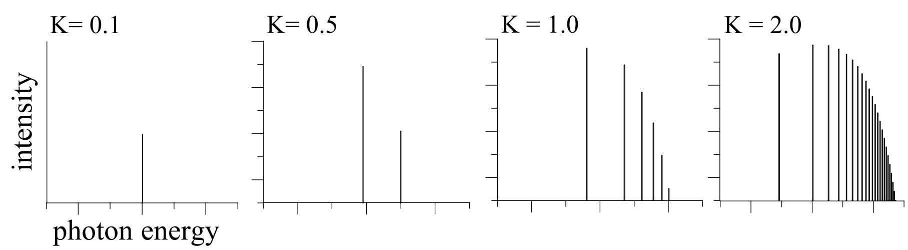

Fig. 3.5. Radiation spectrum of an undulator magnet as the strength parameter K increases [28].

4. SYNRAD3D

Synrad3D was used to compare an analytical model with measurements of radiation heating. Discussed in this Chapter will be the physics of Synrad3d including photon generation, an overview of diffuse scattering and how to use Synrad3D.

Synrad3D [30] is a Monte Carlo photon tracking code, using the Better Methodical Accelerator Design (BMAD) [31] library to model the accelerator lattice. The photon scattering model used in the code has developed over the last three years to include diffuse scattering off technical surfaces. All reflections are assumed to be elastic, no loss in energy. The simulation does not include fluorescence or Compton scattering. This chapter will describe the physics included in Synrad3d.

4.1 Photon Generation

The program simulates the trajectory of N macro-photons. Macro-photons are generated based on synchrotron radiation integrals. Polarization of the photons is ignored. Synchrotron radiation integrals are a set of integrals that are commonly used in calculations of synchrotron parameters such as betatron oscillation, beam energy spread and horizontal emittance. Equation 4.1 is used to calculate the average number of photons emitted by a beam particle over one turn [31],

$$\aleph = \frac{5 r_f}{2\sqrt{3}\hbar c} I_0 \tag{4.1}$$

where c is the speed of light and r_f is the classical radius factor given by,

$$r_f = \frac{e^2}{4\pi\epsilon_0} = 1.4399644 * 10^{-9}\text{meters-eV} \tag{4.2}$$

for all particles with a charge of ± 1. I_0 is the radiation integral

$$I_0 = \oint ds \gamma_0 g. \tag{4.3}$$

The variable g is defined by $1/\rho$ where ρ is the bending radius of the magnet and γ_0 is the relativistic factor. The integral is taken along the path of the electron, around the accelerator ring. Therefore I_0 is only non-zero in sections of the ring that bend the path of the electron beam. This includes dipole magnets and off-axis beam in quadrupole magnets. A beam off-axis in a quadrupole magnet 'sees' a dipole field and produces synchrotron radiation.

Macro-photons are generated at longitudinal positions specified in the input file in the regions where I_0 is non-zero. The number of photons generated is weighted by the probability of a photon emission, defined by the local orbit and total number of generated macro-photons. Each macro-photon's initial angle is randomly generated using a probability function based on the standard angular spectrum of photons generated in a bending magnet from

$$\psi = \begin{cases} {}^{1}/_{\gamma} \left(\frac{\omega_c}{\omega}\right)^{1/3} & \omega << \omega_c \\ {}^{1}/_{\gamma} & \omega = \omega_c \\ {}^{1}/_{\gamma} \left(\frac{\omega_c}{\omega}\right)^{1/2} & \omega >> \omega_c. \end{cases} \tag{4.4}$$

where ω is the photon wavelength and ω_c is the critical wavelength of the radiation produced in the bending magnet. According to this equation radiation with shorter wavelengths has a small opening angle, while radiation with a longer wavelength can have a large opening angle.

4.2 Photon Reflections

Including photon scattering the photon distribution on the chamber wall changes. Physics of the photon reflectivity was explored to determine the final photon positions.

Synrad3D uses data from the Berkeley Center for X-Ray Optics [32] to determine the probability of reflection of each macro-photon as a function of photon energy and grazing angle. Figure 4.1 is an example of a reflectivity curve for aluminum with a 10 nm copper layer. The dipole spectrum is from an APS main bending magnet.

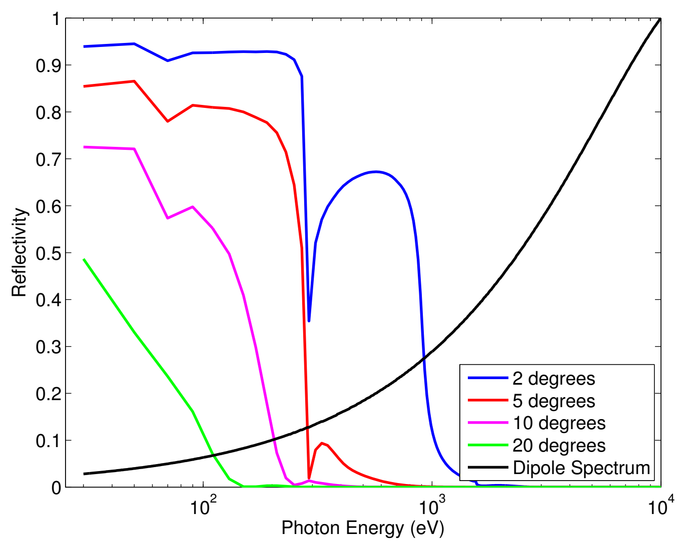

Fig. 4.1. Example of photon reflectivity for an Aluminum substrate with a 10 nm copper layer. Taken from the Berkeley Center for X-ray Optics.

The addition of diffuse scattering in Synrad3D was prompted from research into the surface roughness of the vacuum chamber wall. Initially the code assumed 2 nm rms surface roughness which indicates a negligible amount of diffuse scattering, Figure 4.2. However measurements of the APS beam chamber roughness showed a surface roughness of 139 nm for a polished chamber, and 1180 nm for an non-polished beam chamber [33]. The implementation of diffuse scattering is discussed in subsection 4.2.2.

4.2.1 Specular Scattering

For very smooth surfaces the photons can be assumed to specularly reflect off the beam chamber. The probability of an incident photon being reflected is dependent on the photon energy, incident angle and material it is scattering from. The Berkeley database provides the flexibility to vary the substrate material and roughness as well

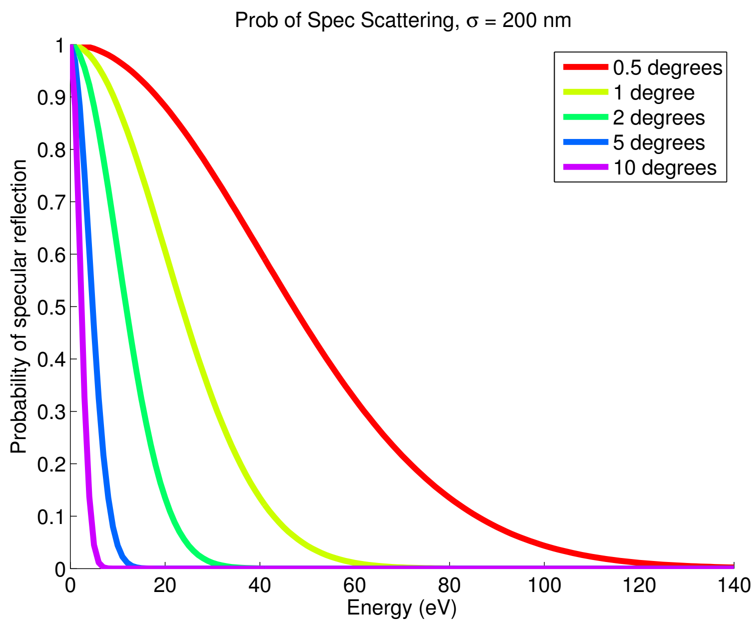

Fig. 4.2. The probability a photon specularly reflects off the chamber surface, assuming a surface roughness of 200 nm rms.

as the roughness and thickness of a top layer. The first version of Synrad3D assumed a 8 nm layer of Al_2O_3 forms on the surface of the aluminum beam chamber with a roughness of 2 nm rms [30]. After a comparison to reflectivity measurements made at Daphne the surface material was updated to a 10 nm Carbon layer on the Aluminum substrate [34].

The default chamber wall is assumed to have a 10 nm copper layer on an Al substrate. The surface parameters were determined by comparing specular reflectivity measurements taken at Daphne [13] with the reflectivity curves from Berkeley Center for X-Ray Optics.

4.2.2 Diffuse Scattering

Evidence for diffuse scattering being an important parameter in describing the absorbed photon distribution was shown. Diffuse scattering dominates when $\sigma/\lambda >> 1$, where σ is the rms surface roughness of the beam chamber and λ is the photon wavelength. At APS the beam chamber rms roughness has been measured as 139 nm for a polished chamber and 1180 nm for an unpolished chamber, which is much greater than the critical wavelength of photons emitted from the bending magnet, 0.0653 nm.

4.3 Beam Steering in Synrad3D

To compare simulations with the analytical model developed in chapter 6, simulations of an off-axis electron beam in Synrad3D were needed. The steering magnet field for set orbit bumps in the main bending magnet was calculated using the particle accelerator simulation code, Tao [35]. To calculate the corrector strengths Tao minimizes the error at a set of specified beam position monitors by varying the strength of the correctors.

5. ACCELERATOR PARAMETERS

This chapter will describe the magnetic lattice of the Advanced Photon Source accelerator, as well as describe the assumptions made in the radiation heating model and simulations.

5.1 Accelerator Parameters

The SCU studied was installed the Advanced Photon Source in December 2012 and commissioned in January 2013. The parameters for the accelerator are given in Table 5.1.

Table 5.1
Parameters for the Advanced Photon Source.

Parameter	**Value**
Electron Beam energy	7 GeV
Nominal Beam Current	100 mA
Ring Circumference	1104 m
Revolution frequency	271.554 kHz
Revolution time	3.682 μsec
Number of sectors	40

The order of magnets in a particle accelerators are called the lattice. The lattice design of storage rings use a periodic structure. APS has a periodicity of 40. Each repeated section is known as a sector and therefore APS has 40 sectors. Most of the sector, 21.6 m, is composed of electromagnets to focus, steer and bend the electron beam, Figure 5.1. Two large bending magnets, and two small bending magnets are sources of the synchrotron radiation heating of the SCU. In [36] Glenn Decker proposed using two horizontal correctors in each sector to keep the radiation from the large bending magnets from contaminating the X-ray Beam Position Monitor (BPM) signal. These two corrector magnets, labeled AH1 and BH1, are no longer used for horizontal corrections of the beam path. The modification, named after him, is is known as the 'Decker Distortion'. Each sector ends in a straight section, 5.78 m long, where ID's, such as the SCU, are installed.

5.2 Sector layout

The straight section which contains the SCU begins 4.842 m after the end of the bending magnet (BM); the full length of the straight section is 5.78 m. In the first half of the sector contains a hybrid permanent magnet undulator and the SCU in the downstream end.

The second bending magnet in the sector, BM, creates radiation that can directly heat the SCU, shown schematically in Figure 5.2. Therefore unless otherwise stated, all the calculations presented in this thesis will focus on the radiation from BM to the end of the SCU. The first part of this section will describe the general layout of the area of interest, then will describe the chamber shapes, and how they were modeled for simulations. The section will end with a timeline of design changes to be referenced in later chapters.

SCU0 was installed in the last 2 m of the sector 6 straight section, approximately 10 m from the end of BM. To shield the SCU chamber from direct radiation from BM a photon absorber is placed approximately 30 cm before the entrance to the SCU. With the tip 17 cm from the chamber center, this creates 1.43 mm clearance between the radiation fan and the end of the chamber, as shown in Figure 6.1. The photon absorber has an angle of 30 degrees with respect to the beam path [38].

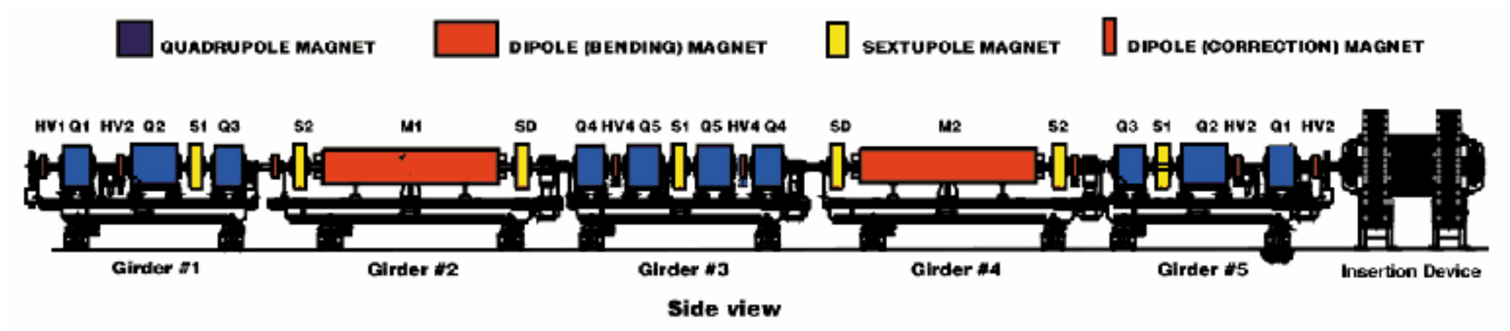

Fig. 5.1. One sector of the APS ring. [37]. The length of one sector of APS is 21.6 m.

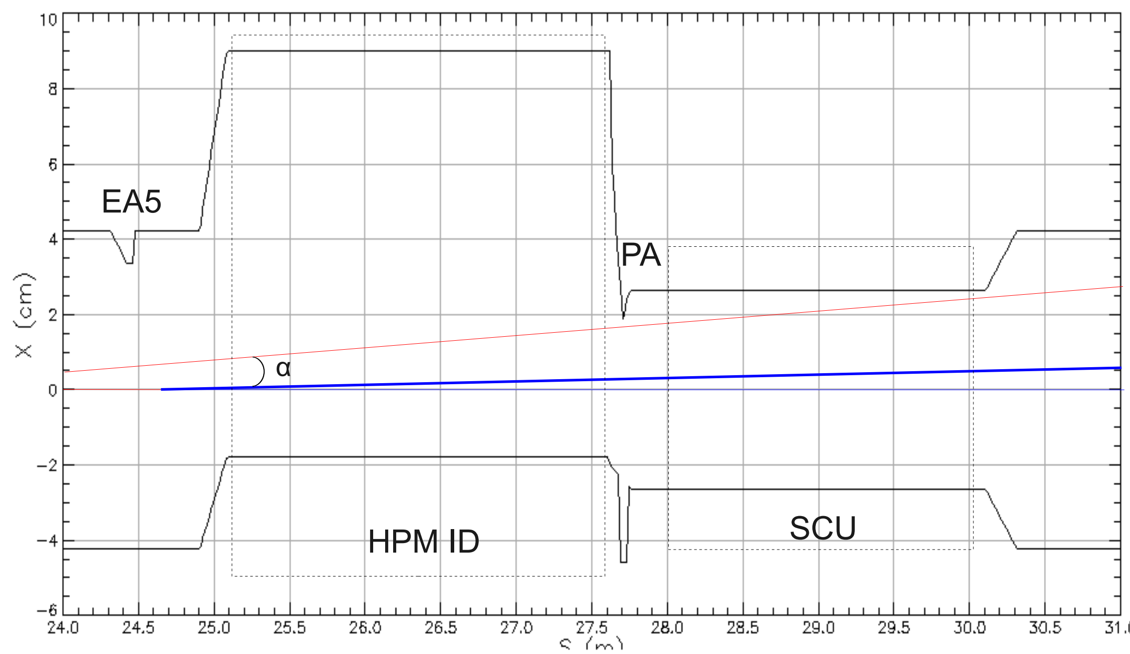

Fig. 5.2. Horizontal radiation fan from the second bending magnet, and Decker Distortion. Shown is radiation from an on-axis electron beam.

5.3 Hard edge model approximation

The APS main dipole field has a magnetic core length of 3.0 m and an effective magnetic length of 3.0547 m, shown in Figure 5.3. But the calculations and simulations done for this thesis assume hard edge magnetic model, which means that the magnetic field is assumed to be constant along the length of the core, and does not include the fringe field. This is a conservative assumption, because the radiation incident on the SCU is generated in the fringe field. Photons generated in the fringe field would have a lower energy spectrum, decreasing the absorbed power.

5.4 SCU Chamber Ellipse

The SCU chamber is based on the standard ID chamber. This chamber has a vertical aperture of 7.2 mm and a horizontal aperture of 53 mm. The top and bottom

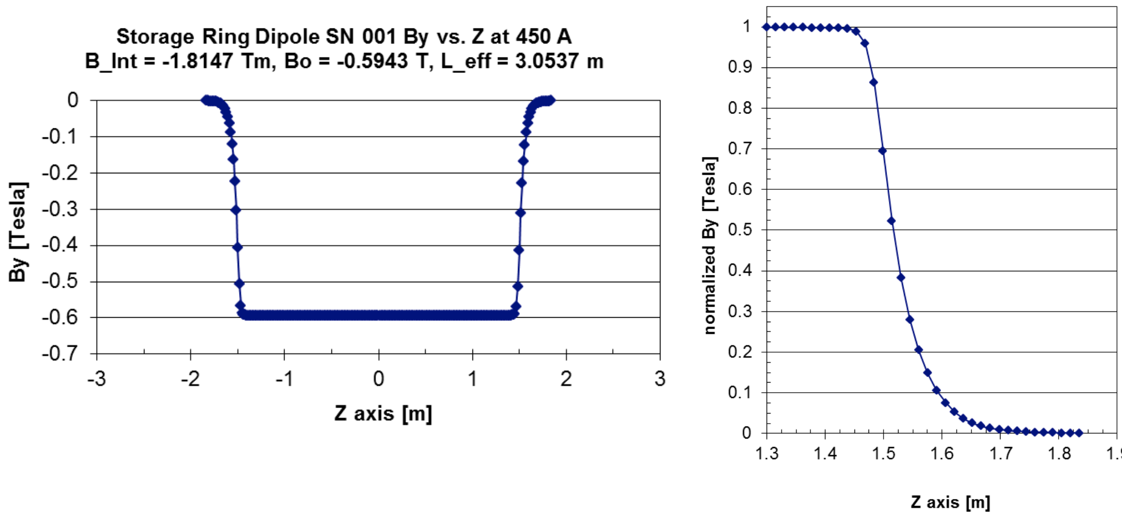

Fig. 5.3. Hall probe measurement of the magnetic field of the main dipole magnet. The core length of the magnet is 3 m, and the effective magnetic length is 3.0547 m [39].

of the chamber is an ellipse with major and minor axis of 53 mm and 7.2 mm, respectively. The top and bottom ellipses were modeled as straight lines. The lines angle from the center of the chamber at the maximum aperture out to 24 mm to the half circles on each end, Figure 5.4.

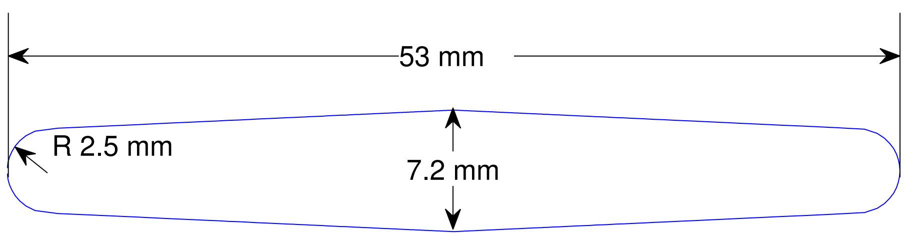

Fig. 5.4. Modeled cross section of the SCU ellipse chamber

5.5 Surface Roughness Calculation

Two samples were taken from sections of extruded aluminum APS beam chamber. The first, an as-received sample, Tabor Metals in 2001, was extruded from Aluminum 6063-T5. The polished sample, made by Cardinal Aluminum in 2011, was extruded from Aluminum 6063-T5. The sample was polished using an abrasive flow process [40].

Table 5.2

Sample Surface Parameters

Sample	**RMS**	**Correlation length**
As-received	1180 nm	3.8μm
Polished	139 nm	2.4μm

The surface roughness of both samples were measured by the Metrology group at APS, using a MicroXAM surface profiler with an objective lens with 20X magnification [41] the results are in Table 5.2. The RMS roughness is calculated as the root-mean-squared average of the chamber profile. The correlation length is calculated using the autocorrelation function given by

$$r_k = \frac{\sum\limits_{i=1}^{N-k} (x_i - \bar{x})(x_{i+k} - \bar{x})}{\sum\limits_{i=1}^{N} (x_i - \bar{x})^2}, \tag{5.1}$$

where r_k is the autocorrelation coefficient, x is the measured surface height, N is the number of data points and k is the offset. This equation compares the height of the surface with itself offset by some value dx, represented by k.

The results of this measurement were used in the photon scattering simulations described in chapter 7 and the quantum efficiency measurement described in chapter 9.

6. ANALYTICAL MODEL

The power incident on the SCU0 beam chamber from primary photons can be calculated through ray tracings and analytically. Ray tracings are 2D projections of the dipole radiation fan on the 3D vacuum system layout. Ray tracings do not include the vertical distribution of the dipole radiation. So analytical calculations were performed to include the vertical distribution of photons. Ray tracings were used to benchmark the steering model when the electron beam is off-axis through the upstream dipole magnet.

This chapter describes the steps taken to create a full analytical model. For the analytical calculation we make the conservative assumption that all photons incident on the beam chamber are absorbed.

6.1 Ray Tracings

Traditionally ray tracings are used to confirm that accelerator components other than photon absorbers are protected from in-plane radiation, because ray tracings assume the synchrotron radiation has a horizontal opening angle equal to the bending radius of the magnet, and no vertical distribution. The SCU photon absorber is designed so that no direct radiation is incident on the SCU chamber for an on-axis electron beam. The initial analytical model compared the radiation clearance at the end of the SCU to a ray tracing from Mark Jaski of APS [42]. The clearance is the distance between the radiation fan and horizontal edge of the beam chamber, shown as a red line in Figure 6.1. Results are shown in Table 6.1 for Layout 3 described in subsection A.2.3.

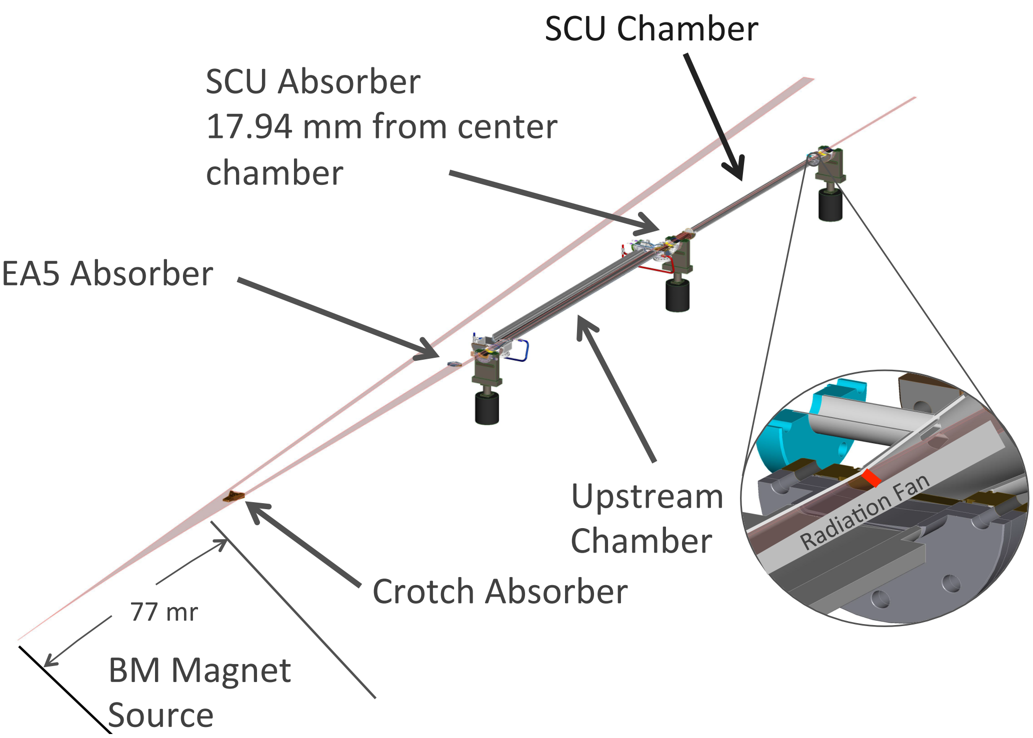

Fig. 6.1. Ray Tracing of the BM radiation. The radiation clearance is shown as the red line in the highlighted section.

Table 6.1
Clearance calculation. The clearance is marked by the red line in Figure 6.1.

Calculation Method	**Clearance**
Ray Tracing	1.42 mm [43]
Analytical Model	1.43 mm

6.2 Benchmarking Steering Model

Generally ray tracings assume an ideal machine and beam trajectory, however they can be used to calculate the radiation fan for a source that is off-axis. These ray tracing results were used to benchmark the horizontal steering model used in the analytical calculation of radiation heating. The trajectory of the electron beam through the upstream dipole magnet is defined by two parameters, the beam offset and angle, referenced to the dipole exit. For a range of horizontal steering values direct dipole radiation heat load on the SCU chamber can be calculated. For all other steering values it is assumed there is zero heat load, since the SCU photon absorber shields the chamber from direct radiation. For comparison with ray tracings the heat load from incident radiation is calculated as the fractional power of synchrotron radiation that is intercepted by the beam chamber, Equation 6.1,

$$P(\alpha) = P_{dipole}\left(\frac{\beta}{\theta_{dipole}}\right) \tag{6.1}$$

where β is the angle of radiation subtended by the SCU chamber, θ_{dipole}, defined in Table 6.2, is the bending angle of the dipole and P_{dipole} is the total power produced by the dipole magnet given by

$$P_{dipole}[kW] = 14.07928L[m]E^4[GeV]I[A]\rho^{-2}[m]. \tag{6.2}$$

The variables are described in Table 6.2, with the values for the APS main bending magnet which produces 6.6 kW of power per 100 mA of beam current.

Table 6.2
Variables for synchrotron radiation power calculation

Variable	**Description**	**Value**
L	Length of magnet	3.0 m
E	Beam energy	7 GeV
I	Total current	100 mA
ρ	Bending radius	39 m
θ_{dipole}	Angle of the dipole	77.5 mrad

As the beam position through the bending magnet changes the radiation source point also changes. The source point is the position along the curved trajectory of the beam in the bending magnet, in which the radiation produced just passes the SCU photon absorber. To calculate the source point use the equation:

$$S = \frac{\alpha}{\theta_{dipole}} * L, \tag{6.3}$$

Where S is the source point, and α is the angle of radiation that passes the SCU photon absorber. The value of α is dependent on the source point so to get an accurate value for the source point Equation 6.3 is solved iteratively until convergence. Using the correct value for the source point is important because it changes the opening angle of the radiation fan incident on the SCU chamber wall, and the heat load calculated from the analytical model.

Results from the heat load calculation are shown in Figure 6.2. The horizontal angle ($\pm$4.62 mrad) and offset ($\pm$13 mm) ranges modeled are the maximum possible horizontal orbits. Due to the wide horizontal aperture of the beam chamber, only for steerings exceeding -5 mm there is a concern about radiation heating. The power on the outside edge ranges from 0.3 W to 22.8 W, increasing for the larger negative offsets. For positive offsets the photon absorber shields the beam chamber. If we define the horizontal steering limit to be when the radiation fan begins to intercept the outside edge of the beam chamber the analytical model agrees with the ray tracings. The steering limit defined by ray tracings is shown as the red dashed line in Figure 6.2. Calculations were done using Layout 3 described in subsection A.2.3.

6.3 Vertical radiation distribution

The vertical distribution of synchrotron radiation was added to the analytical model. The dipole radiation opening angle is described by Equation 4.4.

The power produced by a dipole magnet integrated over all photon frequencies is given by [44, 45]

$$P\left(\mathrm{W/mrad^2}\right) = P_{dipole}\,\frac{\alpha}{\theta_{dipole}}\,\left(\frac{1}{\left(1+X^2\right)^{5/2}}\left[1+\frac{5}{7}\frac{X^2}{1+X^2}\right]\right); \quad X = \gamma\psi. \tag{6.4}$$

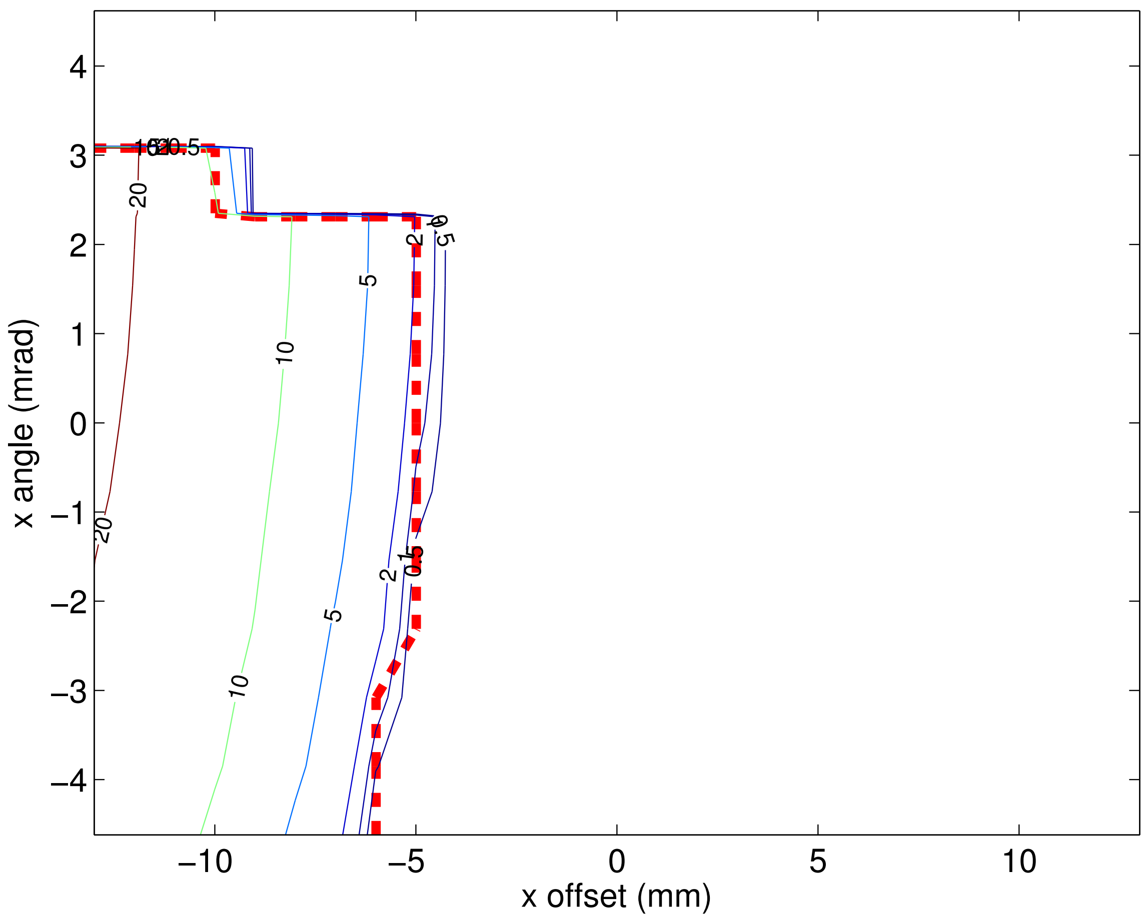

Fig. 6.2. Calculated heat load for a horizontally off-axis electron beam in the upstream dipole. Contours indicate analytical calculation of synchrotron radiation power in Watts, while red dotted line indicates steering limit calculated using ray tracings. Power is shown in Watts.

P_{dipole} is the total power produced by the dipole magnet, from Equation 6.2. The ratio, α/θ_{dipole}, calculates the fractional power that passes the SCU photon absorber. The part in parentheses describes the vertical distribution of synchrotron radiation power produced in a dipole.

The vertical angle between the source point and top of the chamber is defined as ψ. The power incident on the SCU chamber wall was calculated by integrating Equation 6.4 from ψ_1 to ψ_2, where ψ_1 is the angle between the source point and the top of the downstream end of the SCU chamber, and ψ_2 is the angle between the source point and upstream end of the SCU chamber, see Figure 6.3.

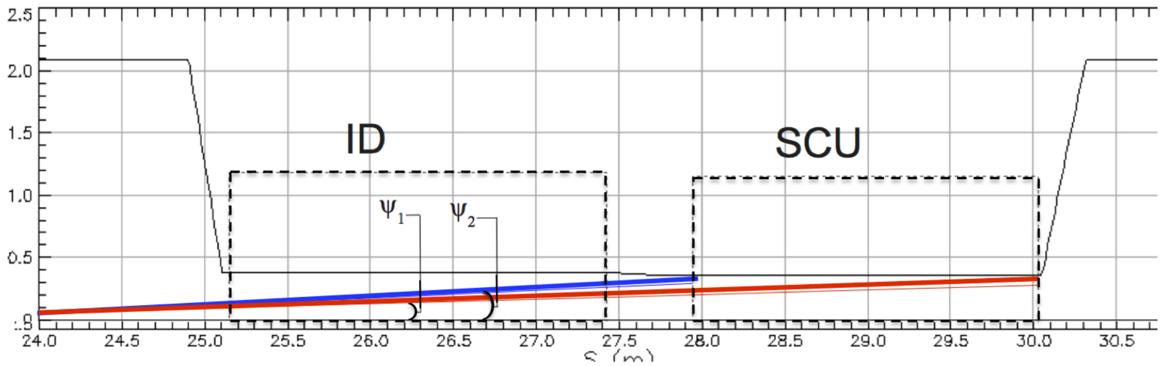

Fig. 6.3. Schematic showing the chamber cross-sections in the long straight drift section along the x = 0 plane. Here the blue line depicts the limit of the vertical radiation fan that just intercepts the top of the SCU chamber at the upstream end of the cryomodule and the red line depicts the fan that just intercepts the top of the chamber at the downstream end.

To speed up the computation the integral was computed analytically from ψ to infinity. This gives Equation 6.5, the fractional power incident on the SCU chamber from the source point downstream to the angle ψ.

$$F = 1.3125\left[16 - \frac{1}{21}\left(\psi\,\frac{3+4\psi^2(7+4\psi^2)}{(1+\psi^2)^{5/2}}\right)\right] \tag{6.5}$$

Using this method the equation to calculate the power on the SCU chamber is given by,

$$\begin{aligned} P = \left(\mathrm{W/mrad}^2\right) = P_{dipole}\,\frac{\alpha}{\theta_{dipole}}\,1.3125\,&\left[-\frac{1}{21}\left(\psi_2\,\frac{3+4\psi_2^2(7+4\psi_2^2)}{(1+\psi_2^2)^{5/2}}\right)\right] \\ &+\left[\frac{1}{21}\left(\psi_1\,\frac{3+4\psi_1^2(7+4\psi_1^2)}{(1+\psi_1^2)^{5/2}}\right)\right]. \end{aligned} \tag{6.6}$$

This speeds up the computation time because the program is no longer doing the integration for each set of $\psi_{1,2}$.

For example, from layout 1 in subsection A.2.1, the vertical angles $\psi_1 = 4.67/\gamma$ and $\psi_2 = 3.32/\gamma$ were calculated at y_1=2.75 mm ($x_1 = 18.65$ mm) and y_2=2.46 mm ($x_2 = 25.0$ mm). Using Equation 6.6 the radiation that passes the photon absorber and is intercepted and absorbed on the walls is, $P = 6650\ W \times 0.025 \times (0.00391 - 0.00108)$, or 0.426 W per 100 mA stored electron beam current.

As discussed in section 5.4, the SCU chamber is elliptical and not rectangular. By calculating the absorbed power using the minimum vertical apertures the estimated power on the SCU is over-estimated, which is conservative. Repeating the same calculation using the vertical apertures on the inside edge of radiation, the power absorbed on the SCU is underestimated, reducing the power to 0.136 W from the 0.426 W calculated before. To calculation is numerically integrated over the elliptical chamber to get a better model of radiation heating. The horizontal coordinate, x, was divided into N sections with ψ, the vertical opening angle, calculated for each x. After the integration along x the radiation power on the SCU is 0.238 W.

The steering model was then added to this calculation, to be able to more accurately estimate the radiation heat load from an off-axis electron beam.

6.3.1 Horizontal Steering

When the radiation fan vertical distribution is added to the horizontal steering model described in section 6.2 there is no longer a defined line when radiation is incident on the chamber walls. Figure 6.4 is a contour plot of the heat load on the beam chamber when the electron beam is off-axis in the upstream bending magnet. The values were calculated using Layout 4 described in subsection A.2.4. The contour plot shows that large negative offsets through the dipole magnet produce the most power incident on the SCU0 beam chamber. The maximum heat load values are lower than those calculated in section 6.2 because the design of the SCU photon absorber is 17 mm from the beam chamber center, in Figure 6.4. By making this 1 mm change in SCU photon absorber position we were able to relax the steering limits on the electron beam.

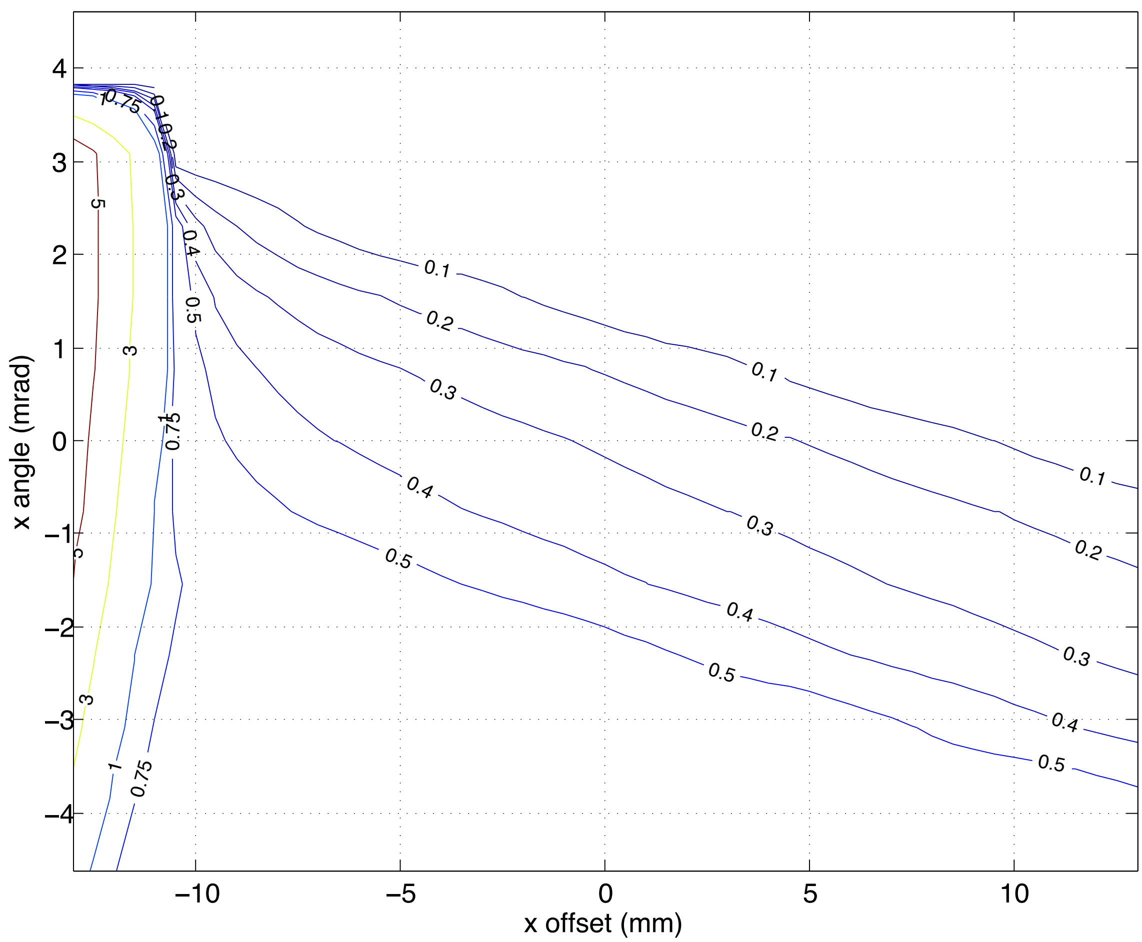

Fig. 6.4. Analytical calculation of radiation power incident on the SCU0 beam chamber for a beam horizontally offset in the upstream bending magnet. Power is shown in Watts. $(y = y' = 0)$

Studies were done Fall 2011 to determine the greatest possible horizontal steering through 6BM, using a one sector orbit bump. These studies showed that the maximum beam offset ranged from 1.4 mm to -2.7 mm and the maximum angle was 0.3 mrad to -0.72 mrad. This horizontal steering does not exceed that which shields the cryostat from on axis radiation.

6.3.2 Vertical steering

The calculation described in section 6.3 assumes the heat load is symmetric on the top and bottom of the beam chamber. That symmetry is broken when the radiation fan is no longer centered at $y = 0$ which occurs when the electron beam is steered vertically through the upstream bending magnet. To account for this change the power on the top and bottom of the chamber are calculated separately, then added together,

$$P_{vert} = \frac{P_{top}(\psi_1, \psi_2)}{2} + \frac{P_{bottom}(\psi_1, \psi_2)}{2} \tag{6.7}$$

where P_{top} and P_{bottom} are calculated from Equation 6.6 using ψ_1 and ψ_2 as defined as the angle to the top or bottom of the chamber.

Figure 6.5 is a contour plot of the the heat load on the SCU for beam steered vertically off-axis in the upstream bending magnet. Because of the smaller vertical aperture, less steering provides a greater heat load than in the horizontal direction. The incident power can reach over 100 W of power for relativity small vertical angles in the dipole.

The heat load 'cut-off' at y = ±4 mm is because of the small chamber aperture, both the chamber for the upstream undulator and SCU. The upstream HPM has a vertical aperture comparable to that of the SCU0. This acts as a shield to the top and bottom of the SCU0 chamber. Second, the SCU0 chamber has a vertical half aperture of 3.6 mm. Photons produced above that position will be absorbed in the taper upstream of the SCU0 chamber.

Steering the beam vertically, it is possible to put over 100 W of radiation power on the SCU chamber during machine studies. However when the SCU is operating beam position limiting detectors (BPLD) are activated, which limit the electron beam position in the dipole. The allowed steering limits are shown in the box in Figure 6.5. This limits the heat load to 20 W.

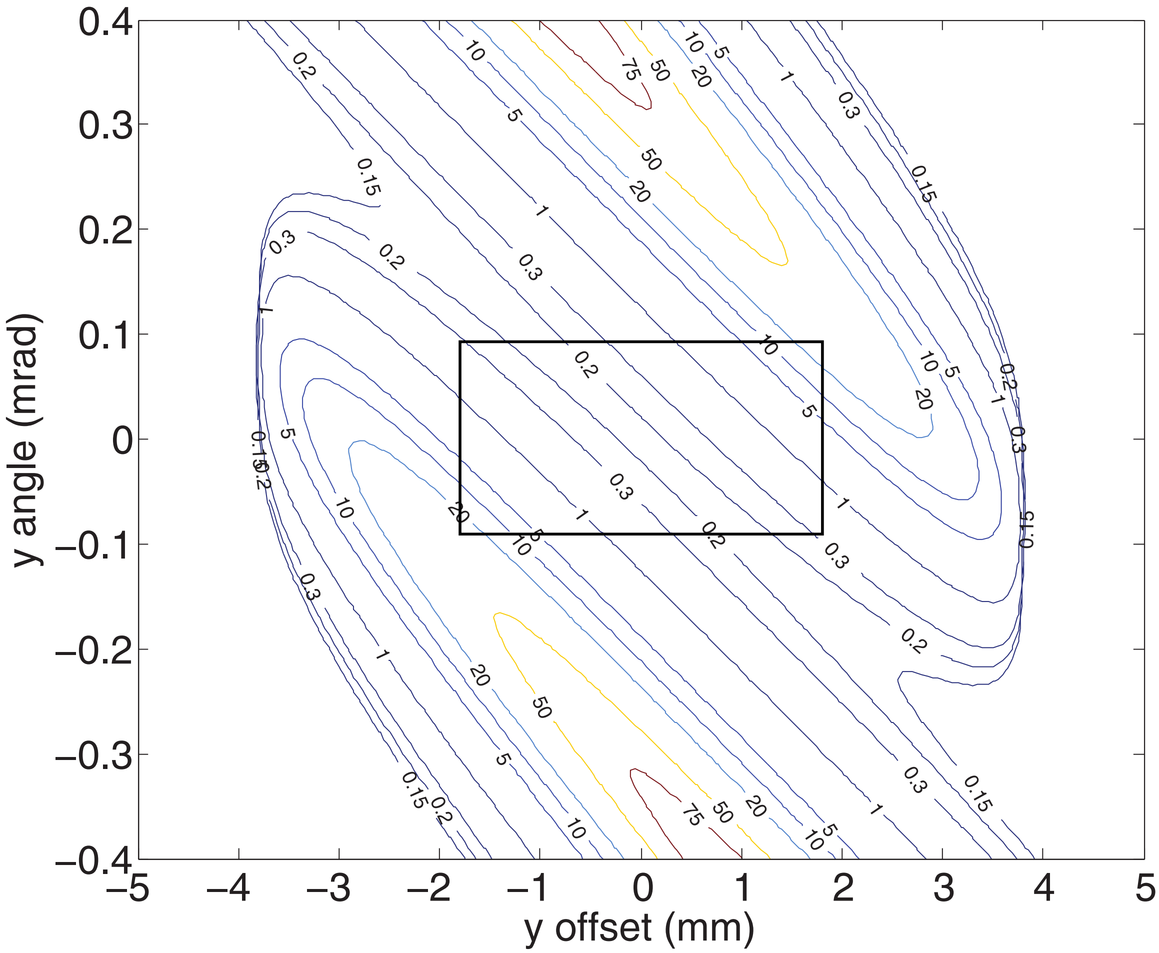

Fig. 6.5. Power incident on the SCU0 cryostat for a beam that is off-axis vertically through the upstream bending magnet. Power is shown in Watts. ($x = x' = 0$)

6.4 BH1 Corrector Heat Load

The same calculation was applied to the Decker distortion [36], small bending magnet, to determine steering limits of the electron beam through this magnet. The total power produced by this magnet is calculated from Equation 6.2. Using the values in Table 6.3 the total power is 21.1 W per 100 mA. The photon absorber does not intercept any of the radiation from the corrector.

Table 6.3
Variables for synchrotron radiation power calculation for the small bending magnet used in the Decker distortion.

Variable	**Description**	**Value**
L	Length of magnet	0.16 m
ρ	Bending radius	160 m
θ_{dipole}	Angle of the dipole	1 mrad

Because the critical energy of the mini-bend is two orders of magnitude lower than that of the main bend its contribution to the total heat load is less, and steering the beam off axis through BH1 has little effect on the total power absorbed. Large angle and offsets, or a combination there of, are needed to increase the heat load, as illustrated in Figure 6.6.

When the SCU0 is operating the BPLD's are armed which controls the beam position. Although no studies were done to determine the limits of the electron beam orbit through this small dipole the orbit is constrained because it is closer to the ID's.

6.5 Summary

The basic heating model and steering model were benchmarked on well understood ray tracings. This helped define important parameters that were included in the program, including a source point calculation. Using this analytical model it was shown that an electron beam off-axis in the upstream dipole can produce more radiation heating on the SCU chamber wall than it is designed to take. Precautions were taken to mitigate radiation heating by limiting the beam steering during operations.

Because vertical steering has the ability to create more heating, comparison studies will only focus on the vertical steering model. Radiation heat loads from the small BH1 dipole are reasonable. Large heating values from this magnet require large electron beams offset, with are not possible during SCU operations.

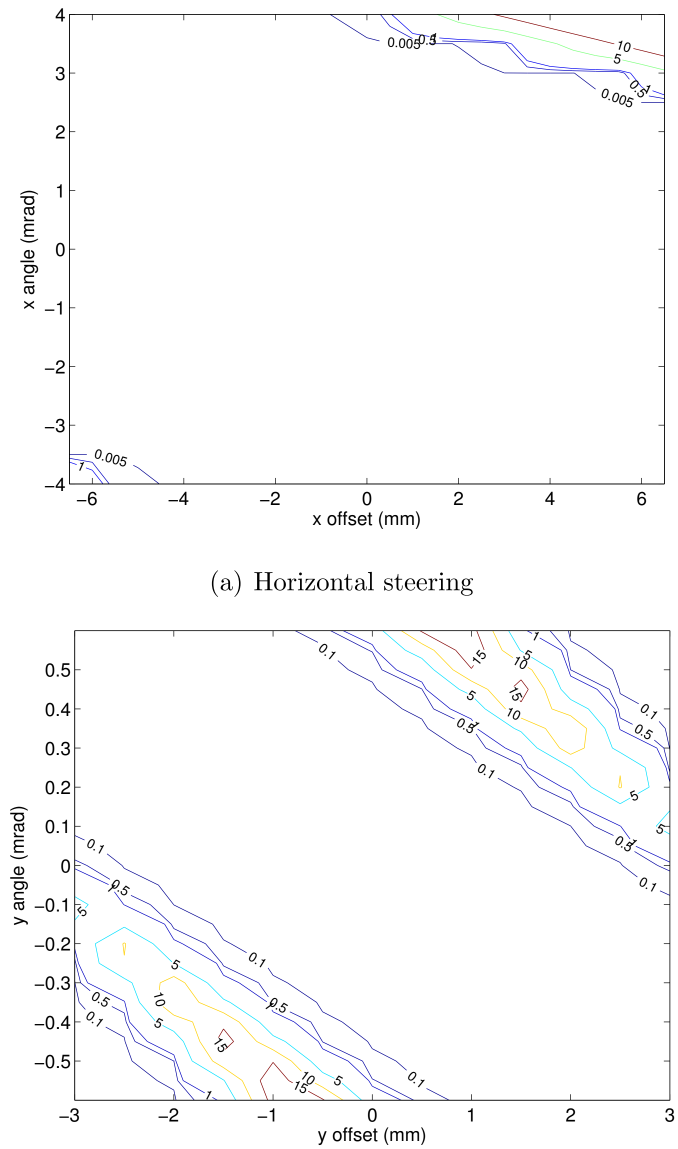

(a) Horizontal steering

(b) Vertical steering

Fig. 6.6. Analytical calculations of the radiation heating on the SCU chamber from an off-axis beam in the small dipole, BH1. Calculated using Layout 4, subsection A.2.4. Power in Watts.

7. SYNRAD3D RESULTS

Synrad3D models the effects of photon scattering on the distribution of radiation heating. The program was used to benchmark the vertical steering model described in subsection 6.3.2, and simulate the distribution of heating from reflected photons. This chapter outlines the method used to calculate the radiation heating from the simulation results, and show the comparison with the analytical calculation for an off-axis electron beam. With the addition of scattering the importance of diffuse vs. specular scattering will be shown and the effect that it has on the photon distribution.

7.1 Analysis of simulation results

As a Monte Carlo program, Synrad3D models N macro-photons as they travel through the vacuum chamber. Details on the physics implemented in the program were given in chapter 4.

By varying the input parameters specific sections of radiation production and absorption could be studied. This was used to study the heat load from the main bending magnet only, when comparing results with the analytical model. Similarly only macro-photons absorbed in the SCU, or region of interest were included in the output file. By creating active filters within the simulation it was possible to increase the statistics for areas that were shielded by a photon absorber or upstream chamber.

The output of Synrad3D contains a matrix with data for each macro-photon simulated. This included photon index number, energy, start and end positions and direction. If scattering was included in the simulation, additional data was included in the output file. This included the scattering location(s), incidence angle and probability for reflection. This section outlines the analysis of the data and describes how the macro-photon data was used to calculate relevant information.

7.1.1 Power Calculation

The relationship between the energy of absorbed macro-photons and the synchrotron radiation heat load P is given by

$$P[W] = E_{TOT} \times F \times I, \tag{7.1}$$

where E_{TOT} is the sum of macro-photon energy absorbed, and I is the beam current in Amps. F is defined by $\aleph/N_{sim}$, $\aleph$ (given in Equation 4.1) is the average number of photons emitted by a particle in one turn and N_{sim} is the number of simulated photons. The value F is given as an output from Synrad3D, to include all photons generated, not just the ones written to the output file. Equation 7.1 was also used to calculate the power per unit length by dividing by the length of the chamber where photons were absorbed, L:

$$P_L = P/L. \tag{7.2}$$

7.1.2 Incident angle Calculation

To study the effects of photon reflectivity the incidence angle was analyzed. Each macro-photon's incidence angle relative to the surface normal $\theta_\perp$ was included in the output file. The grazing angle, θ_g, is the difference between the perpendicular angle, $\theta_\perp$, and $\pi/2$,

$$\theta_g = \pi/2 - \theta_\perp. \tag{7.3}$$

7.1.3 Flux Calculation

To compare simulation results with calculations on other machines the energy spectrum is presented as the energy flux of photons hitting a defined section of the beam chamber. Flux is presented in two ways, the photons/sec and the photons/sec/0.1% bandwidth, both calculations are described here.

Simulation results provide the number of photons incident on the beam chamber for one revolution of the electron beam. To plot the full spectrum use the equation:

$$Flux = N_i * F/t \tag{7.4}$$

where N_i is the number of macro-photons in energy range dE, and t is the time it takes for an electron to do one revolution, 3.69 μsec at APS. For the results shown in this thesis dE is 50 eV, chosen to be large enough to reduce statistical fluctuations in the simulation results.

Similarly, to calculate the photon flux in photons/sec/0.1% bandwidth

$$Flux = (Flux * B)\left(\frac{E}{dE}\right) \tag{7.5}$$

where B is the bandwidth, 0.1% and E is the photon energy.

7.2 Benchmark no reflection case

Synrad3D was used to benchmark the analytical model described in chapter 6, which assumes no photon reflections. The chamber geometry assumed in these simulations was Layout 1, described in subsection A.2.1. The SCU chamber has been divided into four sections outlined in Figure 7.1. Sections 1 and 4 have a temperature gradient from room temperature to 20K, and is the shape of the SCU chamber aperture is oval. Section 2 is the step from the SCU oval to SCU ellipse and, section 3 is kept at 20K and is the shape of the SCU ellipse.

Simulations were compared with the analytical results for an un-steered beam. This comparison is shown in Table 7.1 for the total power from both the main dipole magnet and mini-bend, BH1. As can be seen in Table 7.1. The results of the analytical model are in good agreement with Synrad3D, in the total heat load, and the heating on each section separately.

Table 7.1
Calculated Heat Load on the SCU0 chamber from Primary Photon Radiation, see Figure 7.1 for section definitions

Section of the Cryostat	**Simulation**	**Analytical Calculation**
S_1	0.0063 W	0.0066 W
S_2	0.058 W	0.058 W
S_3	0.185 W	0.174 W
S_4	7.55×10^{-5} W	8.28×10^{-5} W
Total	0.249 W	0.238 W

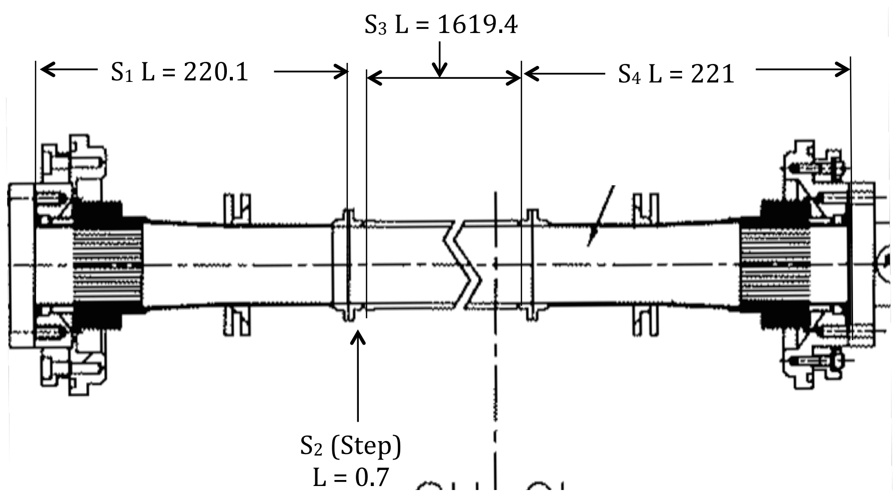

Fig. 7.1. Section definition for the heat load in each part of the SCU cryostat, for Tables 7.1 and 7.2. Lengths are in mm.

7.2.1 Introduction of a mask in ID6

The step from the SCU oval to the SCU ellipse in the cryostat increases the power on section 2 of the beam chamber in the cryostat. The heat load on this one section accounts for approximately 24% of the total direct radiation heating, on a 1 mm section. To decrease the heating on the taper in the SCU cryostat, a mask was added to the upstream end of section 1. This mask has the same shape as the SCU ellipse, is 1.3 mm in length and is 22.1 cm from the step in the SCU cryostat. The addition of the mask is effective in decreasing the heat load on section 2 by 75%. The power as a function of horizontal position on the step, with and without the mask, are compared in Figure 7.2.

Table 7.2 compares the heat load from primary photons on each section of the SCU cryostat with the mask. Comparing those with the heat load without the mask, Table 7.1, it can be seen that the mask is effective in shielding the step in the cryostat (S_2) from direct radiation.

Table 7.2
Calculated Heat Load on the SCU0 chamber from Primary Photon Radiation with the mask, see Figure 7.1 for section definitions.

Section of the Cryostat	**Simulation**	**Analytical Calculation**
S_1	4.96×10^{-5} W	5.17×10^{-5} W
S_2	0.016 W	0.012 W
S_3	0.185 W	0.174 W
S_4	7.64×10^{-5} W	8.28×10^{-5} W
Total	0.201 W	0.186 W

From the total power, the power density on a small area, dA, was calculated. Without the mask this area, dA, is the full vertical height of the step, and some small dx horizontally. When the calculation is repeated with the mask, the radiation is no longer absorbed along the full vertical height of the step; this decreases dA. 7.3(a) is a plot of the peak power density and an estimate of the rate of change in the temperature. The peak power density on the step is the same with and without the mask but the area is smaller by about 90%. From the power density a simple

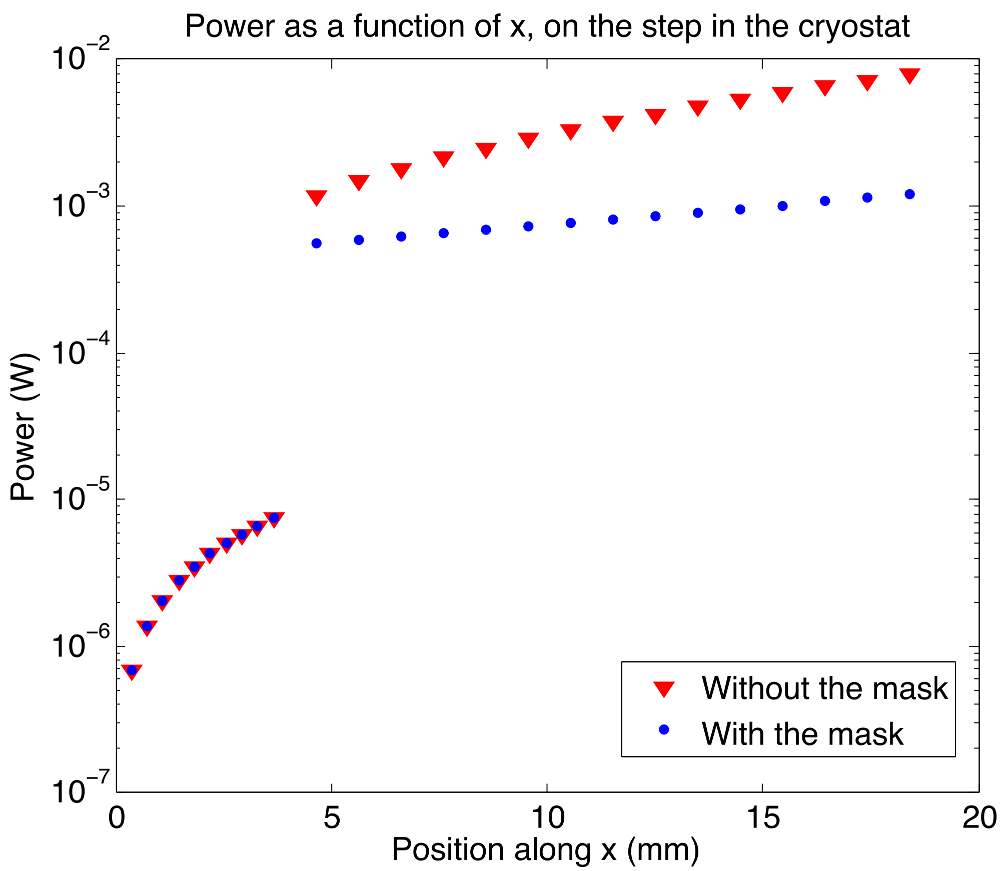

Fig. 7.2. Power absorbed on section 2 in the cryostat. This plot compares the power with and without the mask shielding section 2. The heat load between x = 0 and 3.5mm is generated from the mini-bend, the power at x > 3.5mm is from the main bend.

estimation was made of the change in temperature on the small taper. Assuming a material of volume 1 mm^3, the rate of temperature change was calculated using the equation

$$\frac{\Delta T}{\Delta s} = \frac{Pd}{\rho C_p}, \tag{7.6}$$

where Pd is the power density in W/mm^3, ρ is the density of the aluminum chamber, 2.7 g/cm^3 [46] and C_p is the specific heat of aluminum, 8.85 J/kgK at 20 K and 953.9 J/kgK at 300 K [47], shown in 7.3(b).

The final chamber design installed in the ring did not have the step or the mask due to the large radiation heat load . So none of these calculations were tested against measured heat loads. They were used to benchmark the analytical model.

7.3 Effect of Steering

To validate the analytical steering model Tao, a program for modeling accelerator optics, was used to create a vertical offset and angle of the electron beam through the dipole. Shown in this analysis is only the radiation produced in the bending magnet, to benchmark the results from the analytical model. If the full sector steering was modeled we would have to include the heat load from an off-axis beam in a quadrupole magnet in the analytical model. However the radiation heating from off-axis quadrupole fields are small compared the main bending magnet, so they can be considered a small contribution, in the measured data.

For our comparison only vertical orbit bumps were used because they produce more heating on the beam chamber than comparable horizontal orbits.

7.3.1 Vertical angle

By varying the corrector strengths we can define a known electron beam steering through the dipole magnet, considering only a vertical angle we can compare the results with the analytical model. For large vertical angles through the dipole magnet the steering couples into the horizontal axis, this error must be included in the analytical model when calculating the heat load. The coupling comes from the beam being off-set in the sextuple magnets upstream and downstream of the main dipole. Figure 7.4 compares the two models with good agreement. The Synrad3D

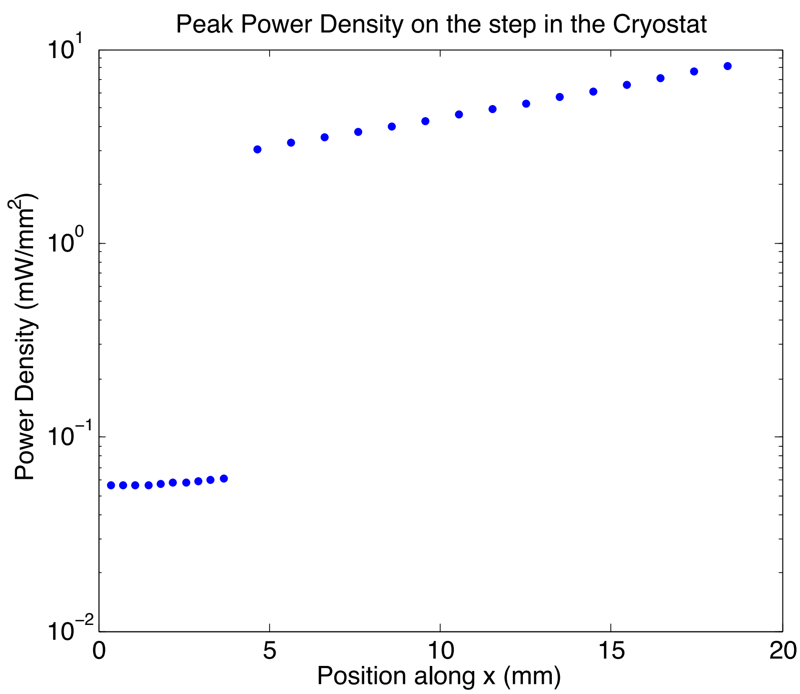

(a) Peak Power Density

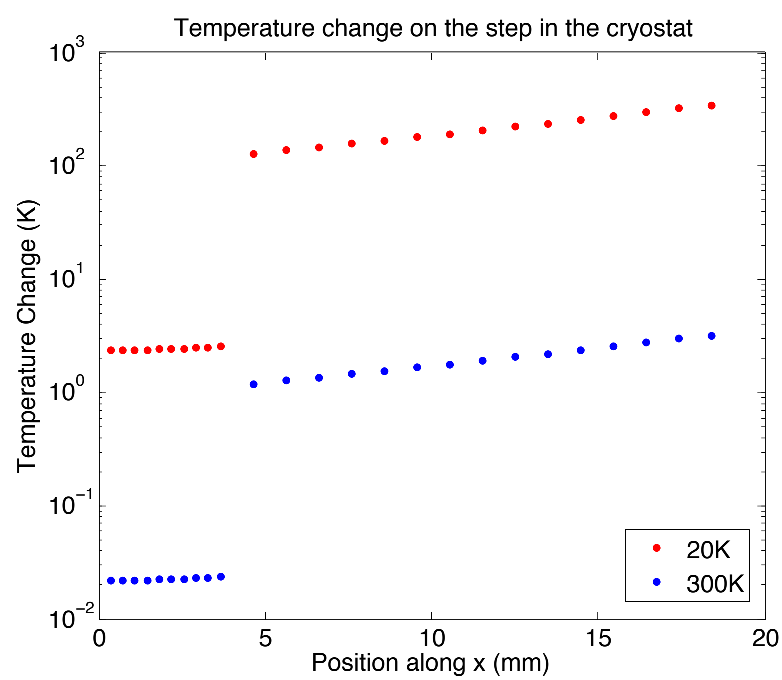

(b) Temperature Change

Fig. 7.3. Plots of the peak power density and initial rate of temperature change on the step in the SCU cryostat. The integrated temperature will give the actual temperature rise (not shown).

simulations estimate a slightly higher heat load between 0.3 mrad and 0.35 mrad, but the total heat loads are less than 10% apart.

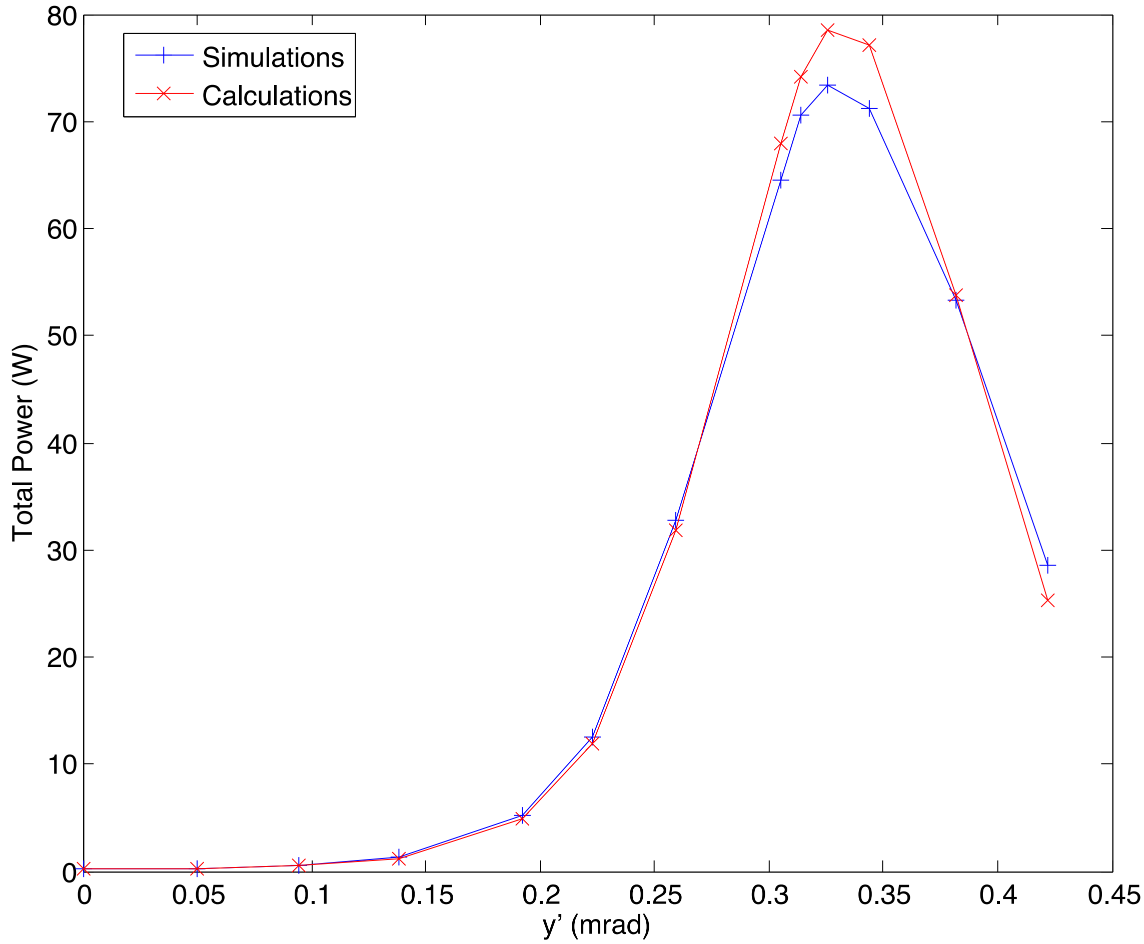

Fig. 7.4. Comparison of two radiation heat load models, from an electron beam with a vertical angle through the upstream dipole magnet. The simulations were done with Synrad3D, and the calculations were done using the analytical model described in chapter 6.

7.3.2 Vertical offset

A similar set of simulations was run to study the radiation heating as a function of vertical offset through the bending magnet. Results from this comparison is shown in Figure 7.5. Included in these results is the x-y coupling of the beam position.

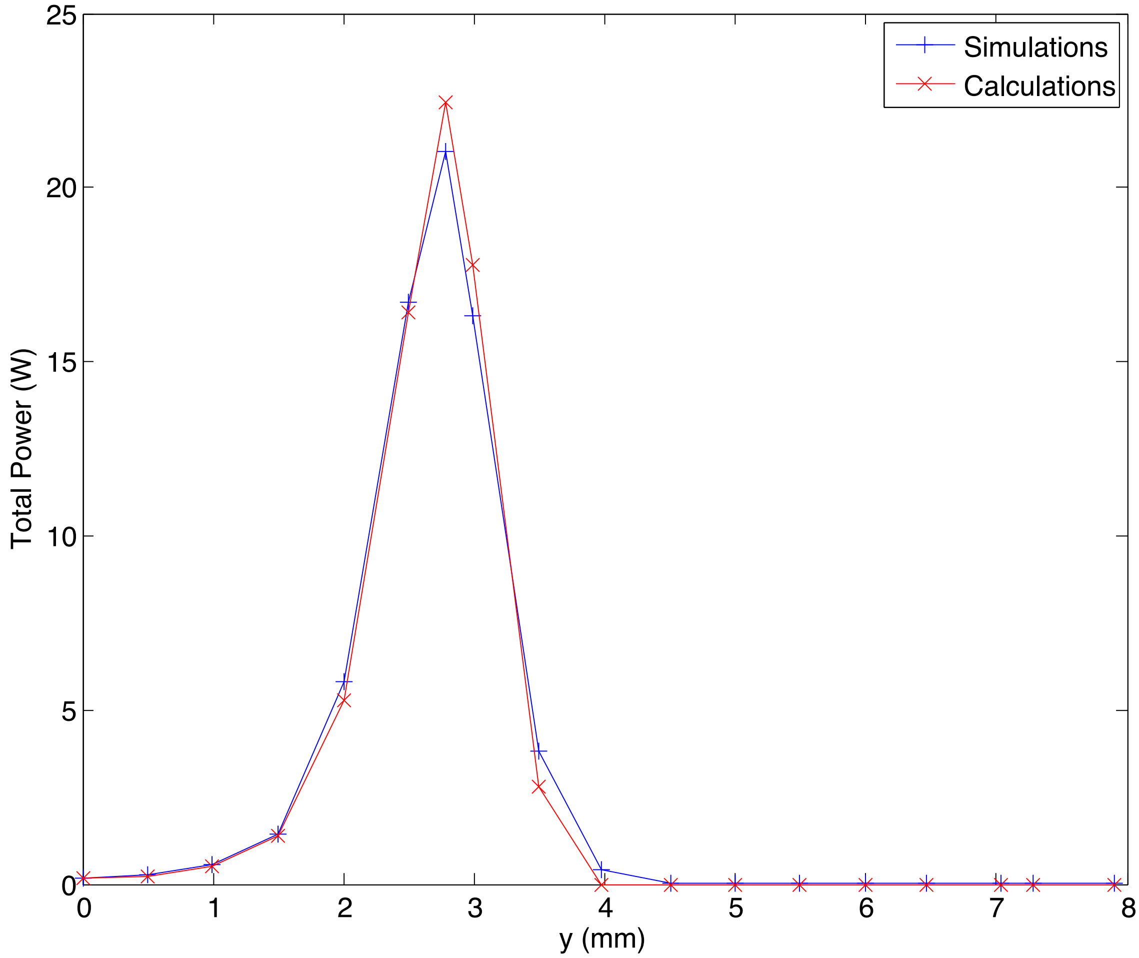

Fig. 7.5. Comparison of two radiation heat load models, from an electron beam with a vertical offset through the upstream dipole magnet. The simulations were done with Synrad3D, and the calculations were done using the analytical model described in chapter 6.

Once again there is a good agreement between the Synrad3D results and the analytical model. Based on these results we assume the full radiation heating map in Figure 6.5 is an accurate model of radiation heating when no scattering is assumed.

7.4 Benchmarking Diffuse Scattering

The photon scattering model has been updated over the years to better model a realistic photon scattering distribution. Before the diffuse scattering model was included in Synrad3D, simulation results were used to model electron cloud growth in ECLOUD. These models were compared to measurements of electron cloud growth in the Cornell Electron Storage Ring Test Accelerator (CesrTA). This study investigates the dependence of electron cloud buildup on the azimuthal position of photoelectron production on the vacuum chamber wall.

CesrTA is an electron/positron storage ring light source at Cornell University. It is also used as a test accelerator for the ILC damping ring design; accelerator parameters are shown in Table 7.3.

Table 7.3
Parameters of the CESR Damping Ring Test Accelerator (CesrTA)

Parameter	**Value**
Circumference	768 m
Beam energy	Variable from 2.1 GeV to 5.3 GeV
Revolution period	2.56 μs

Results showed that the specular scattering model was incomplete and diffuse scattering was needed to account for the electron cloud growth measured. This section will compare simulation results to measured electron cloud growth and discuss the results. The end of the section will present a basic diffuse scattering model.

7.4.1 Method

This work utilizes two simulation codes Synrad3D [30] and ECLOUD [48] to model the results from shielded pick-ups (SPU) [49, 50] a free electron detector placed in a drift section of the CesrTA ring. Comparing the simulation to data will allow us to study the effects of the beam chamber design on the photon distribution around the perimeter of the chamber, and how that changes the photoelectron signal in the SPU. Synrad3D was used to simulate the photon scattering and absorption assuming two different chamber wall shapes. The flux of photons around the perimeter of the ring is input into ECLOUD [48] to simulate the dynamics of the electron cloud buildup. The primary and secondary photons are assumed to produce photoelectrons with a quantum efficiency of 30%.

Time resolved SPU studies at CesrTA use witness bunches to measure electron cloud dynamics. Witness bunch measurements use two positron bunches, the first starts the EC growth and the second excites the bunch to be measured by the SPU. Using different bunch spacings the dynamics of the cloud can be studied. The SPU data shown in Figure 7.7 and Figure 7.10 use this measurement technique. Measurement focused on radiation distribution and electron cloud growth from a 5.3 GeV positron beam.

7.4.2 Smooth Wall Results

Initially Synrad3D simulations were done using a simplistic wall file approximating the CesrTA chamber wall as an ellipse with major and minor axes of 45 mm and 25 mm, respectively. The photon flux around the perimeter of the chamber as a function of angle, ϕ is shown in Figure 7.8. The bottom of the chamber is defined by the angles π to 2π. From Figure 7.6, a photon flux of 0.02 photons/m/beam particle/radian was absorbed on the bottom of the chamber surface.

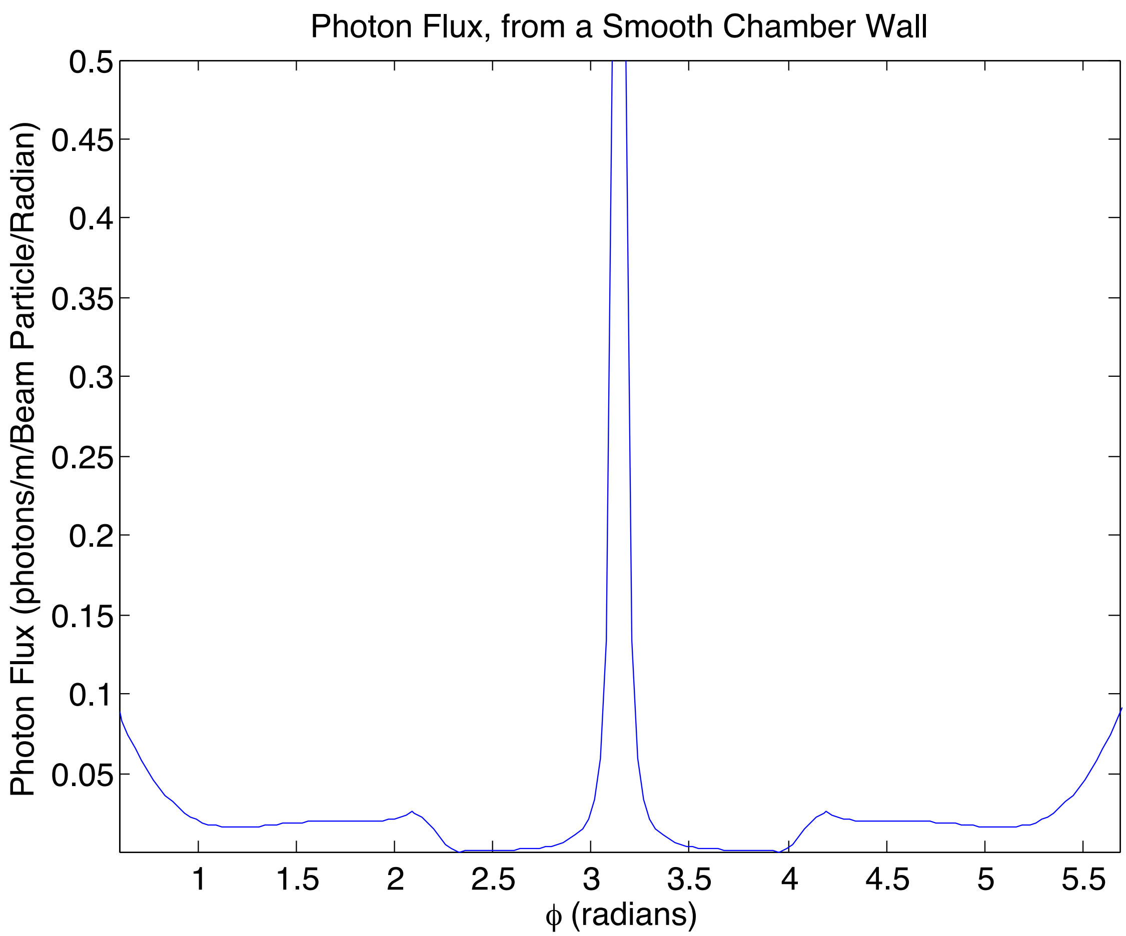

Fig. 7.6. Photon flux around the perimeter of the chamber walls, assuming a simple ellipse as the chamber shape.

Figure 7.7 compares the simulation results with the measurement. When the wall is assumed to be a simple ellipse the measurements agree with the simulation results from Synrad3D and ECLOUD.

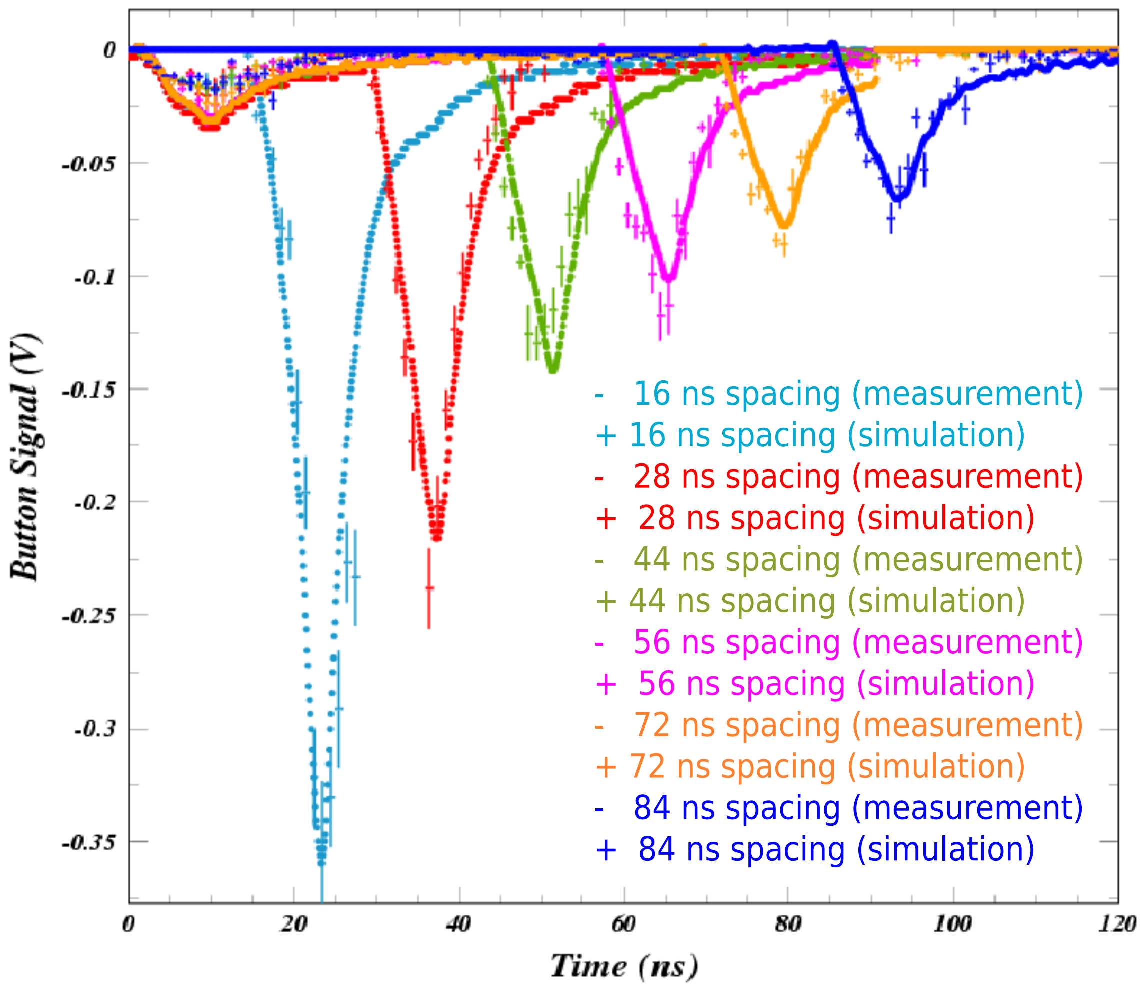

Fig. 7.7. Shielded pickup measurements compared to Synrad3D and ECLOUD simulation results, for different spacings of the leading and witness bunches in the accelerator. Simulations assumed the vacuum chamber is an ellipse [51].

7.4.3 Realistic Wall Results

The simulations were repeated with a more realistic CesrTA chamber. This chamber is similar to an ellipse on the top and bottom of the chamber, but the sides are flat, Figure 7.8.

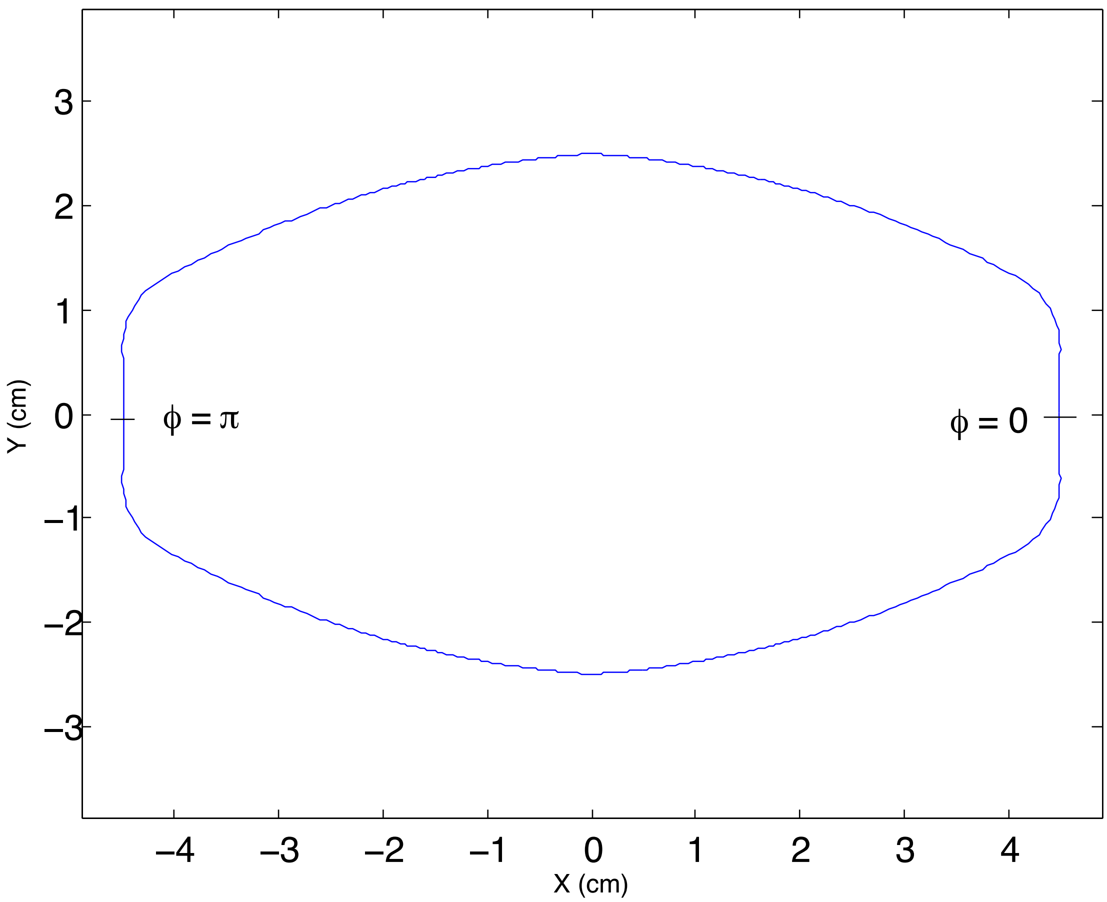

Fig. 7.8. X-Y cross section of the realistic wall at the SPU. The angles presented are the normalized angles in Figure 7.6 and Figure 7.9.

The flux on the bottom of the chamber is reduced by 70% to 0.006 photons/m/beam particle/radian, as compared to the elliptical chamber because of the flat sides, see Figure 7.9.

Simulations done with ECLOUD show no photoelectron signal at 14 ns in the detector from this low photon flux. The decrease in photon flux is due to the shape of the vacuum chamber. The elliptical shape in the smooth wall allows the photons to reflect with a greater vertical angle when scattering near the y-axis. In the realistic chamber these photons are reflecting off a flat surface and not gaining that same

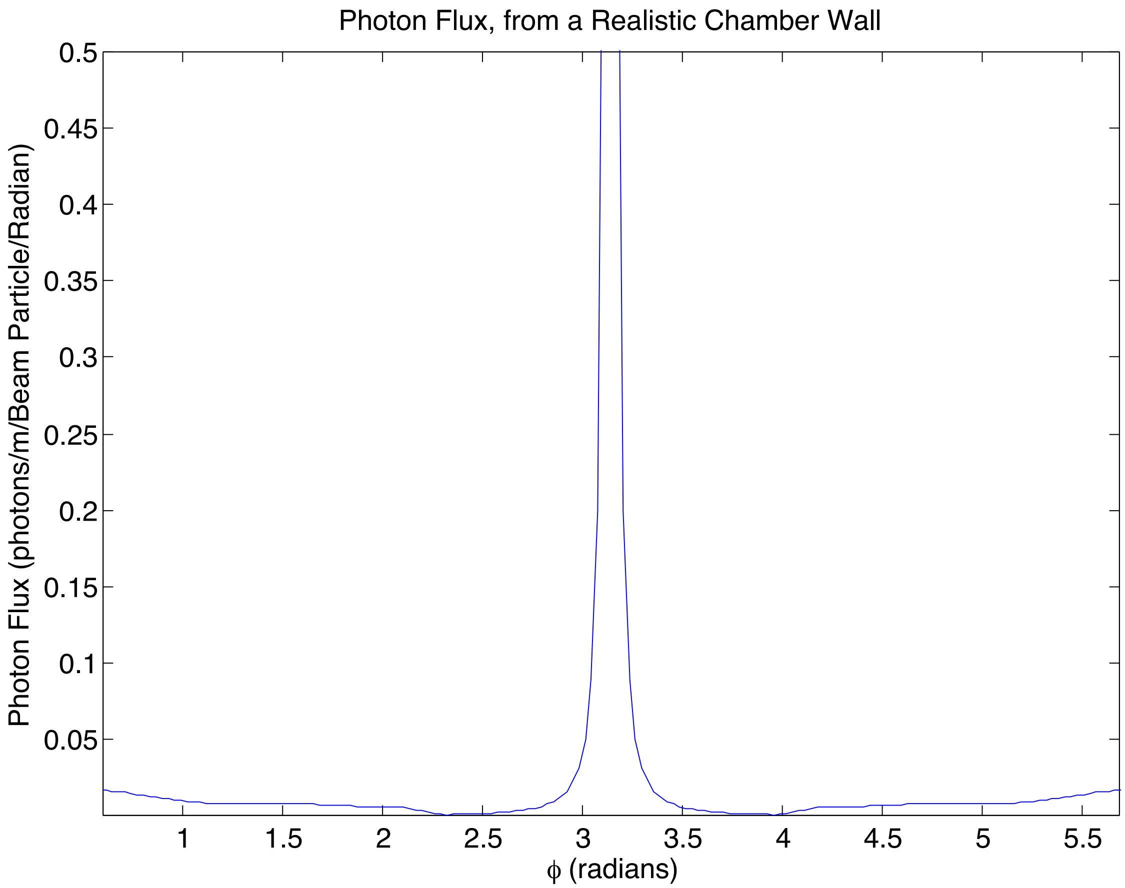

Fig. 7.9. Photon flux around the perimeter of the chamber walls, assuming a realistic chamber shape.

vertical scattering angle needed for them to be absorbed on the top or bottom of the chamber wall, Figure 7.11. The photoelectron signal in the SPU is created by a process not currently being simulated.

7.4.4 First Diffuse Scattering Model

To determine if a diffuse scattering model will produce a photon distribution similar to that of the smooth chamber wall; a simple diffuse model was created using the CesrTA lattice. A rectangular chamber was modeled in Synrad3D. The rectangle has

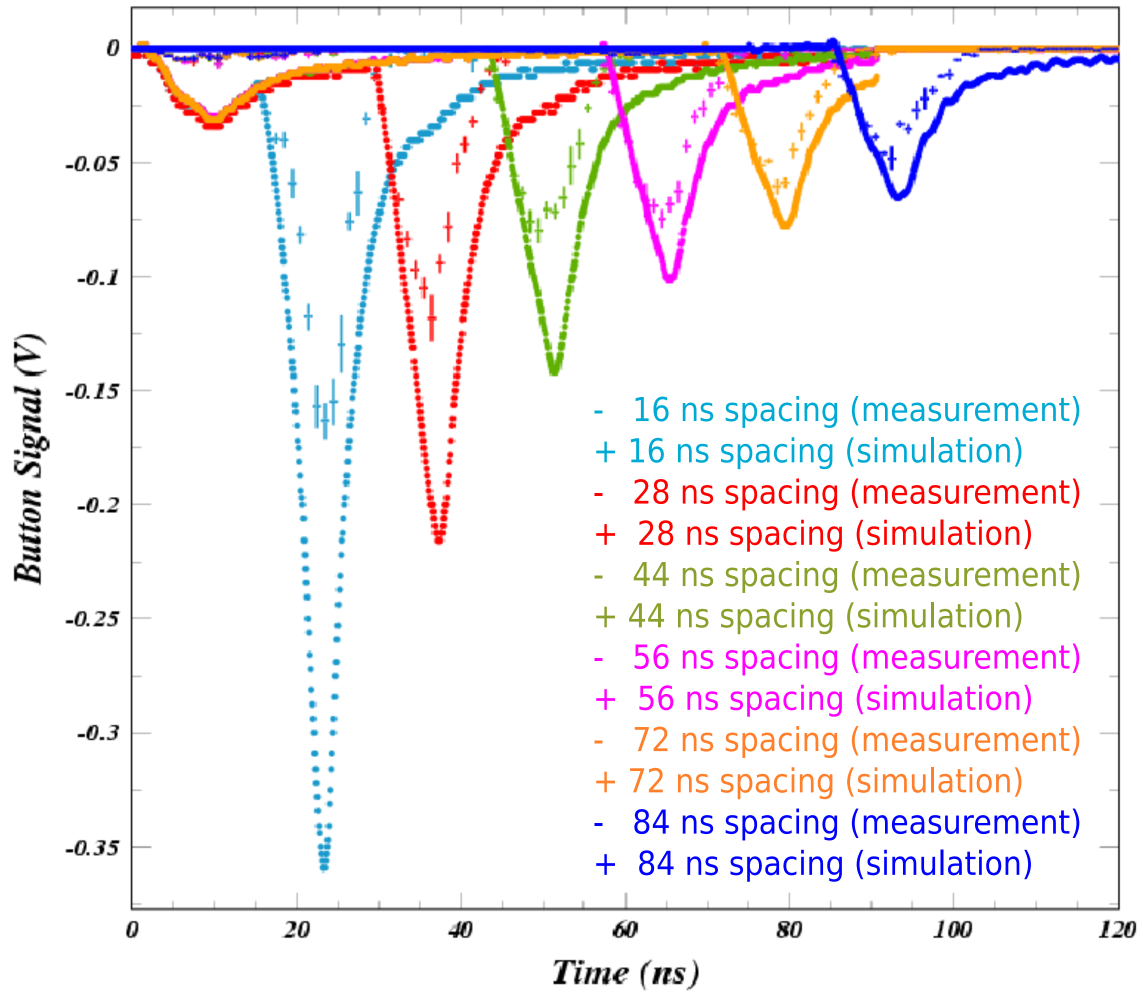

Fig. 7.10. Shielded pickup measurements compared to Synrad3D and ECLOUD simulation results, for different spacings of the leading and witness bunches in the accelerator. Simulations assumed the vacuum chamber has a realistic shape [51].

the same major and minor axes as the CesrTA ellipse, 45 mm and 25 mm respectively. The grazing angles of the photons in CesrTA are all smaller than 5°, so it was assumed that all photons had a scattering angle of ±1° from the incident angle. Assuming the photon is absorbed longitudinally in the same location, a new x,y, absorption point was calculated for each photon. The results, Figure 7.12, show that without diffuse scattering there is no photon flux on the top or bottom of the chamber. The simple

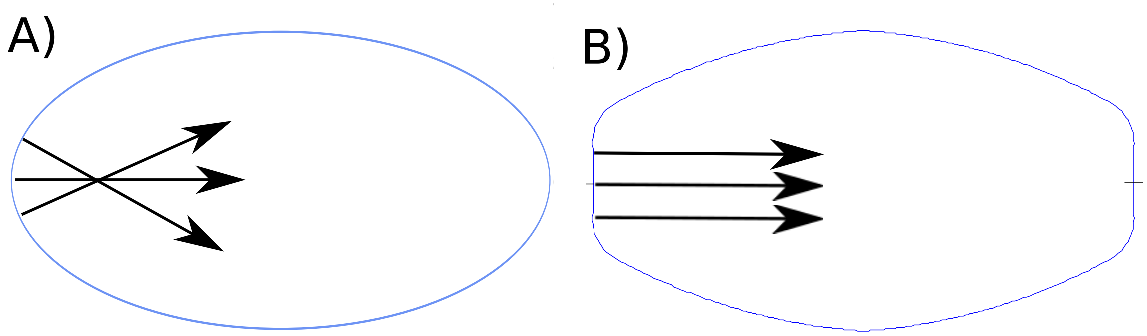

Fig. 7.11. Photons reflected off the smooth wall chamber are absorbed on the top and bottom of the chamber, due to the vertical scattering angle from the rounded chamber walls, A). Photons reflected off the realistic chamber wall, B) do not scatter vertically, reducing the probability that they will be absorbed on the top or bottom of the chamber.

diffuse scatter model increases the photon flux on the top and bottom of the chamber to 0.08 photons/m/beam particle/radian. The rectangular chamber wall will underestimate the photon flux on the top and bottom of the chamber compared to a more round chamber.

Based on this work, and the surface roughness measurements discussed in subsection 4.2.2 a full diffuse scattering model was implemented into Synrad3D by Gerry Dugan and David Sagan of Cornell University.

7.5 Photon Scattering

We have now shown the importance of including the diffuse model to get an accurate photon distribution. This section will describe the effect of diffuse and specular scattering on the radiation heating of the SCU chamber. Comparing 5 different scattering models we determined that the analytical model is a conservative estimate of radiation heating. The specular scattering model assumed a surface roughness of

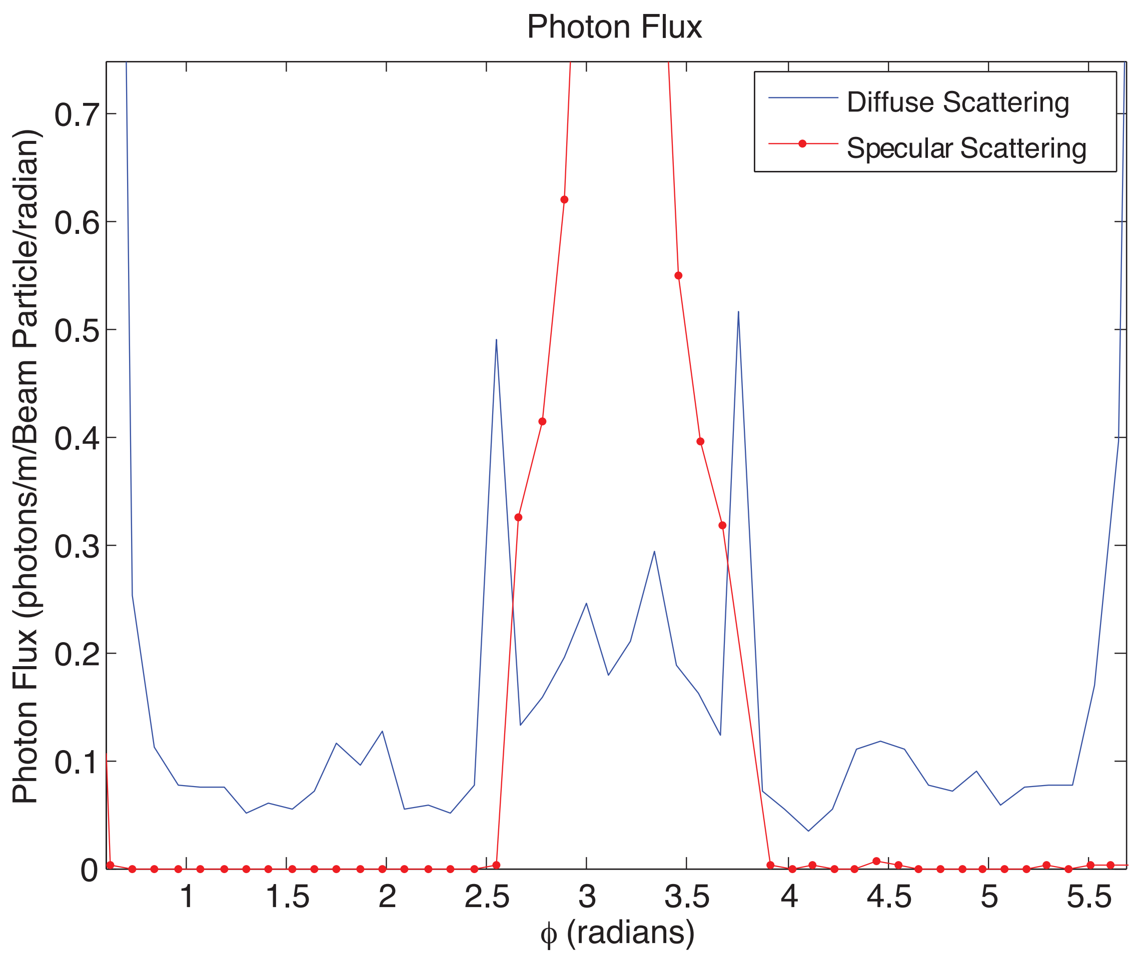

Fig. 7.12. Photon flux around the perimeter of the chamber walls, comparing elastic scatter to diffuse scatters with a rectangular chamber wall.

10 nm [34], while the diffuse scattering model is dependent on the user defined surface parameters.

The total heat load values from scattering simulations are shown in Table 7.4. The heat loads include radiation from all radiation sources in the upstream sector, including the two main dipole magnets and the mini-bends.

The no scattering and specular scattering simulations used the default chamber surface parameters described in section 4.2. Each of the the three diffuse scattering models assumes different surface parameters. All Rough simulated photon scattering

Table 7.4
Radiation heat load values for 5 scattering models using Synrad3D.

Scattering model	**Surface Parameters**	**Heat Load**
No scattering		0.199 W
Specular Scattering		1.52 W
Diffuse Scattering	All Rough	0.14 W
	All Smooth	0.061 W
	Combination	0.009 W

assumes the full accelerator vacuum chamber wall was the roughness of the as-received extruded aluminum chamber (1180 nm rms and 3.8 μm correlation length). The all smooth model simulated the full chamber wall with the roughness of the polished aluminum chamber (139 nm rms and 2.4 μm correlation length). The combination model is closest to the installed chamber with the smoothed aluminum chamber through the SCU length and the as-received aluminum chamber for the rest of the accelerator simulated. The simulations were done using layout 4 described in subsection A.2.4,

When specular scattering is assumed the heat load is 10 times greater than the heat load for any other scattering model. This can be understood in Figure 7.13 where the high energy photon flux is greatest for the specular scattering model and power is proportional to energy.

The photon flux for the no scattering and rough surface are equal for photon energies above 350 eV, which is why the heat load for the two different scattering models are so similar. The small difference is because of the difference in photon flux for photon energies below 350 eV. The no scattering model increases at lower energies, while the rough scattering model decreases for low photon energies, making the calculated heat load greater for the no scattering model.

The difference in heat load simulated is based on the surface modeled in the simulation. There are two scattering processes that determine the radiation heat

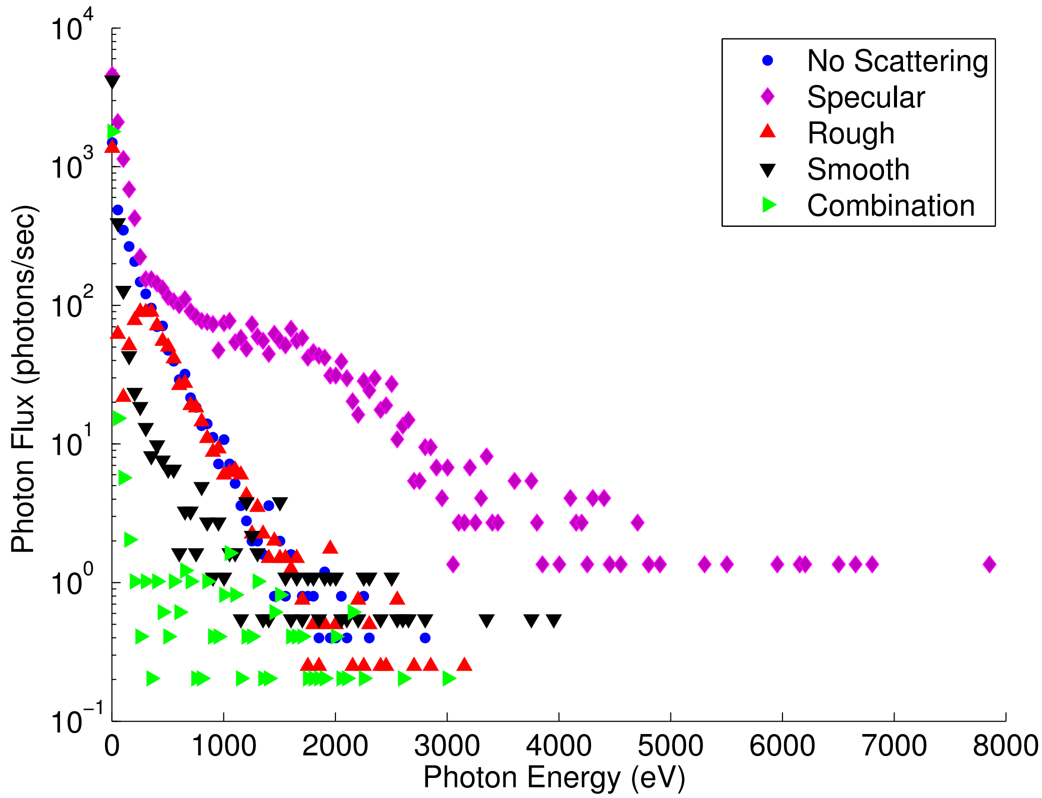

Fig. 7.13. Photon flux of photons absorbed on the SCU chamber assuming 5 different scattering models.

load on the SCU when scattering is included, 1) photons can scatter into the SCU chamber, and 2) photons can scatter out of the SCU chamber. The ratio of how many scatter in and how many scatter out explain the difference in heat loads. The number of reflections each macro-photon had before it was absorbed in the SCU is shown in Figure 7.14.

Since photon reflectivity decreases for high energy photons on average the lower the photon energy the more times it scatters. The simulations with a high number of reflections show a small heat load. For example, the 'combination' simulation had the lowest heat load, and the number of reflections peaks at 10 reflections per photon, the highest number in all the simulations.

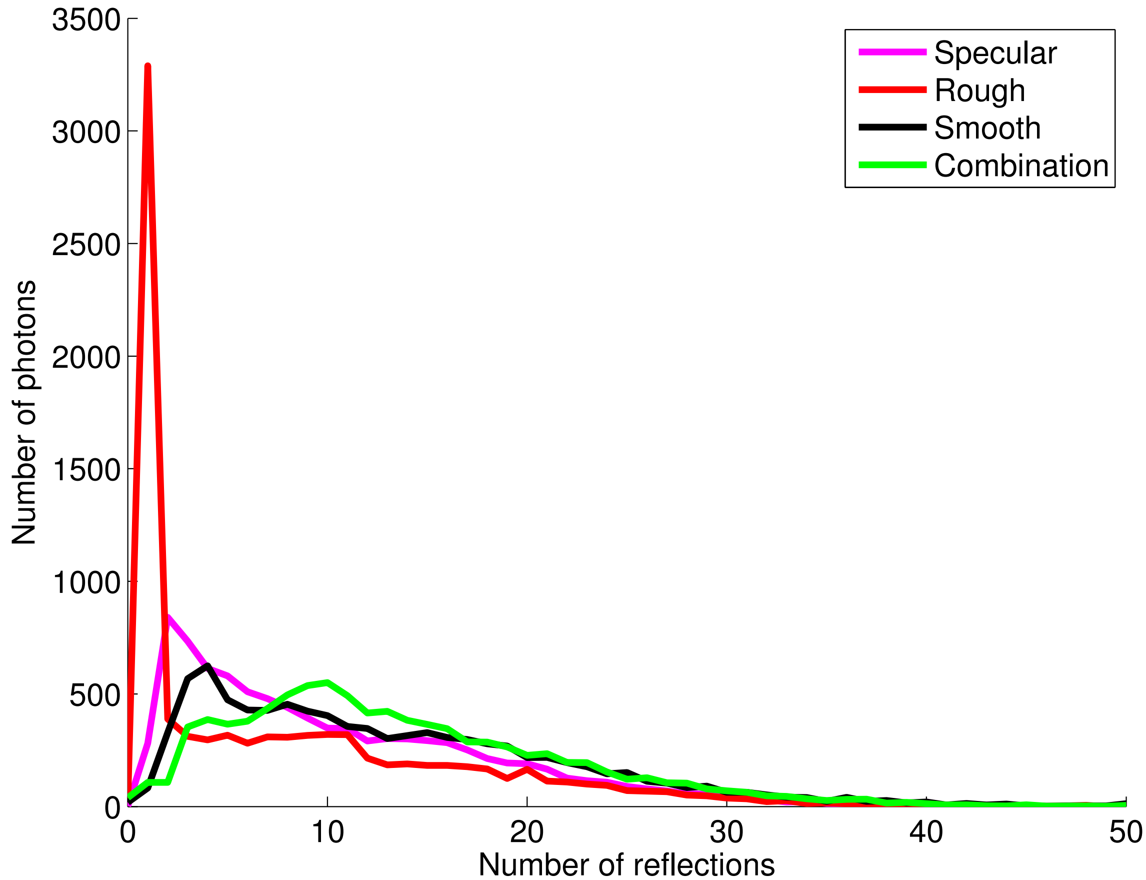

Fig. 7.14. Number of reflections per macro-photon, comparing the results from four scattering models.

Based on these results the no scattering or analytical model is a conservative calculation of the radiation heat load on the SCU chamber.

7.6 Summary

In this chapter we have shown that the no scattering model had good agreement with the analytical model developed in chapter 6, for an ideal electron beam orbit and when the orbit has a vertical offset or angle in the upstream dipole magnet. Synrad3D was also used to show the importance of including diffuse scattering in the simulation to create a realistic photon distribution azimuthally around the chamber, by comparing simulation results to electron cloud growth in the CesrTA ring. Finally, Synrad3D was used to calculate the radiation heat load assuming various scattering models and parameters for the APS SCU. The realistic chamber model had the lowest estimated heat load, showing that the no scattering model is a conservative estimate of the radiation heating because it assumes that all photons are absorbed the first time they hit the chamber wall.

8. MEASUREMENT OF TEMPERATURE RISE IN SCU

The temperature rise in the SCU chamber was measured for known steerings of the electron beam in the upstream dipole magnet. This chapter will describe the method used to measure the the temperature rise, and the analysis of the data, then show a comparison of the data with calculated temperature rise.

8.1 Measurement Method

This section will describe the method used to measure the temperature rise in the SCU beam chamber. During the measurements the SCU coil current was set to 0 A or no magnetic field. Turning the coil current off protects the device from quenching and reduces heat load from the coils. This is a requirement to allow for large steerings without tripping the beam position limiting detectors (BPLD) which will dump the beam in order to protect the machine.

8.1.1 Accelerator Setup

Three hundred and twenty-four evenly spaced bunches were injected into the machine and run in top up. Of the three standard fill patterns 324 bunches provides the lowest resistive wall heating due to image currents flowing in the walls. Top-up mode will inject more current into the machine every two minutes, it 'tops-up' the current. By running in top-up the electron beam current stays constant, reducing error from a changing beam current. The total beam current was varied between 10, 20 and 100 mA to keep the total heat load on the SCU chamber below 10 W as calculated analytically, and shown in Figure 6.5.

8.1.2 Thermal sensor location

The temperature sensors installed in the SCU are Cernox^{TM} Negative temperature coefficient (NTC) Resistance temperature detector. The resistance of the sensor is dependent on its temperature. Nine zirconium oxy-nitride semi-conductor resistors from Lake Shore Cryotronics, Inc. [52] were installed along the length of the beam chamber. These temperature sensors are resistant to magnetic field-induced errors and ionizing radiation. The location of the nine thermal sensors inside the cryostat is shown in Figure 8.1.

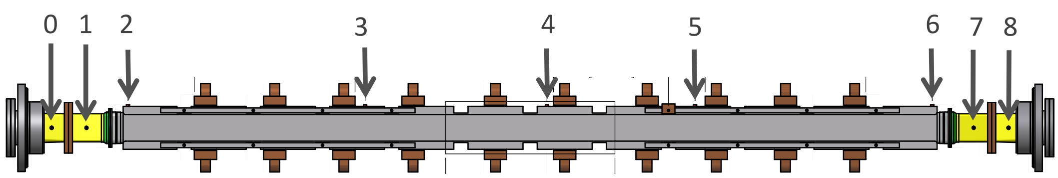

Fig. 8.1. Location of the nine thermal sensors along the length of the chamber in the SCU cryostat. The chamber is 2 m long.

For the comparison to the analytical model only sensors 3, 4, and 5 were used because they are between thermal links to the copper bus bar that is cooled by two cryocoolers. These sensors are not located along a temperature gradient like the other installed sensors are, and we were able to calibrate the temperature rise to a known power on the chamber wall.

8.1.3 Beam steering

Standard orbit control was used to steer the electron beam for studies. Orbit control minimizes the errors on the beam position monitors (BPM). Each BPM has 4 parameters; setpoint, offset, adjusted value and error. The setpoint is the user defined position where they want the beam to be at that location. The offset is the difference between the BPM's electrical center and the magnetic center of the adjacent magnets.

The adjusted value defined as the raw position plus the offset. The offset values are measured and updated for all BPM's in the ring yearly. The error is the difference between the setpoint and adjusted electron beam position.

The center of the SCU defined during commissioning as the position with the minimum temperature when running with 24 bunches [53]. The trajectory of the beam through the SCU was set to this defined center, to minimize the resistive wall heat load. To create a known vertical angle or offset through the bending magnet the setpoint of the BPM's before and after the main bending magnet were changed and orbit correction was used to steer the beam. After the beam trajectory had settled we waited for the chamber temperatures to reach an equilibrium temperature, typically 5-10 min,

8.2 Data Analysis

To compare the measurements with the model a calibration between power incident on the SCU chamber and the temperature rise had to be created. The calibration model and comparison of results with the model will be discussed in this section

8.2.1 Absolute Beam position

The electron beam orbit through the dipole magnet was calculated using the adjusted BPM value, to include any errors in the beam position. The on-axis orbit was defined as the position of the electron beam during user operation.

The angle is defined as the angle between the electron beam position at the two BPM's assuming the they are 3.333 m apart. Next the electron beam offset was calculated at the end of the dipole magnet, instead of the BPM. The offset is defined by

$$y = y_2 + y' * s \tag{8.1}$$

where y is the beam offset through the dipole magnet, y_2 is the adjusted position of the beam at the downstream BPM, y' is the angle of the electron beam through the dipole and s is 15.6 cm, the distance between the BPM and end of the dipole magnet.

8.2.2 Reducing raw data

To calculate the equilibrium temperature the temperature rise at each steering position was fit to an exponential decay,

$$T = T_0(1 - e^{-bt}) \tag{8.2}$$

where T_0 is the equilibrium temperature. This was done for each thermal sensor at every steering position. Figure 8.2 shows the measured temperature rise for the measurements taken with 10 mA of beam current.

8.2.3 Calibration

This section will describe the how the expected heat loads were calculated and converted to a temperature rise in the SCU.

Resistive Wall Heat Load

Although the 324 bunch pattern was used to reduce the image current heating, there was still a small amount of heating that needs to be taken into account. The resistive wall heating is dependent on the frequency spectrum of the bunch as it travels through the SCU chamber, for 324 bunches that is described by [54, 55],

$$I_b(\omega) = I_{av}\frac{\omega_0}{2\pi}\exp\left[-\frac{(\omega\sigma_t)^2}{2}\right]\sum_{n=-\infty}^{\infty}\delta(\omega - nM\omega_0) \tag{8.3}$$

where the variables and their values are listed in Table 8.1. For frequencies greater than 8 GHz the skin depth of the chamber wall is shorter than the mean free path of electrons in the cold aluminum, and the anomalous skin effect must be considered.

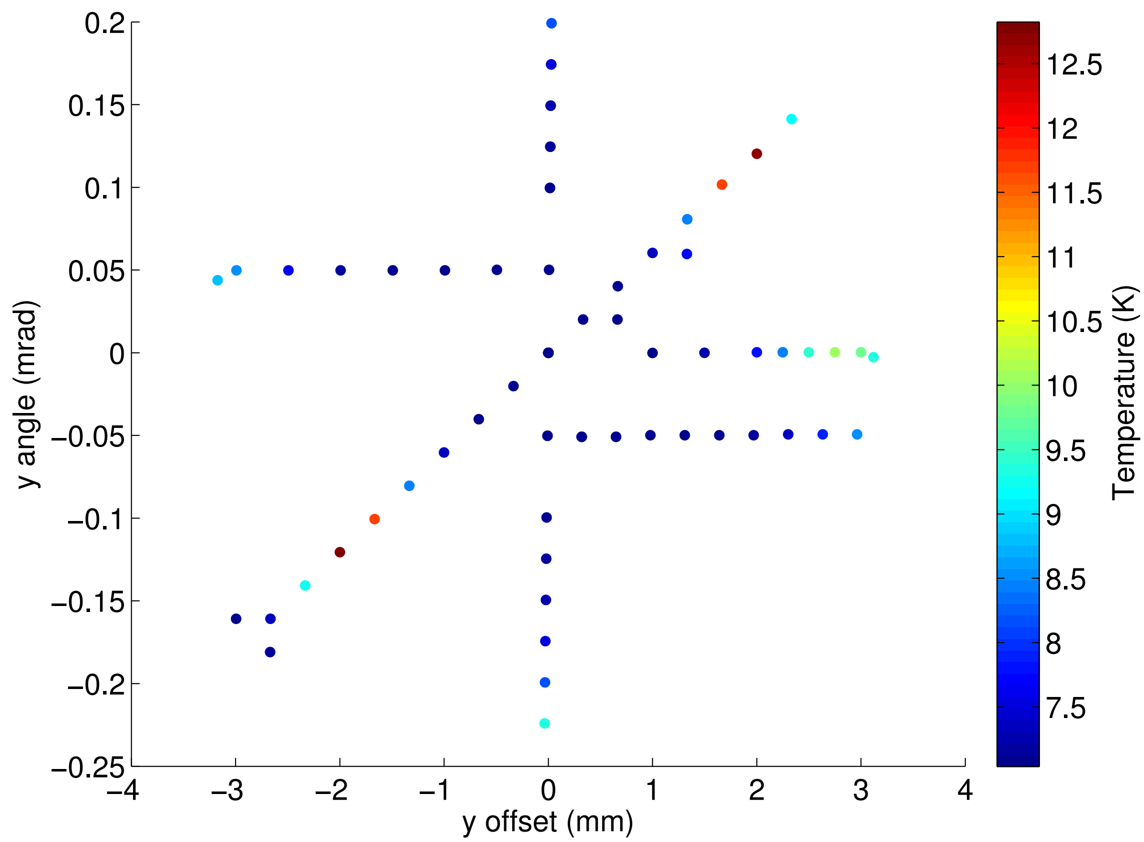

Fig. 8.2. Results of the temperature measurement using 10 mA of beam current, for temperature sensor 4.

The equations for the skin depth, λ, and mean free path, δ_s, for electrons in aluminum is given by Equation 8.5 and Equation 8.4. The frequency spectrum of 324 bunches is shown in Figure 8.3, the calculation for resistive wall heating for frequencies above and below 8 GHz will be calculated separately.

$$\lambda = [6.6 * 10^{-16}(\Omega m)]/\rho \tag{8.4}$$

$$\delta_s = \sqrt{\frac{2\rho}{\omega\mu_0}} \tag{8.5}$$

To calculate the power per meter, P, from the frequency spectrum use

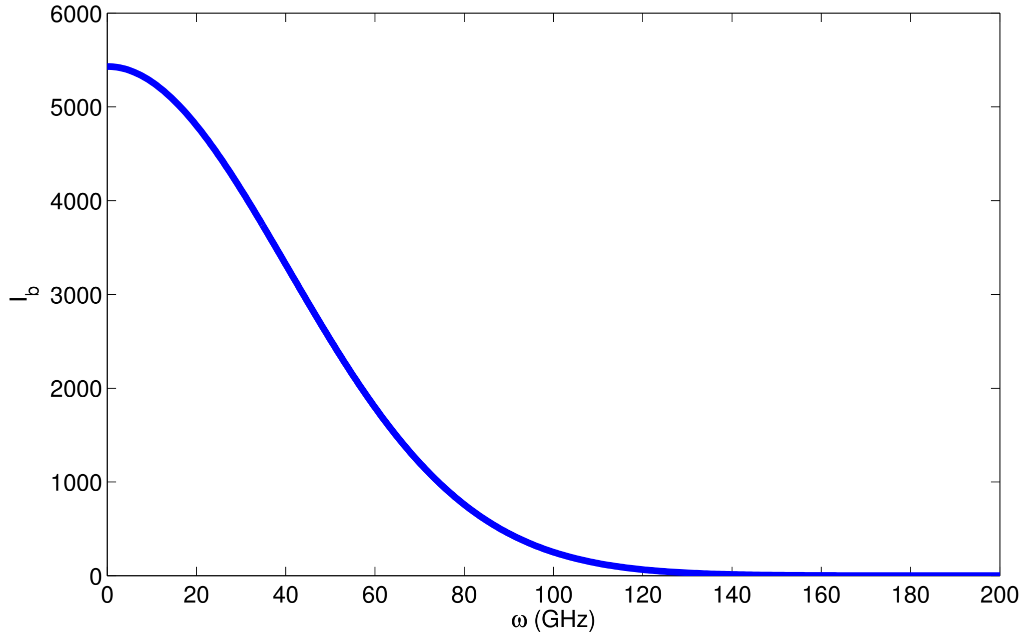

Fig. 8.3. Fourier transform of the longitudinal current distribution for 324 evenly spaced bunches, as given by Equation 8.3. Assuming 100 mA total beam current.

$$\frac{P}{L} = 2I_{av}^2 \frac{1}{2\pi r} \sum_{n=1}^{N_{max}} R(nM\omega_0) \exp[-(nM\omega_0\sigma_t)^2] \tag{8.6}$$

where R is the surface resistance of the beam chamber. For frequencies below the anomalous skin effect cutoff R is defined by, R_s,

$$R_s = \sqrt{\frac{\omega\mu_0\rho}{2}}. \tag{8.7}$$

Above the cutoff frequency R is defined by R_{as} which is the surface resistance under the anomalous skin effect, given by

$$R_{as}(\omega) = R_\infty(1 + 1.157\alpha^{-0.276}) \tag{8.8}$$

R_∞ is the surface resistance under the extreme anomalous region, $\alpha \gg 1$, see Equation 8.9. While α is defined by Equation 8.10.

$$R_\infty = \left(\frac{\sqrt{3}}{16\pi} \rho\ell (\omega\mu_0)^2 \right)^{\frac{1}{3}} \tag{8.9}$$

$$\alpha = \frac{3}{4}\omega\mu_0 (\rho\ell)^2 \rho^{-3} \tag{8.10}$$

$$\rho\ell = 6.6 * 10^{-16} \tag{8.11}$$

Variables and their values are listed in Table 8.1.

Table 8.1
Parameters and their values for the resistive wall heating calculation.

Variable	**Meaning**	**Value**
I_{av}	Total beam current	10, 20 or 100 mA
ω_0	Revolution frequency	1.706 MHz
σ_t	Bunch length	24.8 ps
M	Number of bunches	324
ρ	metal resistivity for 6063-T5 Al at 20K	$2.8 * 10^{-9}$ Ω−m
μ_0	Permeability of free space	$4\pi 10^{-7} (V * s)/(A * m)$

The contribution from the normal skin effect and anomalous skin effect are added to get the total power per meter. Assuming a chamber length of 1.33 m and applying these equations, we calculate the resistive wall heating for the beam currents used for the heating measurements, results are in Table 8.2.

Analytical Model

The radiation heat load was calculated analytically from the model described in chapter 6. To calculate an accurate heat load the horizontal beam position through the dipole was included in the heat load calculation. The radiation heat load was

Table 8.2
Resistive Wall heating for three beam currents.

Beam Current	Heat load
10 mA	0.0033 W
20 mA	0.013 W
100 mA	0.33 W

added to the resistive wall heat load to calculate the total estimated heat load for each electron beam steering orbit.

Power to Temperature Calibration

The calibration was completed by measuring the temperature rise when a known power is put on the chamber. A heater was placed on the chamber in the section with thermal sensor 5, and by measuring the temperature rise in TS 5, for a range of powers a calibration of power to temperature can be created. The starting temperature of TS 5 was 7 K, so that temperature was subtracted off each measured temperature to get the temperature rise. Figure 8.4 shows the measured data and the fit to the calibration equation,

$$dT = 1.974P - 0.0667P^2 + 0.00119P^3. \tag{8.12}$$

where dT is the change in temperature, and P is the power put on the chamber heater.

Results of the calculated power were converted to a temperature rise using Equation 8.12. Results of the comparison are shown in the next section.

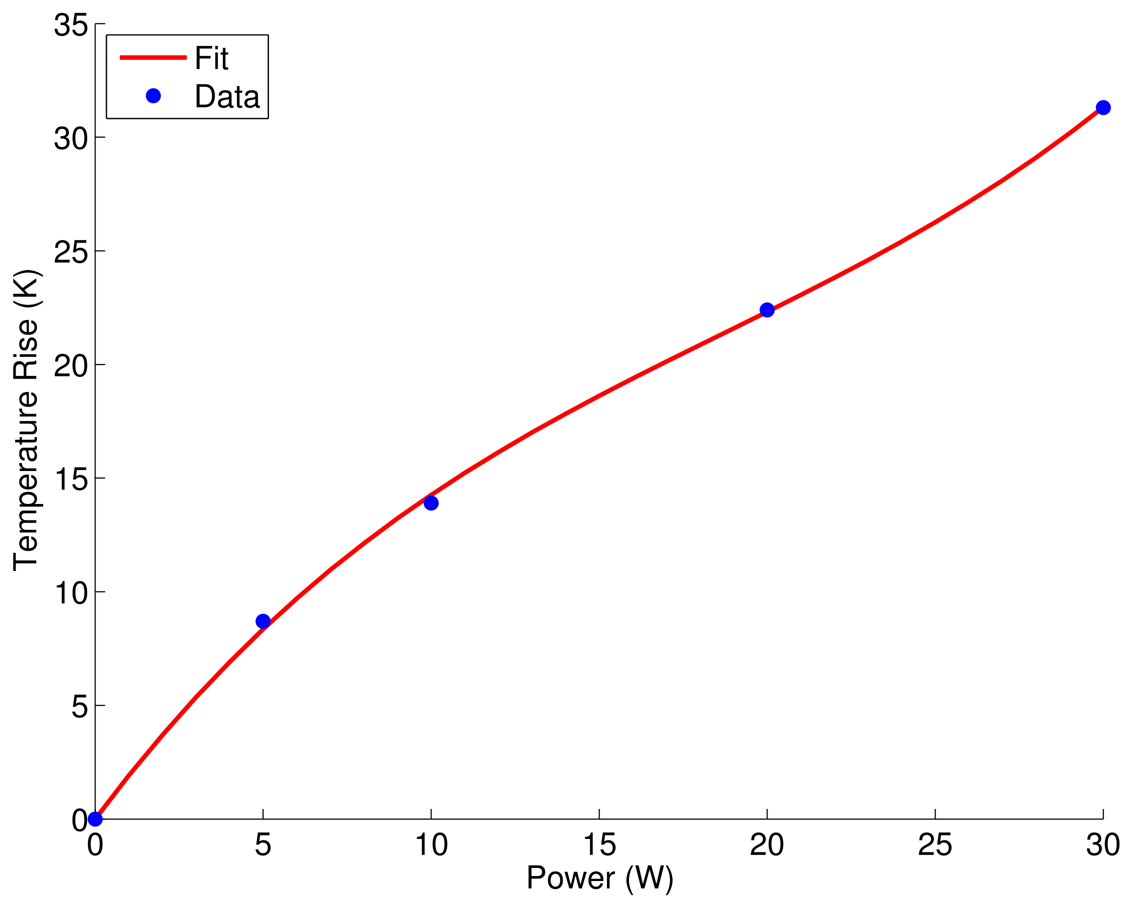

Fig. 8.4. Fit to temperature rise of calibration data, Equation 8.12.

8.3 Comparison with model

Using the calibration method described in the previous section the predicted chamber temperature was calculated. Plotted in Figures 8.5 - 8.7 is the percent error between the measured temperature and the temperature predicted by the model. Results include data from all three beam currents.

$$\text{Percent Error} = \frac{T_{model} - T_{measured}}{T_{measured}} * 100 \tag{8.13}$$

The box added to the figures shows the limits of electron beam steering when the coil current is non-zero and the BPLD's on. This is the range of steering that can occur during normal user operations. The range of steerings outside this box are only possible during machine studies, when the SCU coil current is 0 A.

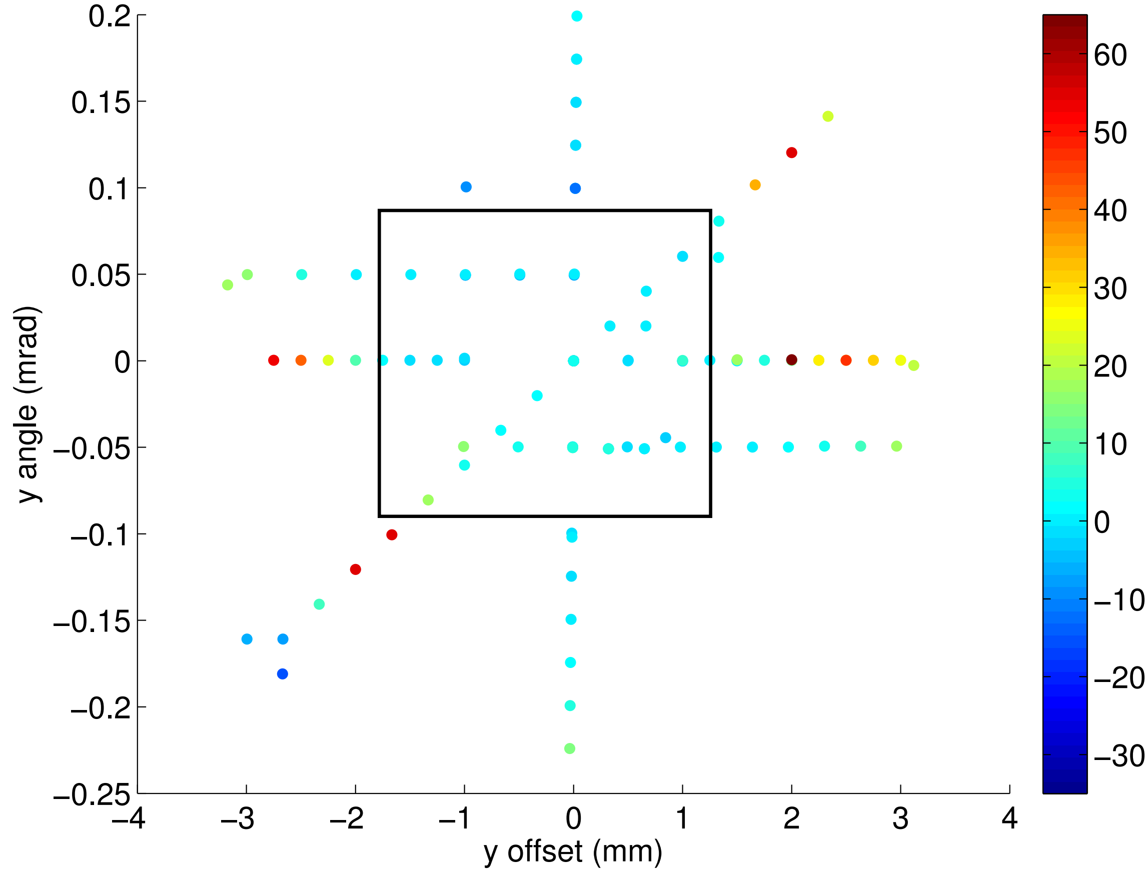

Fig. 8.5. Percent error of a comparison of measured to calculated temperatures for temperature sensor 3. Higher percent error indicates the model over estimated the radiation heat load.

Inside this range the heating model is well understood. All predicted temperatures are within 20% of the measured temperature. Previous work on heat load calculations elsewhere have not been able to explain the temperature rise of their beam liners, predictions have been off from measurements by more than 200% [21]. Previous work has largely ignored radiation heat load, or just stated it is a complex problem dependent on each individual accelerator geometry. While this is a true statement, a simple on-axis model yielded an accurate temperature rise prediction for the SCU installed at APS.

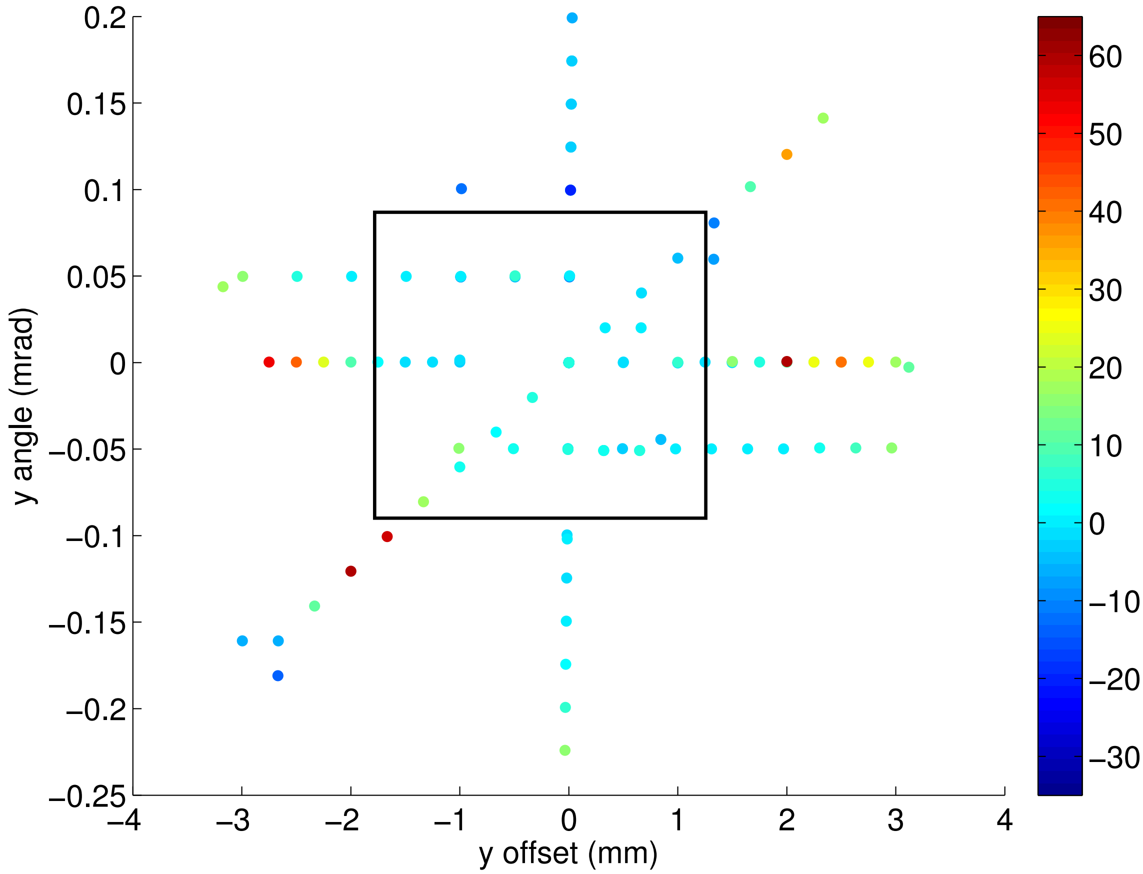

Fig. 8.6. Percent error of a comparison of measured to calculated temperatures for temperature sensor 4. Higher percent error indicates the model over estimated the radiation heat load.

For the range of steerings outside what is possible during user operation, there temperature error reaches 65%. The large error could be from the non-inclusion of photon scattering. The changes in photon distribution due to scattering from an off-axis beam was not studied.

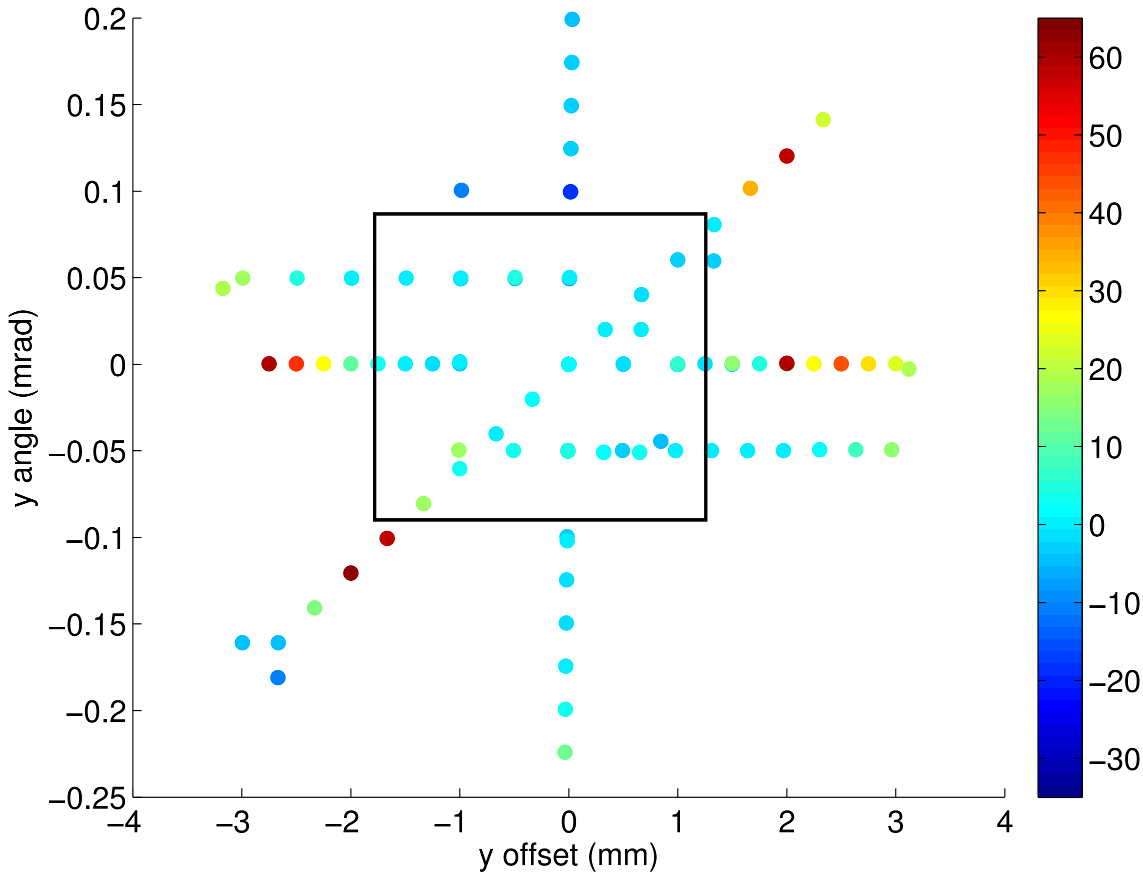

Fig. 8.7. Percent error of a comparison of measured to calculated temperatures for temperature sensor 5. Higher percent error indicates the model over estimated the radiation heat load.

8.4 Summary

This chapter outlined the measurement method, and analysis of temperature rise in the SCU beam chamber. Results show good agreement, within 20% between the predicted temperature and measured temperature for steering values within the range allowed with the device is in operation. Previously published work on heat load models have not been able to account for the heat load measured on their cold devices. But by applying a complete radiation heat load model we can show good agreement. For large steering values there is a larger error between the predicted and measured temperatures. A reason for this discrepancy could be the scattering of photons, which was not included in the model used here.

9. QUANTUM EFFICIENCY

Up until this chapter we have focused on the generation and scattering of synchrotron radiation and heating. This chapter will study the effects of the absorbed radiation. In this chapter is presented the results of a measurement of the quantum efficiency (QE) of two aluminum beam chamber samples. Results from these measurements can be used as inputs into electron cloud simulation codes. The measured QE is applicable to other synchrotron light sources with small aluminum ID chambers because the incident grazing angle distribution will be similar.

9.1 Simulations

Photoelectrons that seed the electron cloud in beam chambers are from dipole radiation generated upstream. Synrad3D was used to determine the photon energy and grazing angle range of photons absorbed on the SCU chamber, the power these photons put on the chamber wall was described in previous chapters. The Synrad3D specular scattering model was used to simulate photon scattering.

The flux of incident photons peaked at 0.6 degrees grazing angle with a maximum angle of 6 degrees, Figure 9.1. The distribution of grazing angles is based on the chamber geometry upstream of the ID. Photons that are first incident on the ID chamber have a grazing angle of 0.025 degrees. The higher angles are generated from photons that have scattered from other surfaces upstream of the undulator chamber.

As the photon energy increased the flux incident on the SCU chamber decreased, Figure 9.2. The beam chamber is shielded from on-axis dipole radiation from an upstream photon absorber [38]. Therefore the only radiation considered in this simulation is incident on the top and bottom of the chamber or has scattered from the upstream

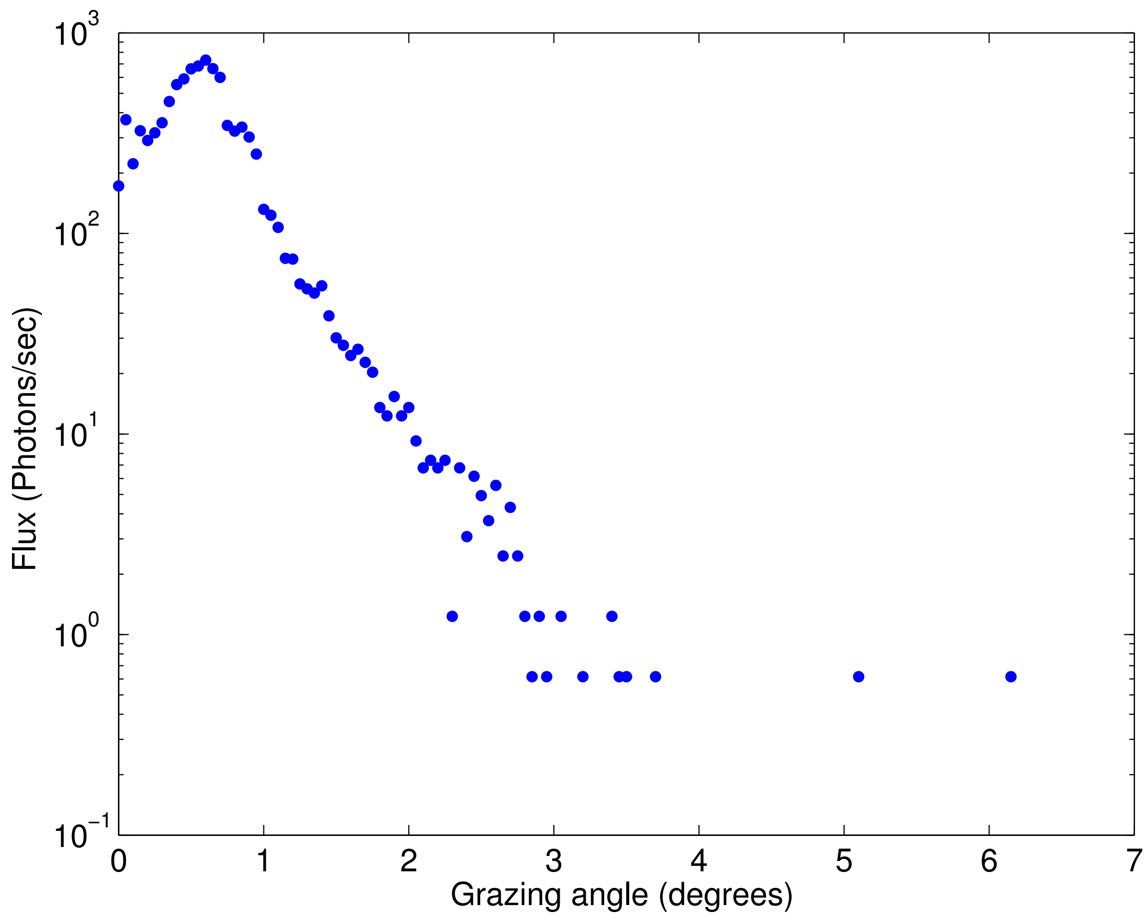

Fig. 9.1. Grazing angle of incident photons in the SCU cryostat chamber. Results produced from simulations using Synrad3D.

beam chamber wall. The probably of scattering from the chamber surface decreases as the photon energy increases.

From these simulations the range of photon energy and grazing angle capabilities of the beam line in which to do the measurement were determined. To compare the angle dependance, a beam line with varying angle capabilities was needed. To reach the lowest possible photon beam energies a soft x-ray beam line was a required.

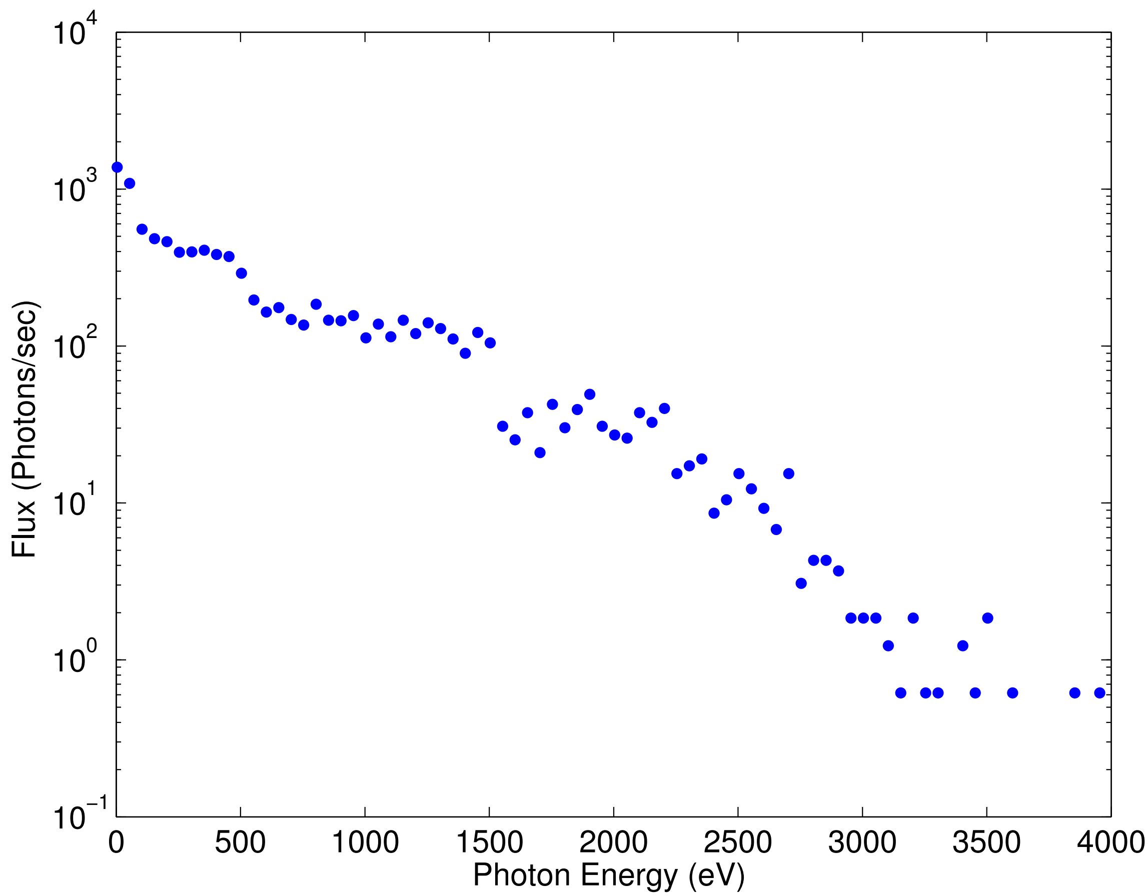

Fig. 9.2. Energy of photons incident in SCU chamber. Results produced from simulations using Synrad3D.

9.2 Measurement Description

The Australian Synchrotron's Soft X-ray beam line was used to measure the QE of beam chamber samples [56]. Two data sets were acquired. The first focused on higher energy measurement varying the incident photon energy between 100 eV and 2000 eV in 0.5 eV steps. Data were taken at grazing angles of 3, 5, 10, and 50 degrees and temperatures from 180K to 300K. The second set of data used the Australian Synchrotron running at an electron beam energy of 1.5 GeV, half its operating energy [57] to produce photons below 100 eV. Data were taken at photon energies between 35 eV and 150 eV in 1 eV steps. Data were taken at grazing angles of 3, 5, 10 and 50 degrees; all data were taken at room temperature. Due to physical limitations of the beam line the smallest grazing angle measurable was 3 degrees, and the lowest energy was 35 eV. No voltage bias was induced on the sample during the measurements. A layout of the measurement chamber in Figure 9.3 shows the relative positions of the samples and the Silicon diode used to calculate the photon flux, described in section 9.3.

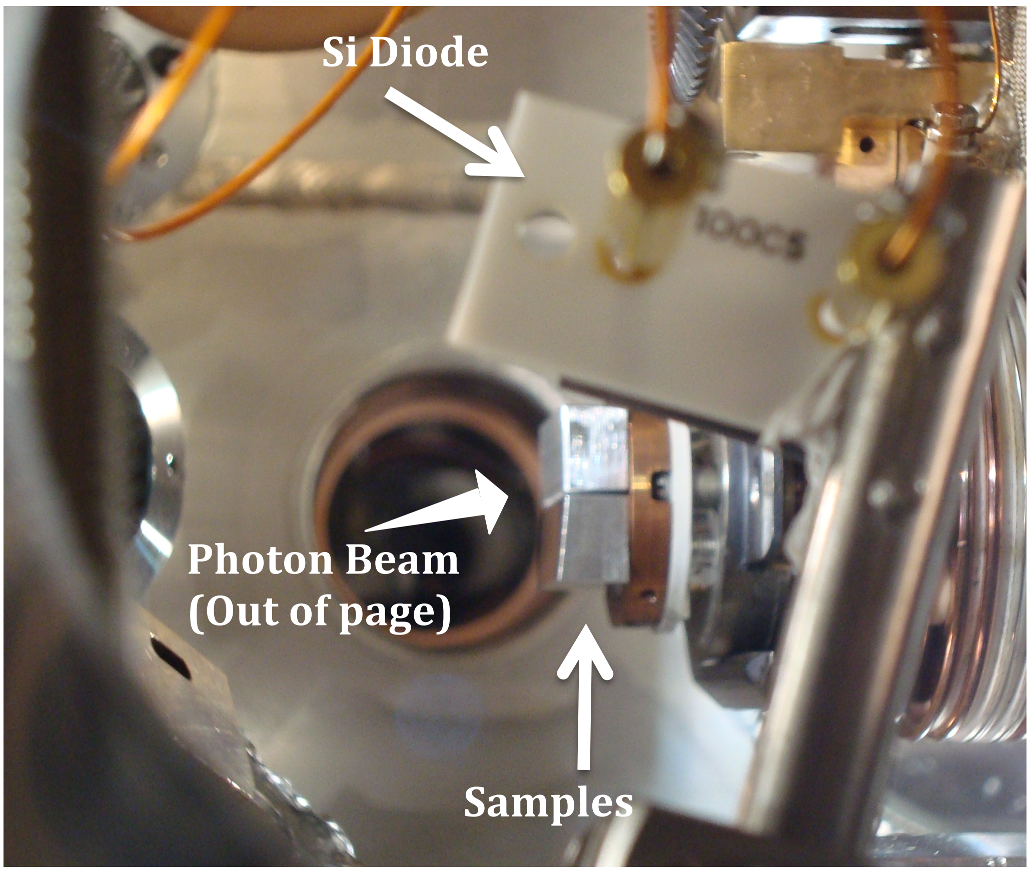

Fig. 9.3. Layout of the beam line measurement chamber, the photon beam is out of the page. The Silicon diode is used to measure the photon flux when the samples have been moved out of the path of the photon beam.

The two samples measured were sections of extruded aluminum APS beam chamber. Figure 9.4 shows the samples measured. The polished sample is on the top, and the as-received sample is on the bottom. Sample details were described in section 5.5.

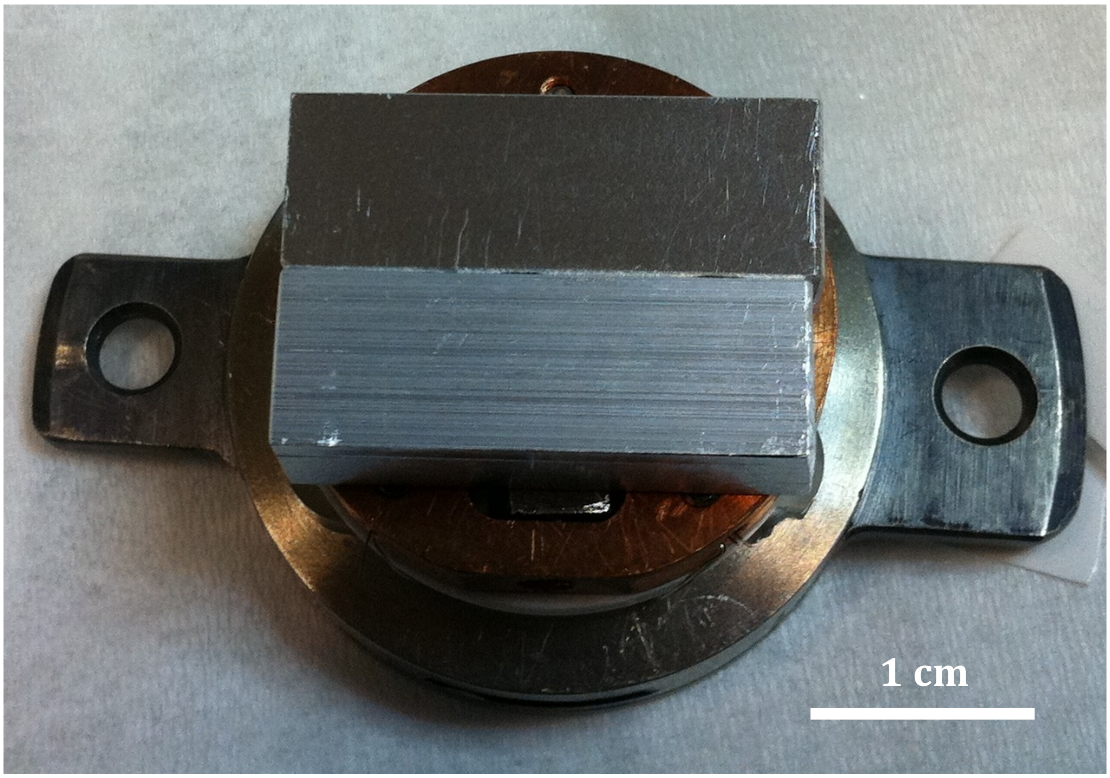

Fig. 9.4. Picture of the sample holder with both aluminum samples. The polished sample is on the top, the as-received sample is on the bottom.

The surface roughness of both samples were measured before the QE measurement, see Table 5.2. During transport the sample surfaces were protected using Kapton tape. Before the measurements were taken the samples were cleaned in an ultrasonic, acetone bath for ten minutes, and dried with dry nitrogen. After the measurements were taken we discovered that the acetone did not remove the tape residue. From [58] it was assumed that the surface had an 11 nm Al_2O_3 layer from exposure to the air at the time of the measurement.

9.3 Analysis

To calibrate the total photon flux on the sample, the drain current from the Silicon diode at the back of the sample chamber, Figure 9.3, was measured for all photon energies. To measure the drain current on the Silicon diode the sample had to be moved out of the path of the photon beam. Using the calibration for the Silicon diode given by the manufacturer [59], the flux at each photon energy can be calculated from Equation 9.1.

$$F_{Photon} = \frac{I_{Si}}{q_e} \frac{3.65eV}{\text{electron}} \frac{1}{E_\gamma} F(E_\gamma) \left[\frac{photons}{sec}\right] \tag{9.1}$$

F_{Photon} is the photon flux, I_{Si} is the drain current measured from the Silicon diode, 3.65 eV is the average energy for an electron-hole pair creation in silicon, E_γ is the energy of the incident photon beam, q_e is the charge of an electron, and $F(E_\gamma)$ is the transmission coefficient [32]. For the photon energies used in the QE measurement $F(E_\gamma)$ is close to one and photoemission dominates as the electron production process. With the sample in place all photons that would have been incident on the diode are now incident on the sample, therefore the photon flux on the sample is also given by Equation 9.1. The drain current from the sample was measured to determine the number of free electrons produced. Using Equation 9.2, the number of electrons produced can be calculated.

$$F_{Electron} = \frac{I_{Al}}{q_e} \left[\frac{electrons}{sec}\right] \tag{9.2}$$

$F_{Electron}$ is the electron flux, I_{Al} is the drain current measured from the aluminum sample. The QE is the ratio of number of electrons emitted to number of incident photons, as seen in Equation 9.3.

$$QE = \frac{F_{Electron}}{F_{Photon}} \tag{9.3}$$

All results were normalized to the storage ring beam current.

For the APS SCU the beam chamber is nominally held at 20 K. To determine if there is an effect on the QE the temperature of the sample was varied from 180 K to 300 K. The minimum temperature of 180 K was a limit of the beam line used to take the measurement. The sample drain current measurements were taken as the sample was being cooled. Measurements of the QE taken at 300 K and 180 K for a 10 degree grazing angle were compared to determine the temperature dependance of the QE. The QE for the sample at 180 K, over all energies, did not vary more than 15% from the QE at 300 K. Carbon monoxide and H_2 are the most abundant gases in the vacuum chamber [12], these gases condense at temperatures 81 K for CO [60] and 20 K for H_2 [61]. All measurements presented in this paper were taken above 180 K, so the surface of the samples are not altered due to cryo-sorbed gases. Future studies must be done to determine a realistic QE values for the APS SCU chamber at 20K. Results presented in this paper do not consider the temperature differences in sample during the measurement.

9.4 Results

The QE as a function of energy was found to be strongly dependent on the energy of the incident photon beam. The QE of the aluminum chamber with a photon beam at a grazing angle of 5 degrees is shown in Figure 9.5 for both samples, the polished sample has a greater QE in the energy spectrum measured. There are peaks in the QE for photon energies equal to the K1s edges of oxygen, carbon, and aluminum. The oxygen and carbon are part of the Al_2O_3 layer, typically 11 nm thick [58], that forms on aluminum from exposure to the air. The next two sections detail the results based on photon grazing angle, and sample surface roughness.

9.4.1 Angle dependance

To study the dependance of the QE on the incident photon angle the average QE was calculated for each angle and sample and then fit to a Lorentzian as a function

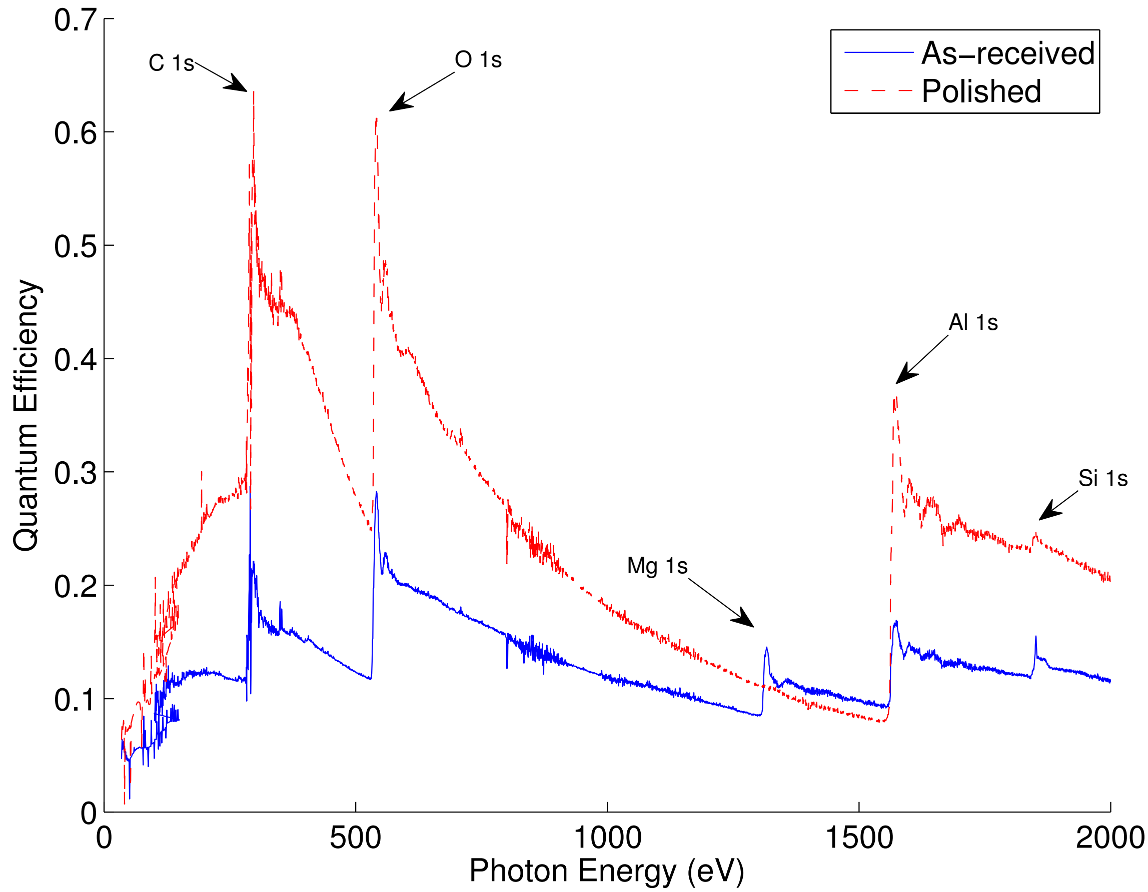

Fig. 9.5. An example of a QE plot as a function of energy. These data were taken with the incident photons at a grazing angle of 5 degrees.

of angle, Figure 9.6. Similarly the peak QE was plotted for each angle then fit to a Lorentzian as a function of angle, Figure 9.7. A Lorentzian was used to include the 50 degree data in the fit, which required a long tail that didn't go to zero.

The angle dependance of the QE is related to the penetration depth of photons. For a set energy the photons travel the same distance through the material for all grazing angles; however, the photons are absorbed closer to the surface when the grazing angle is low [62]. For low angles the escape probability of the photoelectrons is greater, increasing the QE.

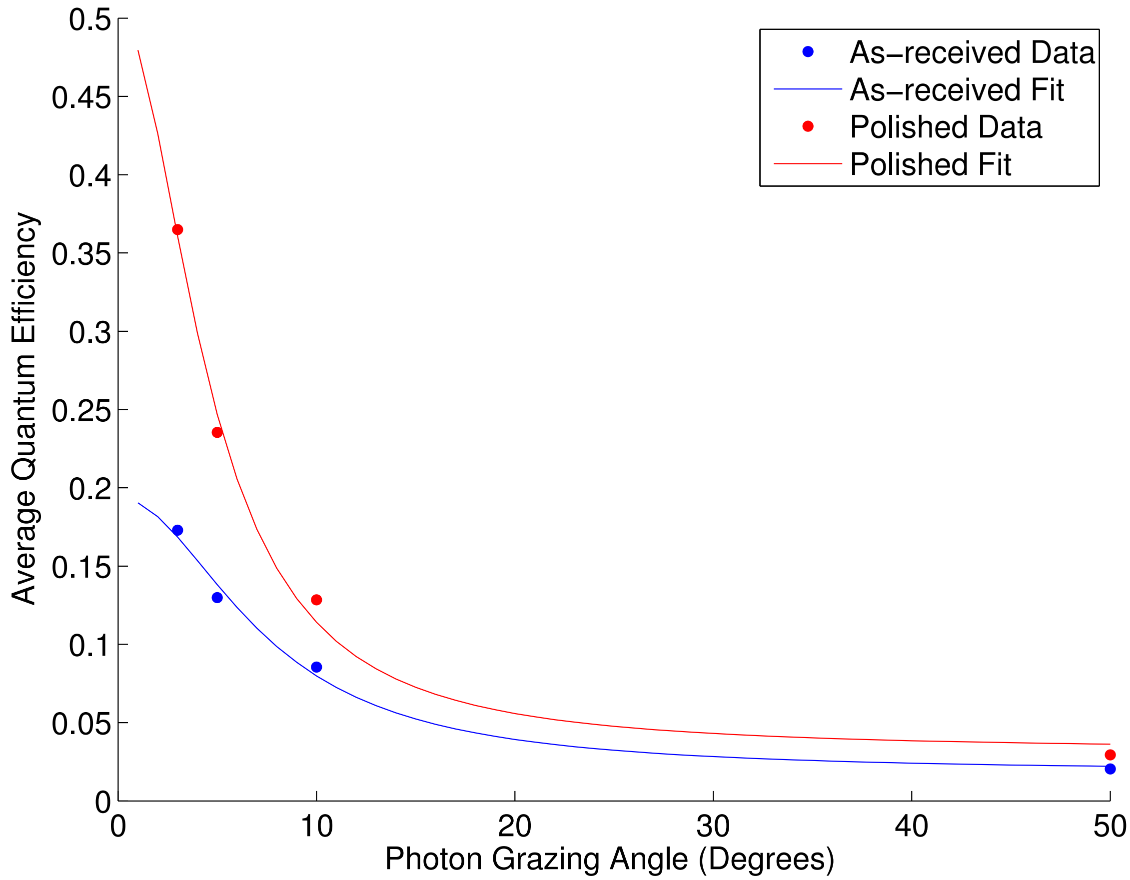

Fig. 9.6. The average QE plotted as a function of photon grazing angle. Higher photon grazing angles have a smaller QE than low grazing angles.

To use these data in current electron cloud generation codes, the QE for angles less than the measured three degrees would need to be interpolated from the data. Figure 9.6 and Figure 9.7 show a good fit with a Lorentzian for photon grazing angles between 3 and 50 degrees, and the QE for less than three degrees is interpolated from the fit. The lack of data at low grazing angles is a limitation of this model. The Lorentzian fit is not a good physical model of the QE at grazing angles less than 1.5 degrees. As the grazing angle decreases at some point the QE will decrease to 0 for an atomically flat surface. The shape of this decline was not studied for this paper.

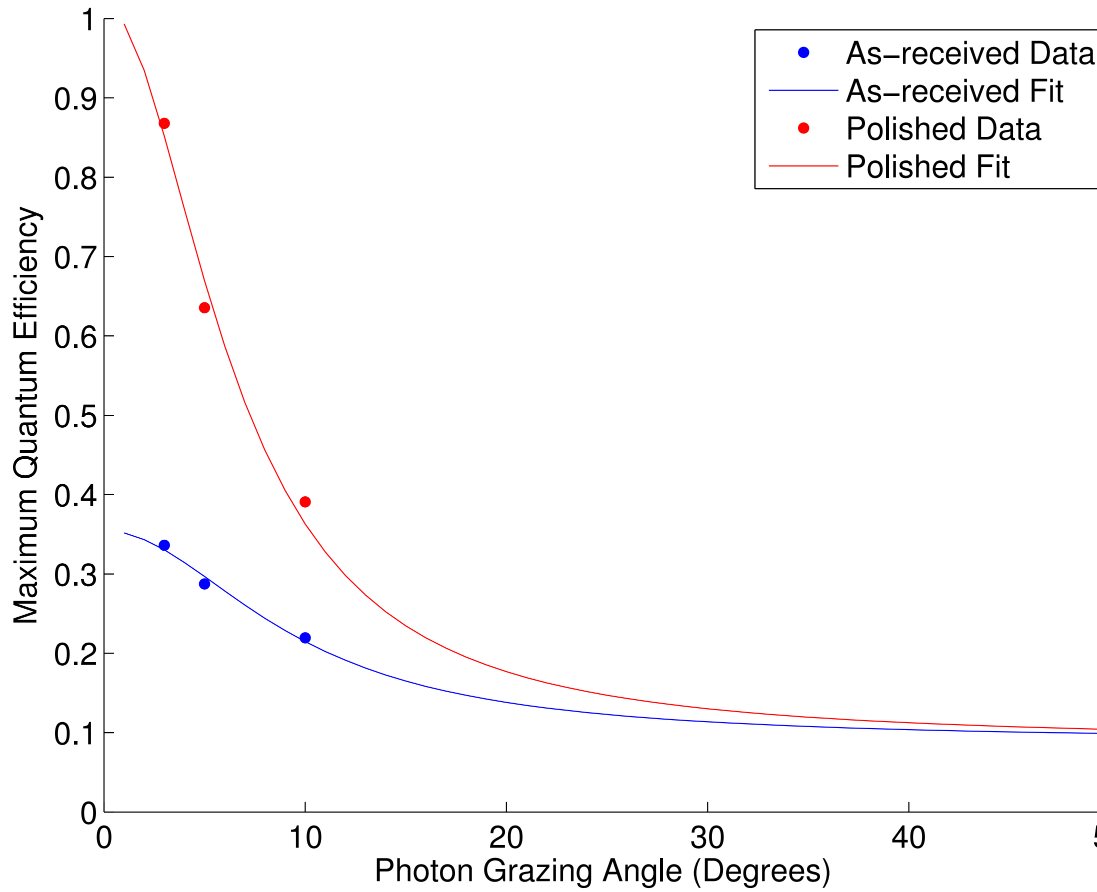

Fig. 9.7. The peak QE plotted as a function of photon grazing angle. Higher photon grazing angles have a smaller QE than low grazing angles.

9.4.2 Surface Roughness dependance

From Figure 9.6 and Figure 9.7 it is seen that the polished sample had a higher overall QE than the as-received sample. In [63] rougher surfaces were found to have higher QE than smoother surfaces. The reason for the difference is the voltage bias on the sample, which is a technique typically used when measuring the QE. To better simulate the working conditions of a beam chamber in the accelerator, a voltage bias was not put on the samples during the measurement. Therefore electrons have a probability of being reabsorbed into the sample and not measured, reducing the

QE, Figure 9.8. This effect increases with a rougher surface, since individual electrons have a higher probability of hitting the surface again. This is consistent with current electron cloud secondary electron yield mitigation research where the secondary electron yield is reduced when grooves are added to the beam chamber surface [64].

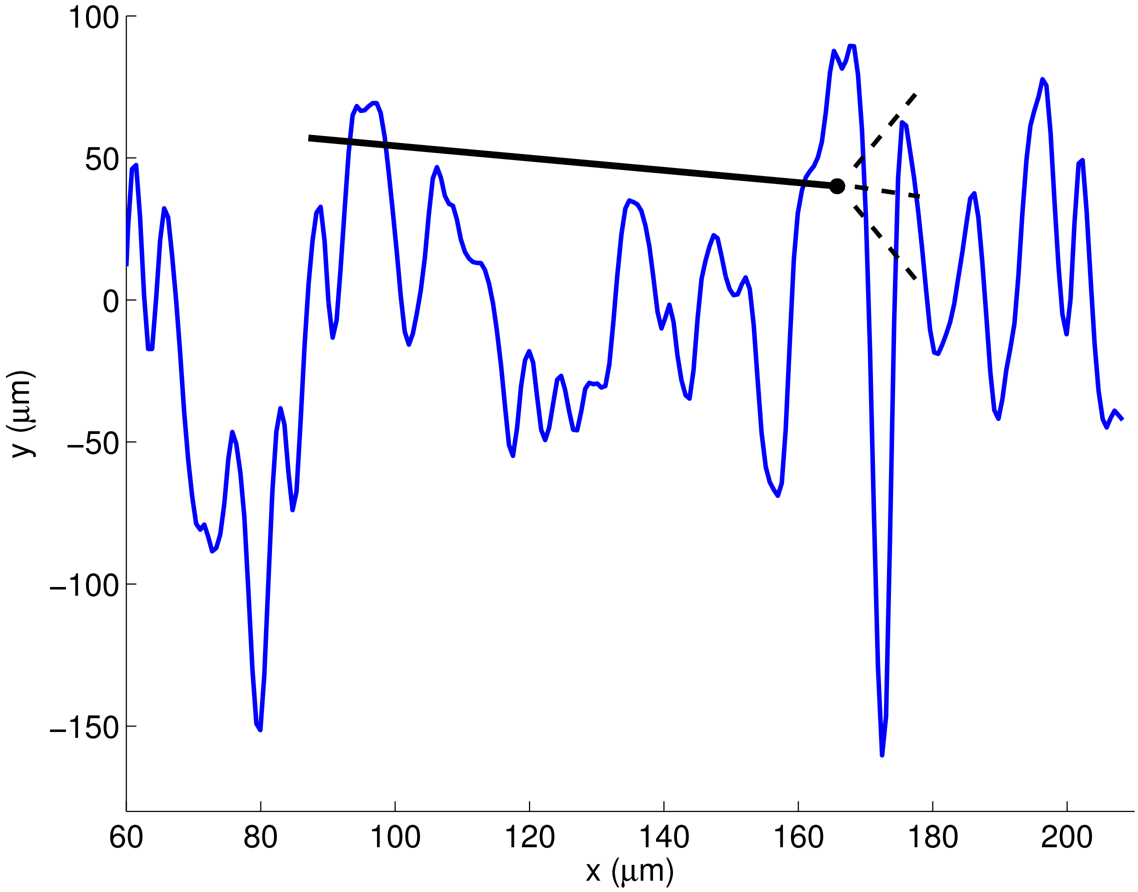

Fig. 9.8. Without a voltage bias on the sample photoelectrons can hit the sample again, before the electron is measured. The probability increases for rougher surfaces.

9.5 Effective QE

The effective QE is the QE at each photon energy averaged over the photon grazing angle distribution at that energy. The photon distribution was based on simulations from Synrad3D. This calculation is a better representation of the QE in a small aperture chamber than the measurement alone, since it considered the photon angle as well as its energy in the calculation.

To estimate the QE as a function of the incident angle the theory from [65] was fit to the data at each photon energy.

$$QE(\theta) = \frac{1 - R(\theta)}{1 - R(normal)} \times \frac{1 + \mu L_s}{\cos(\theta) + \mu L_s} \times \frac{1 - \exp\left[-T\left(\frac{\mu}{\cos(\theta)} + \frac{1}{L_s}\right)\right]}{1 - \exp\left[-T\left(\mu + \frac{1}{L_s}\right)\right]} \tag{9.4}$$

where R(θ) is the reflectivity of aluminum at the angle θ, and R(normal) is the reflectivity at normal incidence. The reflectivity values were taken from [32] assuming an 11 nm layer of Al_2O_3 on an Al substrate, and no surface roughness. The variable μ is the mass absorption coefficient, and is dependent on the photon energy [66], and λ is the electron mean free path in aluminum. Specular reflection was assumed for all angles. The QE theory was scaled by a factor, s, at each photon energy to fit the QE data taken. Shown in Figure 9.9 is the theory fit to data at 1300 eV, a scale factor of 0.5 was used.

As the photon energy increases the peak QE shifts to lower grazing angles. To apply this equation to the simulation results, the theory was fit to data for the range of photon energies between 35 eV and 2000 eV. Then each macro-photon's theoretical QE was found based on its energy and grazing angle. Finally the QE's were averaged for each photon energy, results are shown in Figure 9.10.

The Oxygen, Carbon and Aluminum peaks are still visible, but the Oxygen K 1s peak has been amplified. This occurs because the absorbed photons have a small grazing angle so the thick oxide layer dominates the photoelectron production at that energy. The peak effective QE for the polished chamber at the oxygen K 1s line at 544 eV is 1.023, which is greater than unity. Some error is introduced because of finite energy resolution at the strongly-peaked K 1s line in the reflectivity curve. The polished chamber has a higher effective QE than the as-received chamber, as seen in the raw data results described in previous sections. The details in the effective QE

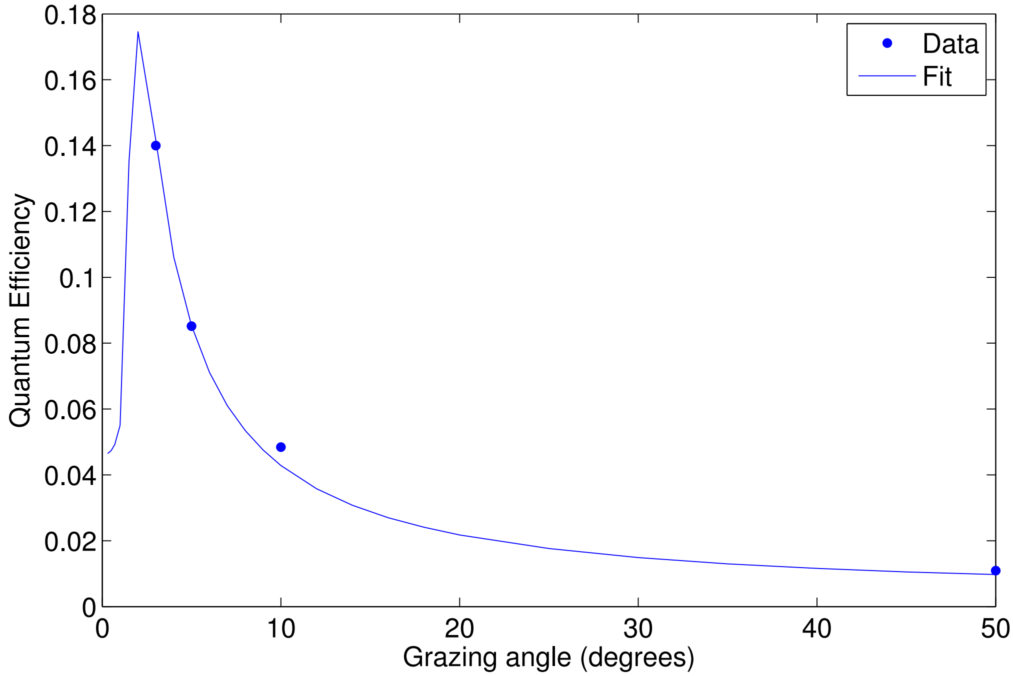

Fig. 9.9. Fit of the theory to the QE measurements at photon energy 1300 eV.

suggest that representing QE with a single value in election cloud codes may be an over-simplification.

9.6 Summary

In this chapter the results from a QE measurement for two technical aluminum surfaces extruded for an APS small aperture beam chamber were presented. Measurements were taken at photon energies from 35 eV to 2000 eV, and at grazing angles 3, 5, 10 and 50 degrees. The results compared the effects of the QE on surface roughness, photon energy and photon incident angle. The QE peaks at photon energies equal to the K 1s shells of the Oxygen, Carbon, Aluminum and Silicon in the samples. The highest peaks where for the Oxygen and Carbon shells. To determine the

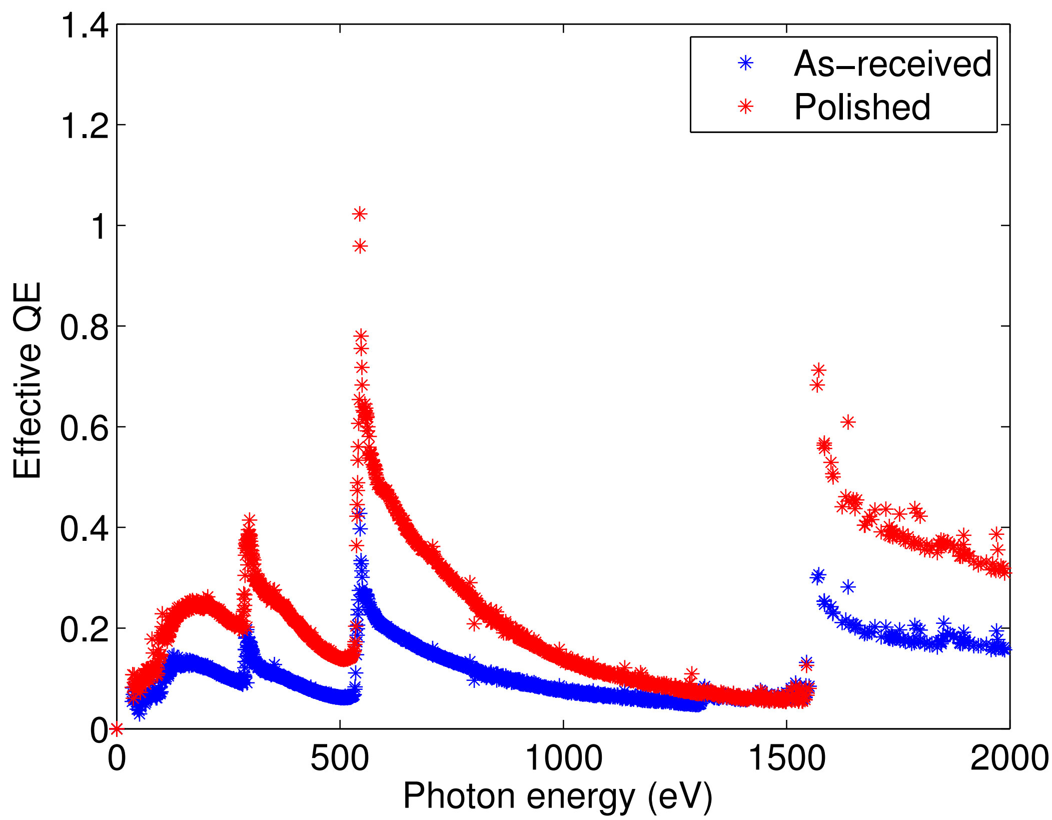

Fig. 9.10. The effective QE spectrum, including the photon grazing angle distribution.

angle dependance of the QE the average QE for each angle was compared. Results showed that the QE decreased as the incident photon angle increased. The angular dependence of QE was fit to a Lorentzian to give an estimate on the QE for incident angles less than 3 degrees. In the photon energy and grazing angle measurements the QE for an as-received and polished sample are shown. The difference in the QE for the two samples is greatest for low photon energies at low grazing angles, but as the photon energy approaches 2000 eV and 50 degrees grazing angle the difference in the measured QE is reduced. Finally the effective QE was calculated to combine the results with the distribution of photon grazing angles. This amplified the QE for the oxygen K 1s line at 544 eV, and suggest that a more complete photoemission model in electron cloud codes is needed.

10. SUMMARY

There were several key results in the development of an accurate model of the radiation heat load on the APS SCU.

An analytical model of synchrotron radiation from a steered electron beam in a bending magnet was produced. Using this analytical model it was shown that an electron beam vertically off-axis in the upstream dipole can produce more radiation on the SCU chamber wall than the maximum power the cryo-pumps can handle, chapter 6.

Monte-Carlo simulations with no-scattering had good agreement with the analytical model, for an ideal electron beam orbit and when the orbit has a vertical offset or angle in the upstream dipole magnet. These simulations assumed that all photons incident on the beam chamber were absorbed. This work showed the importance of including diffuse scattering in the simulation to create a realistic photon distribution azimuthally around the chamber. A diffuse scattering model was used to simulate the radiation heat load from a realistic chamber model. The realistic chamber model showed a 95% decrease in radiation heating compared to the no-scattering simulation. The polished SCU chamber walls increased photon reflections, while the un-polished chamber everywhere else had a low reflectivity, and absorbed the photons.

By applying a complete radiation heat load model we had an error of less than 20% between the analytical prediction and measurements for small vertical orbit bumps in the upstream dipole. This comparison shows better agreement between prediction and measurements than what has been achieved at other synchrotron laboratories. The results of simulations and measurements diverged only for the vertical steering outside the Beam Position Limiting Detector limits. This discrepancy of 65% could be from photon scattering out of the chamber. However even for large vertical bumps this analytical model was able to predict the radiation heat load to better accuracy than any previously published heat load analysis.

Quantum Efficiency(QE) measurements of technical aluminum samples were taken at photon energies from 35 eV to 2000 eV, and at grazing angles 3, 5, 10 and 50 degrees. The results compared the effects of the QE on surface roughness, photon energy and photon incident angle. The QE peaks at photon energies equal to the K shells of the Oxygen, Carbon, Aluminum and Silicon in the samples. The difference in the QE for the as-received and polished samples is greatest for low photon energies at low grazing angles, but as the photon energy approaches 2000 eV and 50 degrees grazing angle the difference in the measured QE is reduced. These measurements demonstrated that models of the photoelectron yield of technical accelerator surfaces need to include the variation of QE with photon energy and angle.

In conclusion, the analytical model developed in this thesis accurately predicted the measured radiation heat load on a small aperture superconducting device installed in a high energy electron storage ring, with substantially improved accuracy over previous efforts.

APPENDIX

A. SECTOR LAYOUT

This Appendix will describe the details of the SCU0 sector in the accelerator. It includes a description of all the chamber designs used in this research, and each of the layouts analyzed as part of this thesis. Including the relative distance between the bending magnet, SCU photon absorber and SCU, also the distance between the beam chamber center and the tip of the potion absorber. Each subsection will highlight the important changes made for each layout.

A.1 Chamber Cross-section

In addition to the SCU ellipse chamber that is in the SCU cryostat section 5.4, three other chamber shapes were used upstream of SCU. This section will describe each shape and describe how it was modeled.

A.1.1 Main Chamber

The main chamber is used through the ring except in sections with a small gap insertion device(ID). The main chamber vertical aperture is 4.2 cm, the horizontal aperture is 8.7 cm. The outside of the chamber is extended to create an anti-chamber, which provides a path for synchrotron radiation to pass out of the vacuum chamber and reduces vacuum pressure rise. Figure A.1 shows the shape of the main chamber with the antechamber.

To model the main chamber the top and bottom were assumed to be circles of radius 53.7 mm and the inside end of the chamber was modeled as a circle with radius 7.9 mm. These two curves are connected with a straight line with a length of 13 mm.

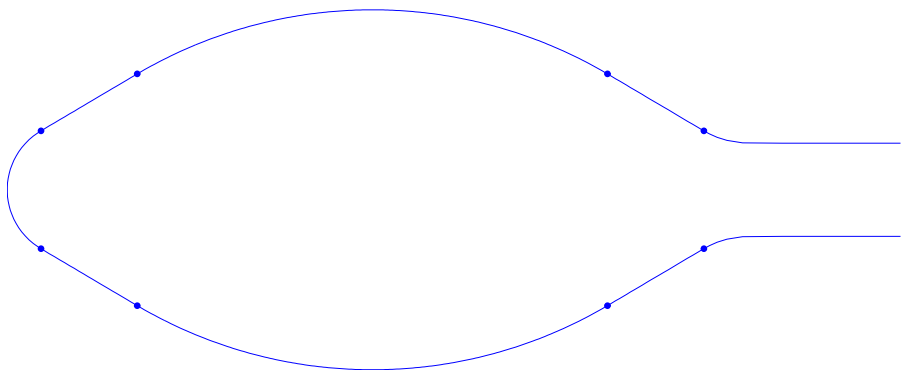

Fig. A.1. Cross section of the main chamber.

A.1.2 ID Chamber

To create a greater magnetic field in the ID's a small aperture chamber is used. The standard ID chamber has a vertical aperture of 7.5 mm with each end rounded off with a circle of radius 3.75 mm. The full horizontal aperture is 36 mm. Included in the simulation was the antechamber with a vertical aperture of 5 mm, Figure A.2.

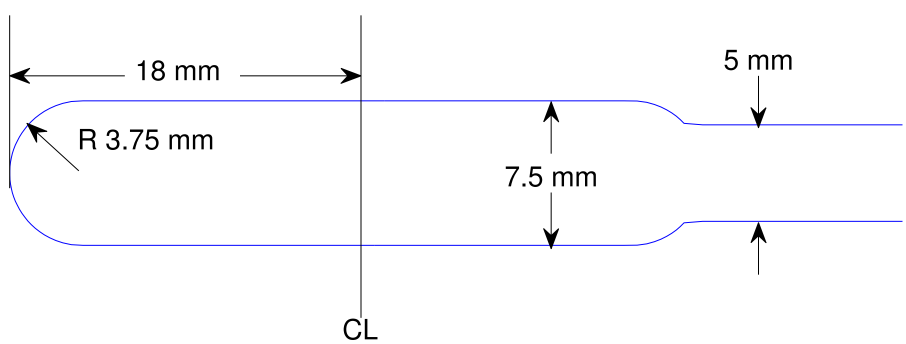

Fig. A.2. Cross section of the ID chamber.

A.1.3 SCU Oval

This chamber cross-section was only used in early designs of the chamber layout The SCU oval has the same horizontal and vertical aperture as the SCU ellipse, but is flat along the top and bottom edges Figure A.3. The chamber does not have an antechamber, and was simulated with half circles on the inside and outside edges with a radius of 3.6 mm.

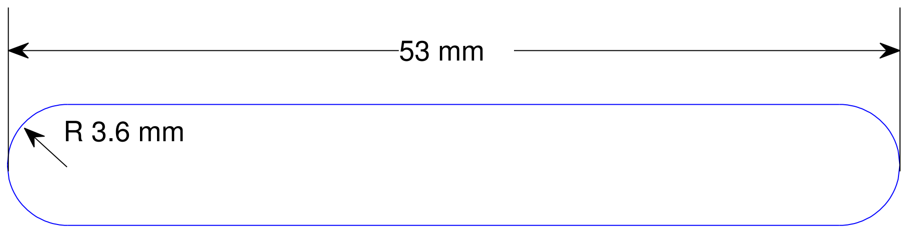

Fig. A.3. Cross section of the SCU oval chamber.

A.1.4 Transition Oval

This chamber cross-section is only used in the installed cryostat. The horizontal aperture is slightly larger then the SCU ellipse, 59 mm, but the vertical aperture is approximately four times larger at 25.4 mm full aperture. This chamber is used as a transition between the main chamber and the SCU ellipse. It was modeled with two half circles on either side with a radius of 12.7 mm, connected by a straight line.

A.2 Layout Descriptions

This section will describe the details of each of the layouts simulated as part of this thesis. For Layouts 1, 2 and 4 the SCU photon absorber was 17 mm from the chamber center. For Layout 3 the SCU photon absorber was 17.94 mm from the

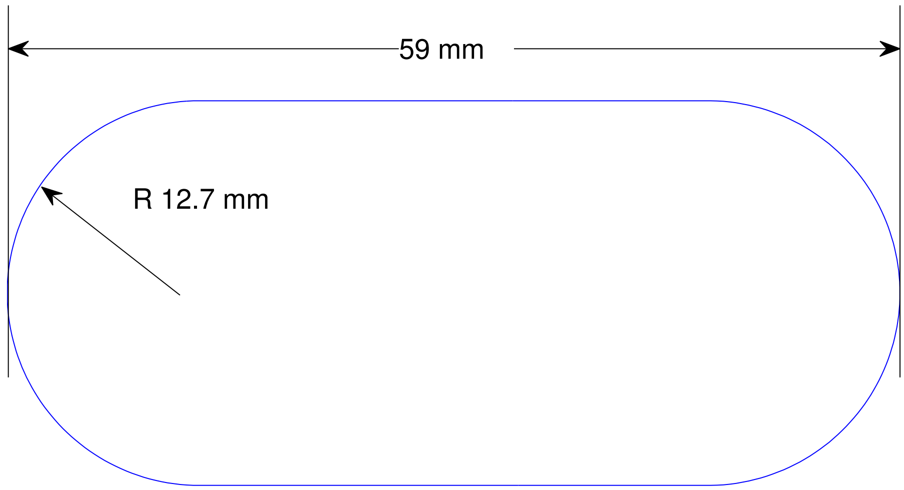

Fig. A.4. Cross section of the transition oval.

beam chamber. In all of the layouts the photon absorber is 75 cm long positioned at an angle of 30 degrees [38].

All the element positions are defined as the distance from the end of the main bending magnet.

A.2.1 Layout 1

Layout 1 is the initial SCU0 design used for radiation heating calculations. The chamber tapers from a small aperture ID chamber shape to an SCU oval in the downstream end box of the standard undulator. There is a short (<1 mm) transition to the SCU ellipse chamber inside the cryostat.

A.2.2 Layout 2

The step from the SCU oval to the SCU ellipse in the cryostat increases the power on that section of the beam chamber in the cryostat. The heat load on this one section accounts for approximately 24% of the total direct radiation heating, on a 1 mm section. To decrease the heating on the step in the SCU cryostat, a mask,

Table A.1
Distance between the end of the Bending magnet and specified positions for Layout 1.

Description	**Distance**
EA5 photon absorber	4.696 m
Center of the BH1 magnet	4.686 m
Start of the taper from ID chamber to SCU oval	7.763 m
Tip of the SCU photon absorber	7.838 m
End of the taper from ID chamber to SCU oval	7.896 m
Beginning of SCU ellipse (step)	8.351 m
Step from SCU ellipse to SCU oval, end of the SCU	9.971 m

designed by Emil Trakhtenberg, will be placed 22 cm upstream of the step. This mask has the same shape as the SCU ellipse, is 1.3 mm in length. The addition of the mask is effective in decreasing the heat load on the step by 75%.

Table A.2
Distance between the end of the Bending magnet and specified positions for Layout 2.

Description	**Distance**
EA5 photon absorber	4.696 m
Center of the BH1 magnet	4.686 m
Start of the taper from ID chamber to SCU oval	7.763 m
Tip of the SCU photon absorber	7.838 m
End of the taper from ID chamber to SCU oval	7.896 m
Center of mask	8.056 m
Beginning of SCU ellipse (step)	8.351 m
Step from SCU ellipse to SCU oval, end of the SCU	9.971 m

A.2.3 Layout 3

A test chamber was installed in APS in May 2012 to measure the heat load on a small aperture ID chamber before the SCU cryostat was installed. The test chamber is an SCU ellipse chamber which extended from the upstream undulator to the end of the straight section. It did not include the step or mask. For these calculations the SCU photon absorber was assumed to be 17.94 mm from the beam chamber center.

Table A.3
Distance between the end of the Bending magnet and specified positions for Layout 3.

Parameter	**Distance**
Center of the BH1 magnet	4.696 m
EA5 photon absorber	4.686 m
Tip of the SCU photon absorber	7.83 m
Beginning of the SCU	8.23 m
End of the SCU	10.31 m

A.2.4 Layout 4

After an RF finger melted in the transition section of the test chamber described in subsection A.2.3 that section was redesigned for the installed device. The chamber now tapers out to the main chamber design in the end box of the upstream undulator, then tapers back to the transition oval before the cryostat. The chamber transitions down to the SCU ellipse aperture inside the cryostat.

Table A.4
Distance between the end of the Bending magnet and specified positions for Layout 4.

Parameter	**Distance**
Center of the BH1 magnet	4.696 m
EA5 photon absorber	4.686 m
Start of the taper from ID chamber to main chamber	7.763 m
Tip of the SCU photon absorber	7.838 m
End of the taper from ID chamber to main chamber	7.917 m
Beginning of taper from main chamber to transition oval	8.091 m
Beginning of taper from transition oval to SCU ellipse	8.239 m
End of taper from transition oval to SCU ellipse	8.353 m
First thermal link	8.603 m
Last thermal link	9.933 m
End of SCU	10.298 m

LIST OF REFERENCES

LIST OF REFERENCES

[1] Y. Ivanyushenkov, M. Abliz, K. Boerste, T. Buffington, C. Doose, J. Fuerst, Q. Hasse, M. Kasa, S. H. Kim, R. Kustom, V. Lev, N. A. Mezentsev, E. R. Moog, D. Skiadopoulos, V. Syrovatin, V. Tsukanov, E. M. Trakhtenberg, I. B. Vasserman, and J. Xu, "Development of a Planar Superconducting Undulator for the Advanced Photon Source," *IEEE Trans. Appl. Supercond.*, vol. 22, p. 4100804, June 2012.

[2] M. Billing, G. Dugan, M. J. Forster, R. E. Meller, M. A. Palmer, G. A. Ramirez, K. Sonnad, J. P. Sikora, H. A. Willians, R. L. Holtzapple, and K. G. Sonnad, "Measurement Techniques to Characterize Instabilities caused by Electron Clouds," in *Proceedings of the Particle Accelerator Conference 2011lerator Conference 2011*, (New York, NY, USA), p. WEP194, JACoW, March 2011.

[3] M. G. Billing, G. Dugan, M. J. Forster, D. L. Kreinick, R. E. Meller, M. A. Palmer, G. Ramirez, N. T. Rider, M. Rendina, K. Sonnad, J. P. Sikora, H. A. Williams, R. L. Holtzapple, M. Randazzo, J. Y. Chu, and J. W. Flanagan, "Status of Electron Cloud Dynamics Measurements at CesrTA," in *Proceedings of the International Particle Accelerator Conference 2011*, (San Sebastian, Spain), p. MOPS084, JACoW, September 2011.

[4] J. Crittenden, J. Conway, G. Dugan, M. A. Palmer, D. L. Rubin, J. Shanks, K. G. Sonnad, L. Boon, K. Harkay, T. Ishibashi, M. A. Furman, S. Guiducci, M. T. F. Pivi, and L. Wang, "Investigation into electron cloud effects in the International Linear Collider positron damping ring," *Phys. Rev. ST Accel. Beams*, vol. 17, no. 031002, 2014.

[5] O. Dominguez, K. Li, G. Arduini, E. Métral, G. Rumolo, F. Zimmermann, and H. Maury Cuna, "First electron-cloud studies at the Large Hadron Collider," *Phys. Rev. ST Accel. Beams*, vol. 16, no. 011003, 2013.

[6] E. Mahner, T. Kroyer, and F. Caspers, "Electron cloud detection and characterization in the CERN Proton Synchrotron," *Phys. Rev. ST Accel. Beams*, vol. 11, no. 094401, 2008.

[7] J. R. Calvey, G. Dugan, W. Hartung, J. A. Livezey, J. Makita, and M. A. Palmer, "Measurement and modeling of electron cloud in a field free environment using retarding field analyzers," *Phys. Rev. ST Accel. Beams*, vol. 17, Jun 2014.

[8] D. R. Grosso, M. Commisso, R. Cimino, R. Larciprete, R. Flammini, and R. Wanzenberg, "Effect of the surface processing on the secondary electron yeild of Al alloy samples," *Phys. Rev. ST Accel. Beams*, vol. 16, no. 051003, 2013.

[9] S. Casalbuoni, M. Hagelstein, B. Kostka, R. Rossmanith, M. Weisser, E. Steffens, A. Bernhard, D. Wollmann, and T. Baumbach, "Generation of X-ray radiation

in a storage ring by a superconductive cold-bore in-vacuum undulator," *Phys. Rev. ST Accel. Beams*, vol. 9, January 2006.

[10] K. C. Harkay, L. E. Boon, M. Borland, G. Decker, R. J. Dejus, J. C. Dooling, C. L. Doose, L. Emery, J. Gagliano, E. Gluskin, Q. B. Hasse, Y. Ivanyushenkov, M. Kasa, J. C. Lang, D. Robinson, V. Sajaev, K. M. Schroeder, N. Sereno, Y. Shiroyanagi, D. Skiadopoulos, M. L. Smith, E. Trakhtenberg, A. Xiao, and A. Zholents, "APS Superconducting Undulator Beam Commissioning Results," in *Proceedings of the North American Particle Accelerator Conference 2013*, (Pasadena, CA, USA), p. WEOAA3, JACoW, September 2013.

[11] K. Harkay, R. Rosenberg, and L. Loiacono, "Measuring the Properties of the Electron Cloud at the Advanced Photon Source," in *ICFA Beam Dynamics Newsletter* (K. Ohmi and M. Furman, eds.), vol. 33 of *ICFA Beam Dynamics Newsletter*, pp. 43–52, International Committee for Future Accelerators, April 2004.

[12] S. Casalbuoni, A. Grau, M. Hagelstein, R. Rossmanith, F. Zimmermann, B. Kostka, E. Mashkina, E. Steffens, A. Bernhard, D. Wollmann, and T. Baumbach, "Beam heat load and pressure rise in a cold vacuum chamber," *Phys. Rev. ST Accel. Beams*, vol. 10, no. 093202, 2007.

[13] N. Mahne, A. Giglia, S. Nannarone, R. Cimino, and C. Vaccarezza, "Experimental Determination of e-cloud simulation input parameters for DAΦNE," in *Proceedings of the Particle Accelerator Conference 2005*, no. EUROTEV-REPORT-2005-013, (Knoxville, TN, USA), p. FPAP002, JACoW, May 2005.

[14] R. Cimino, I. R. Collins, and V. Baglin, "VUV photoemission studies of candidate Large Hadron Collider vacuum chamber materials," *Phys. Rev. ST Accel. Beams*, vol. 2, no. 063201, 1999.

[15] E. Wallén and G. LeBlanc, "Cryogenic system of the MAX-Wiggler," *Cryogenics*, vol. 44, pp. 879–893, 2004.

[16] A. Bernhard, S. Casalbuoni, R. Frahm, B. Griesebock, U. Haake, M. Hagelstein, B. Kostka, Y. Mathis, A. Muller, R. Rossmanith, F. Schock, E. Steffens, M. Weier, D. Wollmann, and T. Baumbach, "Performance of the First Superconducting Cold-Bore Undulator in an Electron Storage Ring," *IEEE Trans. Appl. Supercond.*, vol. 17, pp. 1235 – 1238, June 2007.

[17] J. C. Jan, C. S. Hwang, P. H. Lin, and F. Y. Lin, "Design and Improvement of a Mini-Pole Superconducting Undulator at NSRRC," *IEEE Trans. Appl. Supercond.*, vol. 18, pp. 427–430, June 2008.

[18] R. A. Rosenberg and K. C. Harkay, "A Rudimentary Electron Energy Analyzer for Accelerator Diagnostics," *Nucl. Instrum. Methods Phys. Res., Sect. A*, vol. 453, pp. 507–513, March 2000.

[19] S. Gerstl, S. Casalbuoni, A. W. Grau, D. Saez de Jauregui, T. Holubek, R. Voutta, R. Bartolini, M. Cox, E. Longhi, G. Rehm, J. Schouten, R. Walker, M. Migliorati, and B. Spataro, "Beam Heat Load Measurements with COLDDIAG at the Diamond Light Source," in *Proceedings of the International Particle Accelerator Conference 2011nternational Particle Accelerator Conference*, (Shanghai, China), p. WEPWA006, JACoW, May 2013.

[20] S. Gerstl, T. Baumbach, S. Casalbuoni, A. Grau, M. Hagelstein, D. Saez de Jauregui, T. Holubek, R. Bartolini, M. Cox, J. Schouten, R. Walker, M. Migliorati, I. R. R. Shinton, and B. Spataro, "First Measurements of COLDDIAG: A Cold Vacuum Chamber for Diagnostics," in *Proceedings of the International Particle Accelerator Conference 2012*, (New Orleans, LA, USA), p. MOPPP069, May 2012.

[21] S. Gerstl, *A COLD Vacuum Chamber for Beam Heat Load DIAGnostics (COLDDIAG).* PhD thesis, Karlsruher Instituts Fur Technologie (KIT), 2013.

[22] S. Gerstl, R. Voutta, S. Casalbuoni, A. W. Grau, T. Holubek, D. Saez de Jauregui, R. Bartolini, M. Cox, E. Longhi, G. Rehm, J. Schouten, R. Walker, G. Sikler, M. Migliorati, and B. Spataro, "Cold Vacuum Chamber for Diagnostics: Instrumentation and First Results," *Phys. Rev. ST Accel. Beams*, vol. 12, p. 013201, October 2014.

[23] O. Malyshev, J. Lucas, N. Collomb, S. Postlethwaite, M. Korostelev, A. Wolski, and K. Zolotarev, "Mechanical and Vacuum Design of the Wiggler section of the ILC damping rings," in *Proceedings of the International Particle Accelerator Conference 2010*, (Kyoto, Japan), p. WEPE092, JACoW, May 2010.

[24] L. Boon, "Radiation Heating from the ILC Damping Wigglers," in *Proceedings of the International Workshop on Linear Colliders*, (Arlington, Texas), October 2012.

[25] "Advanced Photon Source Upgrade Project Conceptual Design Report (CD-1)," Tech. Rep. APSU-1.1-PLN-002-02.1, Argonne National Laboratory, Argonne, IL, USA, May 2011.

[26] D. J. Griffiths, *Introduction to Electrodynamics.* Upper Saddle River, NJ, USA: Prentice-Hall, 3rd ed., September 1999.

[27] A. Hofmann, *The Physics of Synchrotron Radiation.* No. 20 in Cambridge Monographs on Particle Physics Nuclear Physics and Cosmology, Cambridge, United Kingdom: Cambridge University Press, 2004.

[28] H. Wiedemann, *Particle Accelerator Physics.* Berlin, Germany: Springer-Verlag, 3rd ed., 2007.

[29] D. T. Attwood, "Introduction to Synchrotron Radiation Bending Magnet Radiation," 2007.

[30] G. F. Dugan and D. Sagan, "Synrad3D Photon Propagation and Scattering Simulation," in *Proceedings of ECLOUD10, the 49th ICFA Advanced Beam Dynamics Workshop on Electron Cloud Physics*, (Ithaca, NY, USA), p. PST08, International Committee for Future Accelerators, October 2010.

[31] D. Sagan, *The BMAD Reference Manual.* Cornell University.

[32] B. L. Henke, E. M. Gullikson, and J. C. Davis, "X-Ray Interactions: Photoabsorption, Scattering, Transmission, and Reflection at E = 50-30,000 eV, Z = 1-92," *At. Data and Nucl. Data Tables*, vol. 54, no. 2, pp. 181 – 342, 1993.

[33] L. Boon and K. Harkay, "Chamber Surface Roughness and Electron Cloud for the Advanced Photon Source Superconducting Undulator," in *Proceedings of ECLOUD'12: Joint INFN-CERN-EuCARD-AccNet Workshop on Electron-Cloud Effects* (R. Cimino, G. Rumolo, and F. Zimmermann, eds.), vol. CERN-2013-002, (La Biodola, Elba, Italy), pp. 95 – 98, June 2012.

[34] G. Dugan and D. Sagan, "Synrad3D Photon Propagation and Scattering Simulations," in *Proceedings of ECLOUD'12: Joint INFN-CERN-EuCARD-AccNet Workshop on Electron-Cloud Effects* (R. Cimino, G. Rumolo, and F. Zimmermann, eds.), vol. CERN-2013-002, (La Biodola, Elba, Italy), pp. 117–129, June 2012.

[35] D. Sagan and J. C. Smith, "The TAO accelerator simulation program," in *Proceedings of the Particle Accelerator Conference 2005*, (Knoxville, TN, USA), p. FPAT085, May 2005.

[36] G. Decker and O. Singh, "Method for reducing x-ray background signals from insertion device x-ray beam position monitors," *Phys. Rev. ST Accel. Beams*, vol. 2, Nov 1999.

[37] V. Sajaev, "Lattice definitions," Nov 2014.

[38] L. Boon, A. Garfinkel, and K. Harkay, "Heat Load for the APS Superconducting Undulator," in *Proceedings of the International Particle Accelerator Conference 2011*, (San Sebastian, Spain), p. THPC186, JACoW, September 2011.

[39] K. Harkay, L. Boon, and A. Xiao, "Synchrotron Radiation Heat load on the superconducting undulator SCU chamber for ideal and missteered beam trajectories," Tech. Rep. ASD-AOP-2011-32, Argonne National Laboratory, August 2011.

[40] E. Trakhtenberg, P. Den Hartog, and G. Wiemerslage, "Extruded aluminum vacuum chamber for insertion devices," in *Proceedings of the Particle Accelerator Conference 2011*, (New York, NY, USA), p. THOBS5, JACoW, March 2011.

[41] L. Assoufid, J. Qian, C. M. Kewish, C. Liu, R. Conley, A. T. Macrander, D. Lindley, and C. Saxer, "A microstitching interferometer for evaluating the surface profile of precisely figured x-ray K-B mirrors," *Proc. SPIE*, vol. 6704, 2007.

[42] M. Jaski, "Sector 6 Ray Tracings with SCU0 Test Vacuum Chamber," Tech. Rep. APS_1431001, Argonne National Laboratory, Argonne, IL, USA, 2012.

[43] M. Jaski, "Private Communication," August 2012.

[44] K. Kim, "Characteristics of Synchrotron Radiation," in *AIP Conference Proceedings*, pp. 565–631, 1984.

[45] R. Dejus, "Power Distribution from a Dipole Source," Tech. Rep. APS_1424215, Argonne National Laboratory, August 2003.

[46] ASM Aerospace Specification Metals Inc., asm.matweb.com.

[47] Cryogenics Technologies Group.

[48] F. Zimmermann and G. Rumolo, "Electron Cloud Build Up in Machines with Short Bunches," in *ICFA Beam Dynamics Newsletter* (K. Ohmi and M. Furman, eds.), vol. 33 of *ICFA Beam Dynamics Newsletter*, pp. 14 – 24, International Committee for Future Accelerators, April 2004.

[49] J. Crittenden, Y. Li, X. Liu, M. A. Palmer, J. P. Sikora, S. Calatroni, and G. Rumolo, "Electron Cloud Modeling Results for Time-Resolved Shielded Pickup Measurements at CesrTA," in *Proceedings of the Particle Accelerator Conference 2011*, (New York, NY, USA), p. WEP142, JACoW, March 2011.

[50] J. Sikora, M. Billing, J. Crittenden, Y. Li, M. Palmer, and S. DeSantis, "Time Resolved Measurement of Electron Clouds at CesrTA using Shielded Pickups," in *Proceedings of the Particle Accelerator Conference 2011*, (New York, NY, USA), p. WEP195, JACoW, March 2011.

[51] L. E. Boon, J. Crittenden, and T. Ishibashi, "Application of the Synrad3D Photon-Tracking Model to Shielded Pickup Measurements of Electron Cloud Buildup at CesrTA," in *Proceedings of the International Particle Accelerator Conference 2011*, (San Sebastian, Spain), p. WEPC141, JACoW, September 2011.

[52] "Lake Shore Cryotronics."

[53] K. Harkay, "SCU0 Test Chamber Beam-Based Alignment," Tech. Rep. ASD-AOP-2013-002, Argonne National Laboratory 2013, January.

[54] S. H. Kim, "Resistive Wall Heating Due to Image Current on the Beam Chamber for a Superconducting Undulator," Tech. Rep. APS_1429125, Argonne National Laboratory, 2012.

[55] R. Kustom, "Preliminary Report on Heat Load due to Image Currents on the Vacuum Liner of a Superconducting Undulator," Tech. Rep. APS_1423346, Argonne National Laboratory, Argonne, IL, USA, 2011.

[56] B. C. C. Cowie, A. Tadich, and L. Thomsen, "The Current Performance of the Wide Range (90 - 2500 eV) Soft X-ray Beamline at the Australian Synchrotron," *AIP Conf. Proc.*, vol. 1234, no. 1, pp. 307–310, 2010.

[57] R. B. Clarken, J. S. Hughes, K. P. Wootton, Y.-R. E. Tan, and M. J. Boland, "1.5 GeV low energy mode for the Australian Synchrotron," in *Proceedings of the International Particle Accelerator Conference 2013*, (Shanghai, China), p. MO-PEA002, JACoW, May 2013.

[58] R. A. Rosenberg, M. W. McDowell, and J. R. Noonan, "X-ray photoelectron spectroscopy analysis of aluminum and copper cleaning procedures for the Advanced Photon Source," *J. Vac. Sci. Technol. A*, vol. 12, no. 4, pp. 1755–1759, 1994.

[59] "International Radiation Detectors, Inc.."

[60] J. O. Clayton and W. F. Giauque, "The Heat Capacity And Entropy Of Carbon Monoxide. Heat Of Vaporization. Vapor Pressures Of Solid And Liquid. Free Energy To 5000 °K. From Spectroscopic Data," *J. Am. Chem. Soc.*, vol. 54, no. 7, pp. 2610–2626, 1932.

[61] J. W. Leachman, R. T. Jacobsen, S. G. Penoncello, and E. W. Lemmon, "Fundamental Equations of State for Parahydrogen, Normal Hydrogen, and Orthohydrogen," *J. Phys. Chem. Ref. Data*, vol. 38, no. 3, pp. 721–748, 2009.

[62] P. Thieberger, W. Fischer, H. Hseuh, V. Ptitsyn, L. P. Snydstrup, D. Trbojevic, and S. Y. Zhang, "Estimates for secondary electron emission and desorption yields in grazing collisions of gold ions with beam pipes in the BNL Relativistic Heavy Ion Collider: Proposed mitigation," *Phys. Rev. ST Accel. Beams*, vol. 7, Sep 2004.

[63] J. G. Endriz and W. E. Spicer, "Study of Aluminum Films. II. Photoemission Studies of Surface-Plasmon Oscillations on Controlled-Roughness Films," *Phys. Rev. B*, vol. 4, pp. 4159–4184, Dec 1971.

[64] Y. Suetsugu, H. Fukuma, M. Pivi, and L. Wang, "Continuing study on electron-cloud clearing techniques in high-intensity positron ring: Mitigation by using groove surface in vertical magnetic field," *Nucl. Instrum. Methods Phys. Res., Sect. A*, vol. 604, no. 3, pp. 449 – 456, 2009.

[65] A. Tremsin and O. Siegmund, "The dependence of quantum efficiency of alkali halide photocathodes on the radiation incidence angle," in *SPIE Conference on EUV, X-Ray and Gamma-Ray Instrumentation for Astronomy X*, vol. 3765, (Denver, CO), pp. 441–451, Experimental Astrophysics Group, July 1999.

[66] E. Gullikson, *X-Ray Data Booklet*, ch. Mass Absorption Coefficients, pp. 1–38 to 1–43. No. 1.6, Lawrence Berkeley National Laboratory, third edition ed., October 2009.

VITA

VITA

Laura Boon received her B.S. in Physics from Case Western Reserve University in May 2009. She started her PhD work in the Physics and Astronomy Department at Purdue University that summer. In January 2010 she started working with Dr. Katherine Harkay of Argonne National Laboratory on electron cloud growth. Laura completed her Masters degree in Physics in May 2011, and moved to Chicago to continue her work on beam induced heating of the superconducting undulator at the Advanced Photon Source.